NTNU

Norwegian University of
Science and Technology

Mass Transfer Coefficients and Bubble Sizes in Oxidative Ladle Refining of Silicon

Erlend Lunnan Bjørnstad

Materials Science and Engineering
Submission date: June 2016
Supervisor: Gabriella Tranell, IMTE
Co-supervisor: Hugo Atle Jakobsen, IKP
Jannike Solsvik, IKP

Norwegian University of Science and Technology
Department of Materials Science and Engineering

Abstract

The mass transfer of $[Al]$ and $[Ca]$ between three synthetic $SiO_2 - CaO - Al_2O_3$ slags, and 8N silicon, has been investigated to find the overall mass transfer coefficient $k_{i,t}$ for the individual species. Samples were kept at 1873K for 5, 10, 20, 30 and 180min before quenching. The metal phase was later analyzed by ICP-MS to view how the concentrations of impurities change with respect to time. This work then compares these results to industrial data gathered from ladles used for oxidative ladle refining of silicon from Elkem Salten in 2012 and 2014, on 96% and 99% *Si* alloys. These measurements were not gathered by this author but generously provided by Elkem as part of the KPN FUME project. To get a better understanding of the mass transfer kinetics in oxidative ladle refining is of great importance to the industry at it allows them to supply more specialized products.

In addition to the mass transfer experiments this thesis contains a literature review of the scaling of bubble column reactors and important parameters controlling bubble sizes in these types of reactors. Based on this it proposes a cold reactor experiment, scaled in such a way as to exhibit similarity, with respect to initial bubble sizes, with the industrial ladle. Both the mass transfer experiment and the proposed bubble column experiment are meant to find parameters needed to be able to create a comprehensive CFD model of oxidative ladle refining.

The values gained from ICP-MS for the experimental data were exceptionally high when compared to the equilibrium concentrations of $[Al]$ and $[Ca]$ found in the literature, for silicon in equilibrium with $SiO_2 - CaO - Al_2O_3$ slags, at 1873K. This is considered to be due to a contaminated standard metal sample used to calibrate the machine. While a new round of analyses could not be completed due to time constraints it is deemed that the data can still be useful as the error should be consistent for all the samples. This allows for an analysis of the trends seen in the experimental data, and to compare it to the ones seen in the industrial alloys.
While looking at the trends the data was normalized with respect to the largest value, found in each sample series, for each species. This is the initial concentration for the industrial data as they have a contaminated metal where the impurities move into a slag. For the experimental data this is the 180min concentration as the experiment looks at impurities moving from a slag into a clean metal. This should have no impact on the trends as $k_{i,t}$ should be equal in both cases. A consistent trend in both the experimental and industrial data was that the mass transfer rate was higher in the samples with lower initial concentration gradient of impurities. In the experimental data one could in addition see a trend where the sample with the highest slag viscosity had the largest initial mass transfer rate. The sample with the lowest slag viscosity had consequently the lowest initial mass transfer rate. This does not agree with the theoretical data on the subject, and due to this no reasonable $k_{i,t}$ could be extracted. Seen in isolation the behavior of $[Ca]$ in both the industrial alloys follows the model from Engh [1] quite well. This is not true for $[Ca]$ in the experimental data, where $[Ca]$ has the same behavior as $[Al]$ for all the slags. $[Al]$, in the 96% alloy, exhibited the closest degree to the expected behavior according to Engh's model, with respect to the other $[Al]$ data. $[Al]$ in the 99% alloy and in the experimental data exhibited a more complex behavior. No theory has been found by this author to explain this behavior. A better fit for the data can be achieved by adding in additional expressions, but there is not enough data to say anything conclusive on this subject.

The central bubble column in oxidative ladle refining can be expressed as a chemical bubble column reactor. The literature concerning the behavior of bubbles in bubble column reactors has been reviewed. Using dimensional analysis, and based on the literature, an experiment has been proposed to measure the initial bubble sizes in oxidative ladle refining of silicon. This is proposed done with a cold fluid reactor exhibiting similarity with the industrial system, by controlling other factors then the ones measured.

Preface

This thesis is submitted to the Department of Materials Science and Engineering, at the Norwegian University of Science and Technology(NTNU), Trondheim, as the primary evaluation requirement for the course TMT4905, and partial requirement for the degree of Master of Science.
This work has been performed between January 2016 to June 2016 at the Department of Materials Science and Engineering, in collaboration with the Department of Chemical Engineering, at NTNU. It was conducted as part of the CRI Metal Production, and financed by the Research Council of Norway.

At first i would like to thank my primary supervisor Professor Gabriella Tranell, and my co-supervisors Professor Hugo Atle Jakobsen and Jannike Solsvik, for their support, enlightening discussions and valuable insight. I would also like to thank Egil Grøndal Krystad for his invaluable help and know how, while doing experiments, analysis, and for always being available for questions and discussion. I would like to thank Lars Klemet Jakobsson for allowing me to use his materials, and in sharing his experience. I would like to thank Ivar Andre Ødegård for sharing his mechanical expertise in designing the cold model. I am grateful for Håkon Aleksander Hartvedt Olsen as a valuable discussion partner and some one to pitch ideas to. I am also thankful for all the help with the furnace provided by Jonas Einan Gjøvk, Dmitry Slizovskiy and Tine Christin Eikevik. I would like to thank Aksel Alstad, Torild Krogstad, Syverin Lierhaugen and Ove Darell for their help preparing and analyzing the samples. I would also like to thank Vegar Andersen and Elkem for their support and interest in this work, and for sharing their industrial information. At last i would like to thank the SiManTi group for the weekly sessions and various events of academic and non-academic nature.

Trondheim, June 2016

Erlend Lunnan Bjørnstad

Contents

0.1 Letters and Symbols Used

Species

$[El]$	The species El is in the metal phase.
(El)	The species El is in the slag phase.
$\{El\}$	The species El is in the gas phase.

Property Distributions

$[wt\%El]$	wt% of species El in the metal phase.	$[-]$
$[ppm\ El]$	ppm of species El in the metal phase.	$[-]$
$(wt\%El)$	wt% of species El in the slag phase.	$[-]$
$(mol\%El)$	mol% of species El in the slag phase.	$[-]$

Dimensionless Numbers

Eo	Eotvos Number	$Eo = \frac{g(\rho_l - \rho_g)d_b^2}{\sigma}$
Mo	Morton Number	$Mo = \frac{g\mu_l^4(\rho_l - \rho_g)}{\rho_l^2\sigma^3}$
Oh	Ohnesorge number	$Oh = \frac{\mu}{\sqrt{\rho\sigma\ d}}$
Re	The Reynolds number	$Re = \frac{vd}{\nu}$
Sc	Schmidt number	$Sc = \frac{\mu}{D}$
Sh	Sherwood number	$Sh = \frac{k\ l}{D}$
We	Weber number	$We = \frac{\rho U^2 d}{\sigma}$

Greek Letters

α	The volume fraction	$[-]$
ε	The specific rate of energy dissipation	$[\frac{kg}{m\,s^3}]$
γ_i	The activity coefficient	$[-]$
γ	Density ratio	$[-]$
κ	Viscosity ratio	$[-]$
λ	Diameter ratio	$[-]$
μ	The dynamic viscosity	$[\frac{kg}{m\,s}]$
ν	The kinematic viscosity	$[\frac{m^2}{s}]$
ω	The mass fraction	$[-]$
ϕ	Frequency constant	$[\frac{1}{s}]$
φ	Used to simplify expressions	$[\frac{1}{s}]$
ρ	The mass density	$[\frac{kg}{m^3}]$
$\bar{\rho}$	Average mass density	$[\frac{kg}{m^3}]$
σ	Surface energy density/ Inter facial Tension	$[\frac{J}{m^2}]$
$\sigma_{k,p}$	Surface energy density between phase k and p	$[\frac{J}{m^2}]$
θ	Contact Angle	$[rad]$

Subscripts	**and Superscripts**
∞	At $t \to \infty$
$\circ$	At equilibrium
$\star$	At the adsorption interface
b	The gaseous bubble phase
c	Continuous phase
d	Dispersed phases
eq	At equilibrium
end	At the end
g	Gas phase
i	A unique species
in	Initial or input
j	Counting variable
k	A unique phase
l	Liquid
n	An amount
N	The total amount
m	The liquid metal phase
p	A unique phase
plug	Porous plug
s	Slag phase
solid	Solid phase
sp_i	Sampling point number i
t_0	At $t = 0$

Letters

a	The activity	$[-]$
a	Acceleration	$[fracms^2]$
A	The area	$[m^2]$
A_s	The surface area	$[m^2]$
B	Basicity	$[-]$
c	The molar density	$[\frac{mol}{m^3}]$
C	A constant	$[varies]$
d	Diameter	$[m]$
$\bar{d}$	Averaged diameter	$[m]$
d_e	Volume equivalent sphere diameter	$[m]$
d_{SD}	Sauter diameter	$[m]$
d_s	Surface area equivalent sphere diameter	$[m]$
D_i	Fickian diffusion constant/diffusivity of species i	$[\frac{m^2}{s}]$
D	Diameter	$[m]$
E	Enhancement factor	$[-]$
f_i	The Henrian activity coefficient of species i	$[-]$
$f(x)$	A function with some set of variables x	$[varies]$
F	Scalar force	$[N]$
g	The magnitude of the acceleration due to earth's pull on a body	$[\frac{m}{s^2}]$
$\mathbf{g}$	The gravity acceleration vector	$[\frac{m}{s^2}]$
G	The Gibbs Energy	$[J]$
$G^\star_\mu$	Viscous energy	$[\frac{J}{mol\ K}]$
ΔG°	The equilibrium Gibbs energy	$[\frac{J}{mol}]$
$\Delta_r G^\circ_x$	The Gibbs energy of reaction for reaction x at equilibrium	$[\frac{J}{mol}]$
$\hbar$	The reduced Planck constant	$[J\ s]$
H	Height	$[m]$
I	Ion-Oxygen Parameter	$[m^{-2}]$
k	The mass transfer coefficient	$[\frac{m}{s}]$
$\bar{k}$	Average mass transfer coefficient	$[\frac{m}{s}]$
k_t	Total mass transfer coefficient	$[\frac{m}{s}]$
K_x	The distribution coefficient constant for reaction x	$[-]$
l	A characteristic length	$[m]$
L	A characteristic length	$[m]$
m	The mass	$[kg]$
$\dot{m}$	Change in mass with respect to time over a specific volume.	$[\frac{kg}{s\ m^3}]$
$\dot{\mathbf{m}}$	The total mass flux vector	$[\frac{kg}{m^2\ s}]$
M_i	The molar mass of species i	$[\frac{g}{mol}]$
n	# of moles	$[mol]$
n_{tg,t_0}	Total initial amount of moles in the gas phase	$[mol]$
$\mathbf{n}$	The normal vector	

N_i	The scalar molar flux of species i	$[\frac{mol}{m^2\ s}]$
N_A	Avogadro constant	$[mol^{-1}]$
P	Pressure	$[Pa]$
P_i	Partial pressure of species i	$[Pa]$
ΔP	The pressure difference	$[Pa]$
r	Radius	$[m]$
$r_{i,k}$	The mass reaction rate of species i in phase k over a specific volume	$[\frac{kg}{s\ m^3}]$
r_{cat}	Radius of the cation	$[m]$
r_o	Radius of the oxygen anion	$[m]$
R	The gas constant	$[\frac{J}{mol\ K}]$
R_1, R_2	Principal radii of curvature	$[m]$
t	Time	$[s]$
T	Temperature	$[K]$
T_{cr}	Critical temperature	$[K]$
$\mathbf{u}$	Time averaged and Reinhold decomposed mass velocity vector.	$[\frac{m}{s}]$
U	The free stream velocity or terminal velocity	$[\frac{m}{s}]$
$\bar{U}$	Averaged free stream velocity or terminal velocity	$[\frac{m}{s}]$
U_T	Terminal bubble velocity	$[\frac{m}{s}]$
$\mathbf{v}$	The mass velocity vector	$[\frac{m}{s}]$
V	The volume	$[m^3]$
V_M	Molar volume of an ideal gas	$[\frac{m^3}{mol}]$
X	The mole fraction	$[-]$
z_{cat}	# valence of the cation	$[-]$

Chapter 1

Introduction

Metallurgical silicon is used as a raw material in aluminum alloy production, silicones, the electronics industry and in renewable energy technologies. The demand for products with tight specifications with regard to composition accuracy, has increased drastically over the last decade. An example of this is the high purity product needed to supply manufacturing of solar energy technologies. High purity is of importance since even low concentrations of impurities will harm the semiconductor properties of silicon, thus limiting its use in solar panels. To better control the composition of the final product refining steps are added to the production process. Understanding the refining process is vital to stay competitive and continue to meet the demands of today, but also the demand of tomorrow.

Oxidative ladle refining is one of these refining processes and is conducted by tapping molten silicon into a ladle and purging with oxygen enriched air. After a set of reactions the main impurities, calcium and aluminum, will go to an immiscible oxide phase, a slag, which can easily be separated from the molten silicon.

Harsh operating conditions and the opaqueness of the melt makes it difficult and expensive to preform good quantifiable experiments. This leads to difficulties optimizing the process further due to lacking a good quantitative system description. To solve these problems one can try looking to other fields to see if their knowledge can be carried over, and scaled, to fit metallurgical systems. Utilizing cold models constructed to exhibit similarity with industrial systems has a long history in understanding the steel process, where it has been found a fruitful endeavor. By applying the relations and experience from fluid dynamics and transport theory at more favorable conditions new insights can be gained into the complex kinetics and dynamics of metallurgical systems. Mind you, some limitations have been found, mostly due to lack of experimental data, or that some properties behave vastly different between the two regimes. These results allows for CFD and other models to be constructed. Supplemented by the experimental data they erect a mathematical framework firmly rooted in metallurgy, fluid dynamics and transport theory. These models supply engineers with an environment to test theories quicker leading to a lower response time at: locating probable prospects, locating gaps in our understanding, or verifying what is already thought to be true, but not yet proven. Systems control engineers can then get involved using this framework to build more powerful automatic control systems. In addition it has the benefit of keeping the costs down as it is relatively inexpensive compared to experimental work. It must be noted that experimental work should not be neglected as it is the foundation the models are built on. Together modeling and experimental work allows for a more efficient and sustainable allocation of resources to further the development and optimization of the process.

This thesis continues the work outlined by this authors specialization project [2] at the Department of Materials Science and Engineering at NTNU, Norway, fall 2015. The previous work did a review of the literature concerning the parameters needed to build an extensive CFD model for the oxidative ladle refin-

ing of silicon. In addition it looked at the published experimental literature to see if values or expressions for this properties existed, or needed to be measured. One of the properties which was not found was the mass transfer coefficient between the phases in the system. This work begins this process by conducting small scale mass transfer experiments between 8N silicon and a synthetic $SiO_2 - CaO - Al_2O_3$ slag, with three different compositions, in graphite crucibles. Samples were kept at 1873K for 5, 10, 20, 30 and 180min before quenching. They were later analyzed by ICP-MS to see how the concentration of $[Al]$ and $[Ca]$ changed with time. It compares this to industrial data taken from different ladles at Elkem Salten in 2012 and 2014, on 96% and 99% silicon alloys respectively. While the environments were the samples are taken are quite different it is useful to compare these results to see if one can glean some knowledge from it. In addition to the mass transfer experiments this thesis contains a literature review of the scaling of chemical reactors and important parameters controlling bubble sizes in bubble columns. Based on this it proposes a cold reactor experiment, scaled in such a way as to exhibit similarity, with respect to bubble sizes, with the industrial ladle.

1.1 Thesis Outline

This thesis starts by presenting an overview of the metallurgical production of silicon and oxidative ladle refining. It continues by presenting the relevant theory behind slag formation, reactions in oxidative ladle refining and mass transfer. Following this are sections outlining dimensional analysis, shapes and sizes of bubbles and at last some theory behind the analytical technique used to analyze the samples. Proceeding onward one finds the proposal for the bubble column reactor experiment along with a detailed explanation of the mass transfer experiment. The results of the mass transfer experiment is then presented followed by a discussion and comparison with the industrial data. Conclusions and plans for further work marks the ending of the thesis only followed by the references.

Chapter 2

Process Overview

2.1 Metallurgic Production of Silicon

Metallurgic grade silicon($> 96[wt\%Si]$) [3] is primarily used as an alloying element in aluminum production, but over the last decades the demand for metallurgic grade silicon in the electronic-, chemical- and renewable energy industries has increased drastically. Figure 2.1.1 shows the typical metallurgic production route of silicon. Quartz and carbon sources, like coal, charcoal and wood chips, are fed into an electric arc furnace where quartz is carbothermically reduced to molten silicon. The overall reaction $SiO_{2(quartz)} + 2C \rightarrow [Si] + 2\{CO\}$ is done at high temperatures to give a high silicon yield. Another benefit springing from a high process temperature is the accelerated reaction kinetics, which together with the abundance of charge materials allows the process to be easily scaled to meet the demand. After reduction the molten silicon is tapped from the furnace to undergo refining before casting. Refining is necessary due to the large range of products with different composition specifications. Due to the detrimental effect even small quantities of specific impurities might have on a products final properties, it is desired to be able to control the products final composition with high accuracy and precision. The quartz introduces a low amount of impurities into the process due to the abundance of high purity quartz deposits. Most of the primary impurity elements like Al, P, B, Ca and Fe are introduced through the carbon sources. Depending on the customers needs the metallurgical grade silicon may undergo further refining beyond what is what is shown in figure 2.1.1.An example of this is the production of solar cells, where the purity requirements demand above 6N requiring extensive refining beyond what is depicted in figure 2.1.1.

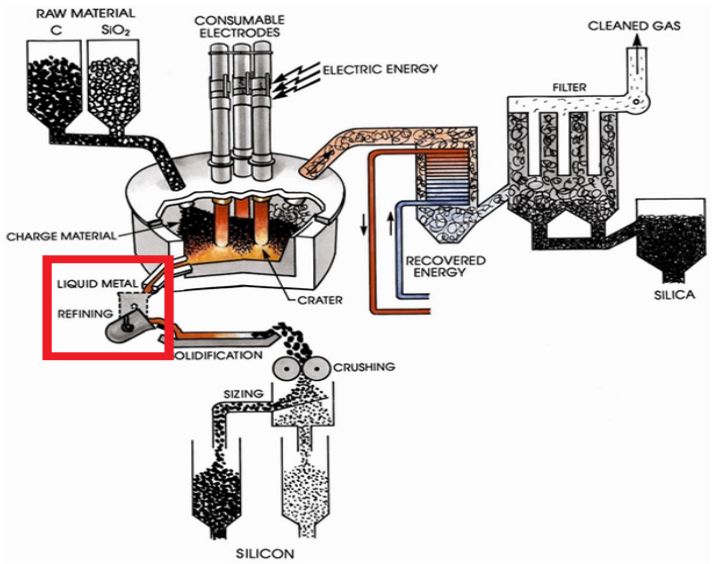

Figure 2.1.1: Typical production chain of silicon. The red box marks the ladle refining step.From Schei et al. [4]

2.2 Oxidative Ladle Refining

Oxidative ladle refining is performed to reduce the concentration of impurities in molten silicon after it leaves the furnace, at temperatures approximately between 1773-1953K [3]. Ladle sizes may vary from plant to plant, but to get a feel for the scale one can visualize a ladle which contains about 7 tonnes of molten Si when full, with a width and height of approximately 2.5-3 m and 3-3.5 m respectively. The refining is done by continually purging with oxygen enriched air from a porous plug located at the bottom of the ladle. This creates a bubble column rising to the top of the melt driving a flow trough the ladle and mixing the melt. The ladle with bubbles can be seen in figure 2.2.1(a). On its ascend the $\{O_2\}$ in the bubbles will react with $[Si]$ to form (SiO_2) and $\{SiO\}$. $\{SiO\}$ will be transported into the bubble saturating the phase with $\{SiO\}$. (SiO_2) reacts with the impurities in the melt, primarily $[Al]$ and $[Ca]$, to form a predominantly $Al_2O_3 - CaO - SiO_2$ slag. The removal of $[Al]$ and $[Ca]$ is the main goal of this process and only the refining of these elements will considered moving forward. The basic reactions are:

1. $[Si] + \{O_2\} = (SiO_2)$
2. $[Si] + \frac{1}{2}\{O_2\} = \{SiO\}$
3. $2[Ca] + (SiO_2) = 2(CaO) + [Si]$
4. $4[Al] + 3(SiO_2) = 3[Si] + 2(Al_2O_3)$

When the slag is formed there will be a driving force to approach equilibrium between the present phases driving a mass transport to the slag so their respective equilibrium concentration can be reached. $\{SiO\}$ together with $\{N_2\}$ will escape through a plume, or "open eye", created as the gas bubbles penetrate the surface slag layer. All $\{O_2\}$ is assumed to have reacted before the plume [5]. The plume causes some emulsification of the top slag layer, reintroducing small slag droplets into the melt. These droplets will be driven to the wall, and congregate there, or be swept by the flow to the bottom of the ladle, depending on the droplets relative density to the bulk. In figure 2.2.1(b) the formation of slag on the bubbles with the plume can be seen together with arrows indicating the flow direction, ascending with the bubble column and descending at the wall.

(a) Enriched air is poured from the bottom threw a nozzle creating a bubble column. The brown layer represents the slag.

(b) Forming of slag at the bubble surface(pink). The arrows indicate the flow pattern.

Figure 2.2.1: The ladle with different aspects added.

The refining process starts the moment molten metal is tapped into an empty ladle until it is filled, and continues for about some time afterwards. A surface slag layer will not be formed straight away, or not at all depending on the composition, leaving the molten metal exposed to the air. This leads to surface reactions between the adsorbed oxygen from the air and $[Si]$ causing losses due to $\{SiO\}$ formation, but also increases the production of (SiO_2) aiding slag formation at the surface. Fine quarts and limestone are added to expedite the formation of the top slag layer and to adjust the slag composition respectively. While filling the ladle a tapping jet from the furnace to the ladle will be present. It will create a hole in the slag and also emulsify some of the slag surrounding its entry point, if a surface slag layer has had time to form. This slag will be transported by the jet flow into the ladle where it might escape to the wall, get dragged to the bottom or get introduced to the general flow, depending on the jet properties and how full the ladle is. In addition, the jet entraps air above the ladle and creates a bubble column of its own. These bubbles are of a different concentration, and size, than the ones introduced from the bottom of the ladle. Figure 2.2.2 illustrates the whole process. After refining the melt is tapped, leaving the unwanted impurities behind. While the refining process is effective it does not work on all elements, noticeably P, B and other elements nobler than Si, meaning other refining steps might be needed depending on the final product.

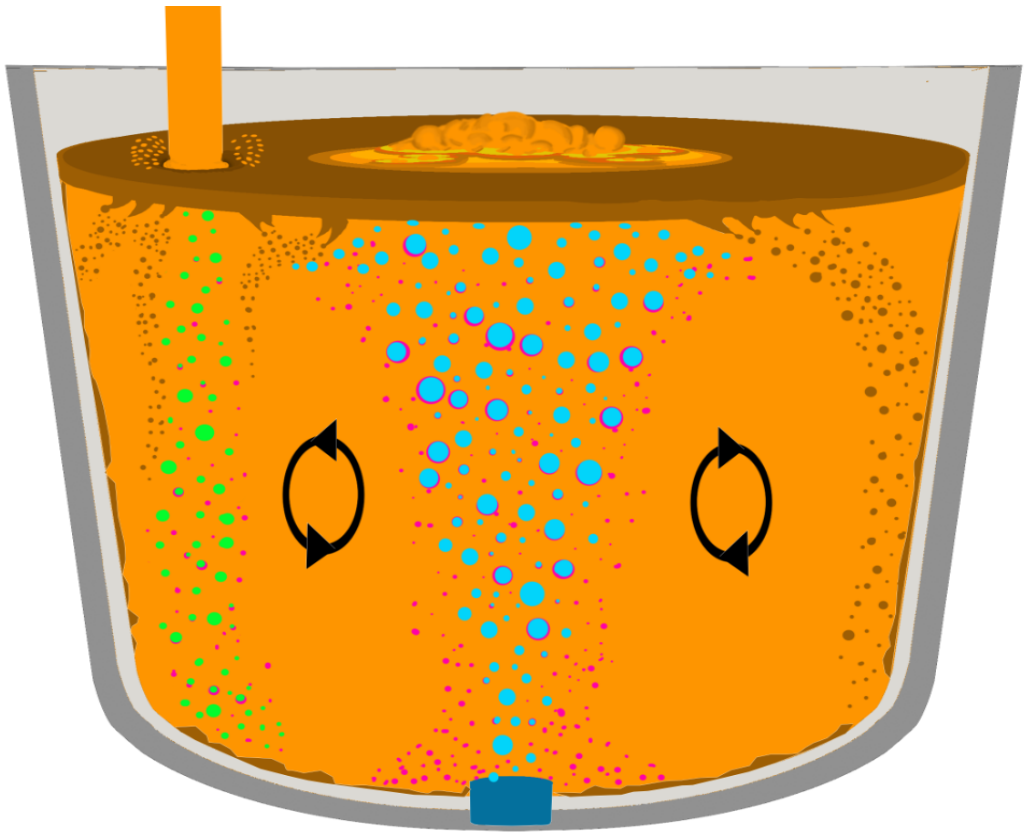

Figure 2.2.2: The whole system including the falling jet. Bubbles of entrapped air are displayed in green.

Chapter 3

Theory

This chapter begins with an overview of the formation of Al_2O_3-CaO-SiO_2 slags and its structure. It continues by discussing the reactions on the bubbles and droplets in the system. Next comes the equilibrium balances between the metal, slag and gas. The experimental part of this thesis only concerns itself with the mass transfer between metal and slag, but the gas is included here to paint the whole picture of the system. While thermodynamics highlight important aspects of the system other aspects can only be viewed through the lens of transport theory and reaction kinetics. The theory surrounding the mass transfer coefficient is reviewed in detail due to its importance determining the kinetics.
The theory concerning the secondary part of the thesis is then presented starting with the dimensional analysis of systems. Expanding upon this theory one can start to describe the shapes of bubbles in flows in different parameter regimes. For industrial applications one needs also to consider the effects present with respect to reactor and injector geometry.
Finally the theory behind the analytical technique ICP-MS presented.

3.1 Al_2O_3-CaO-SiO_2 Slag

In oxidative ladle refining the slag phase is present as an ionic melt, where the molten metal and slag are immiscible. It consists of oxides which form different network structures depending on composition. One way to represent the oxide formation reaction is $x[El] + \frac{y}{2}\{O_2\} \rightarrow \ (El_xO_y)$, where x and y are integers balancing the reaction. The important reactions in the formation of $Al_2O_3 - CaO - SiO_2$ slag are as follows:

1. $[Si] + \{O_2\} = (SiO_2)$
3. $2[Ca] + (SiO_2) = 2(CaO) + [Si]$
4. $4[Al] + 3(SiO_2) = 3[Si] + 2(Al_2O_3)$
5. $3(CaO) + 2[Al] = 3[Ca] + (Al_2O_3)$

Figure 3.1.1 represent this balance by the ternary phase diagram.

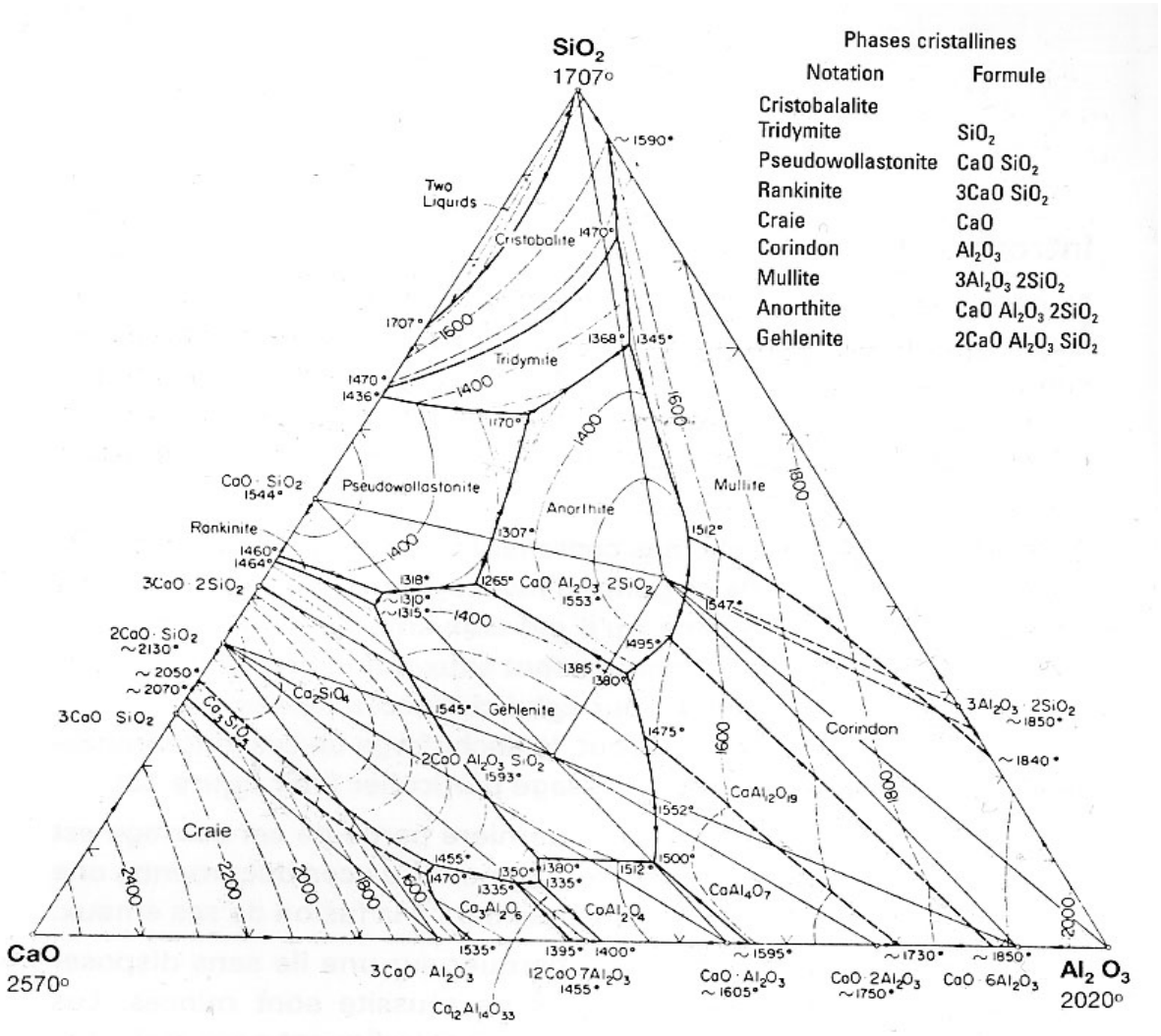

Figure 3.1.1: The ternary phase diagram of $Al_2O_3 - CaO - SiO_2$. Schei et al. [4]

3.1.1 Order of Oxide Formation

The elements which form the slag phase in a given process can be found by using an Ellingham diagram, as seen in figure 3.1.2. ΔG° in the diagram represents the thermodynamic energy barrier a system needs to overcome for a given reaction to take place, with $\Delta G^\circ \leq 0$ giving a favourable reaction. The more negative a reactions ΔG° is the larger the driving force for reaction will become. A consequence of this is that elements with more negative ΔG° should form oxides first. Kero et al. [3] have shown that an elements oxide basicity is of higher importance for oxidative ladle refining of silicon. This is due to the fact that elements with a high oxide basicity will lower the total energy of the slag phase, leading to them reacting first.
Even if ΔG° does not give the order of reaction it does show that if an element has
$\Delta G^\circ(El_xO_y) > \Delta G^\circ(SiO_2)$ then all of the $[Si]$ has to go to (SiO_2) before any (El_xO_y) is formed. This shows how some elements are impossible to refine using this method.

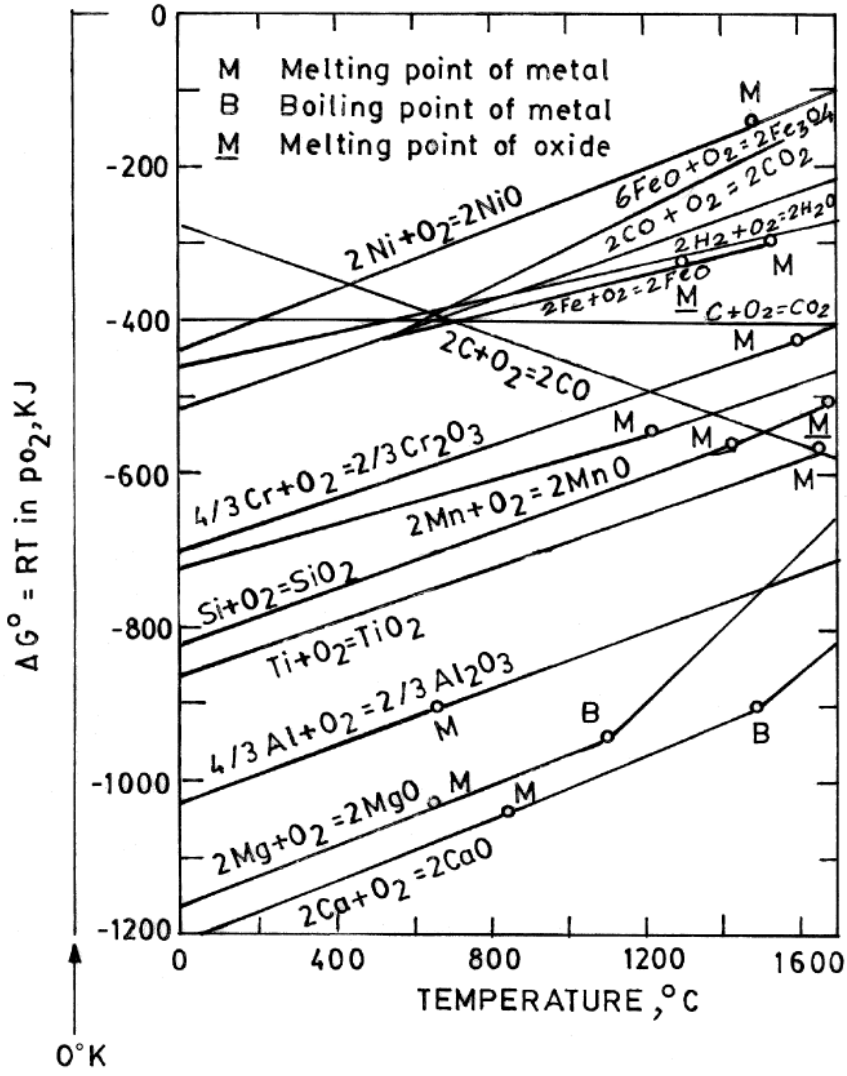

Figure 3.1.2: The Ellingham diagram. Ghosh [6]

3.1.2 Basicity and Slag Structures

Oxides can be categorised as either Lewis acids or bases as they can receive or give an electron pair. Acid oxides form primarily from metals in high oxidation states, or non metals with oxygen coordination numbers 3 or 4. SiO_2 is an acid oxide with the oxygen coordination number 4 and should therefore have a tetrahedral structure. As $SiO_{2\ solid} \rightarrow SiO_{2\ l}$ the covalent structured network of $(SiO_4)^{4-}$ tetrahedra in the solid degrade into a random liquid covalent network of $(SiO_4)^{4-}$ tetrahedra [7]. While the tetrahedra have the composition $(SiO_4)^{4-}$ covalency is retained since each tetrahedra shares each of its oxygen once with its neighbours, giving 2 oxygen for every *Si* atom. In this pure silicate melt the oxygen atoms form bridges between the tetrahedra creating networks, or polymeric structures, as seen in figure 3.1.3. By adding a basic oxide into the mixture, like CaO, an excess amount of oxygen is present creating what is called a non-bridging oxygen. This non-bridging oxygen reacts with the structure decreases the level of polymerization in the mixture, breaking bridges at random points. If the concentration of basic oxides increases beyond 10 mol% [7] complex silicate anions are formed. This changes the silicate melts structure from a random covalent network to an ionic liquid configuration which includes some discrete silicate anions [7], or slag.

Cations who interact strongly with oxygen anions tend to form networks, and the stronger the interaction the stronger this tendency is. This behavior corresponds with the coulombic interaction between the cation and oxygen anion, expressed by the ion-oxygen parameter I:

$$I = \frac{2z_{cat}}{(r_{cat} + r_o)^2} \tag{3.1}$$

If I > 1.7 the oxide is called a network former, and forms networks like SiO_2. If I < 0.7 the oxide breaks the network structure if added to a network former. These oxides, like CaO, are called network modifiers. When $0.7 <$ I < 1.7 the oxide is called amphoteric. Amphoteric oxides behave either as a network former or network modifier depending on the system environment. Al_2O_3 is an amphoteric oxide and behaves as a network modifier if the degree of polymerization is high, or as a network former if it is low. The behaviors of different oxides can be seen in figure 3.1.4.
Kozakevitch [8, As read in [7]] did experiments measuring the activation energy of viscous flow in melts where he kept the $(mol\%SiO_2)$ constant. Waseda and Toguri [7] writes that from Kozakevitch's data one can see that Al_2O_3 behaves as a network former, 4 oxygen coordinated ion, in the region where $\frac{(mol\%CaO)}{(mol\%Al_2O_3)} > 1$. When $\frac{(mol\%CaO)}{(mol\%Al_2O_3)} < 1$, Al_2O_3 starts to behave as a network modifier where the Al-ion is coordinated with 6 oxygen.
Basicity is a term which has proven to be very useful for discussing the properties of a slag. It is usually described as the mass fraction between the basic oxides, the network modifiers, and the acidic oxides, the network formers. For $Al_2O_3 - CaO - SiO_2$ slags if Al_2O_3 behaves as an acid oxide the basicity is expressed by equation 3.2 [9].

$$B = \frac{(wt\%CaO)}{(wt\%SiO_2) + (wt\%Al_2O_3)} \tag{3.2}$$

The basicity is easy to measure since the charge weights are known, and it gives valuable information about the degree of polymerization in the slag. Most of the slags properties are affected by the degree of polymerization making basicity a valuable metric.

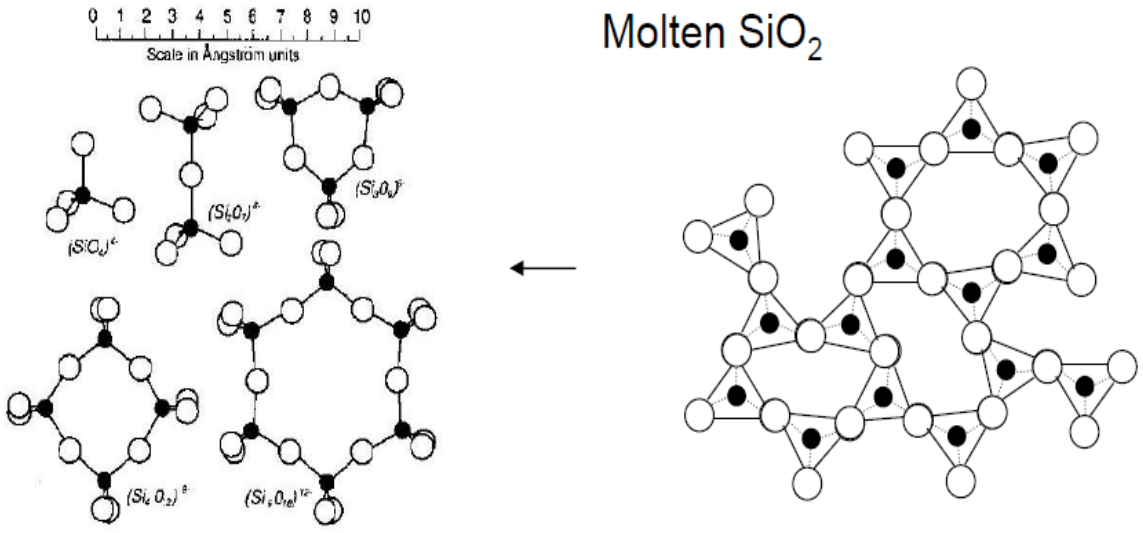

Figure 3.1.3: Structure of $SiO_{2\ l}$ and its transformation into silicates by addition of basic oxides. Tranell [9]

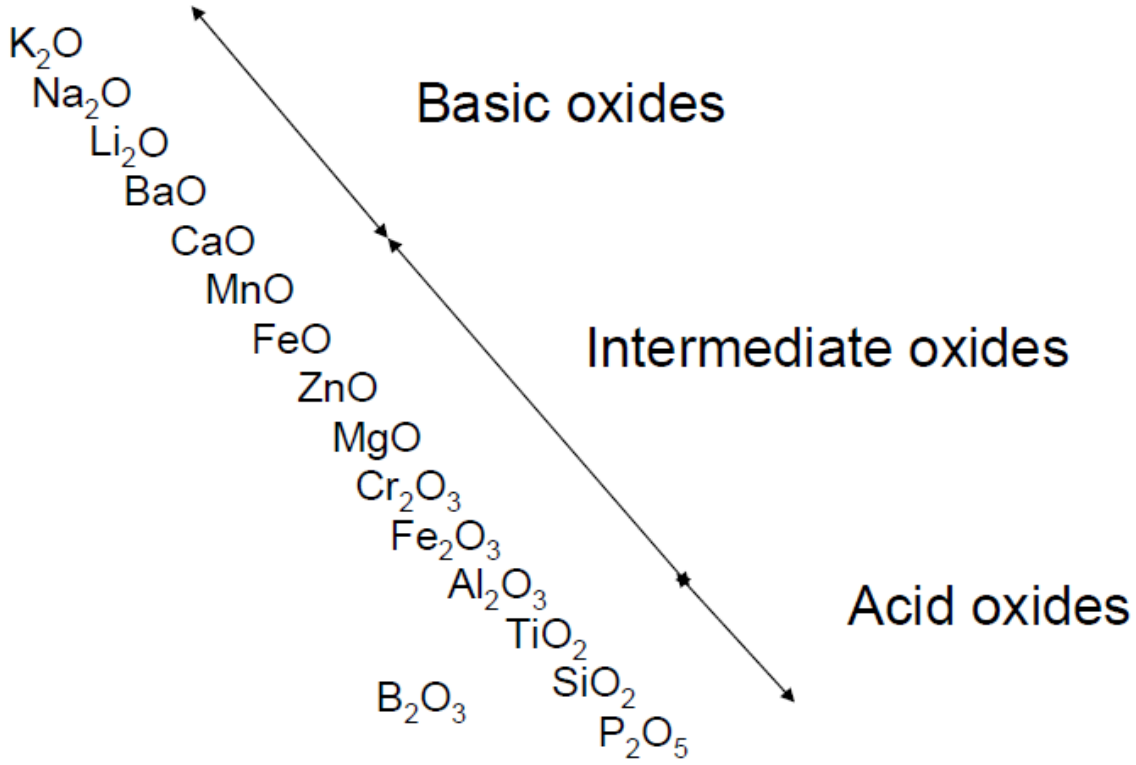

Figure 3.1.4: Common oxides shown in degree of oxygen interaction. Tranell [9].

3.1.3 Viscosity of Al_2O_3-CaO-SiO_2 Slag

In fig 3.1.5 the iso-viscosity curves of $Al_2O_3 - CaO - SiO_2$ are shown. From the figure it can be seen that the iso-viscosity lines run close to parallel with the iso-concentration lines of (CaO). This is due to its network modifying behavior. As $(wt\%CaO)$ decreases and $(wt\%Al_2O_3)$ increases the curves change to angle more towards the iso-concentration line of (SiO_2). Waseda and Toguri [7] writes that this is a sign that (Al_2O_3) starts to change from a network former to a network modifier. From this it can be seen that the viscosity of the slag is linked to its composition where the basicity dictates the degree of polymerization in the slag.
The effect it has on viscosity is easy to see in fig 3.1.5 as the difference between the largest and smallest basicity values gives an increase of three orders of magnitude in viscosity.

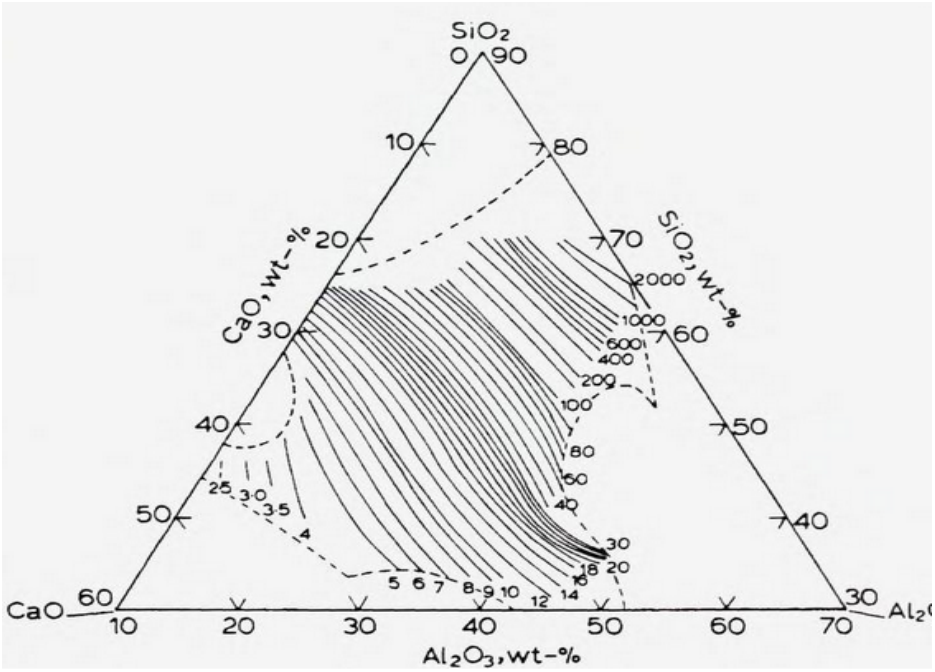

Figure 3.1.5: Iso-viscosity, in [poise], curves of $Al_2O_3 - CaO - SiO_2$ slag melts at 1500 °C. From Turkdogan [10, As depicted in [4]].

Basicity is not the only parameter affecting viscosity. Temperature is another big factor. This can be calculated by an Arrenius expression for the molecular viscosity μ:

$$\mu = \mu_0 \cdot exp(\frac{-G^{\star}_{\mu}}{RT}) \tag{3.3}$$

Equation 3.3 is usually not obeyed for slags with high levels of polymerisation since the degree of polymerisation is reduced by increasing temperature. By introducing the Eyrings expression: $\mu_0 = \frac{N_A \hbar}{V_M}$, as the pre-exponential factor in equation 3.3 it can still be used for $Al_2O_3 - CaO - SiO_2$ slags [9].
Kondratiev and Jak [11] have made a mathematical model for the viscosity of the $Al_2O_3 - CaO - SiO_2$ slag system which can be easily implemented. This model uses experimental data and the ternary phase diagram to calculate $\mu_s = f(X_{(SiO_2)}, X_{(Al_2O_3)}, X_{(CaO)}, X_{(FeO)}, T)$ $[poise]$, and is according to Tang [5] very accurate to the experimental values.

3.1.4 Diffusion Coefficients for the Species in Al_2O_3-CaO-SiO_2 Slag

The fickian diffusion coefficient of a species i in the slag, $D_{(i)}$, and has the units $[\frac{m^2}{s}]$. This term combines multiple factors which describes how easy a particle can move through a given volume. While Maxwell-Stefan diffusion gives a more complete description of the physics behind diffusion then ficks', its diffusion coefficient is the inverse drag coefficient, it is more convenient to use fickian diffusion as it is easier to compute and measure. In this thesis only the fickian diffusion coefficient will be considered, and will just be called the diffusion coefficient. For a more thorough description of diffusion one can read Bjørnstad [2] or Jakobsen [12].
Waseda and Toguri [10] have gathered expressions from multiple authors and writes that the diffusion coefficient can be expressed as a Arrhenius type equation:

$$D_{(i)} = D^0_{(i)} exp\left(-\frac{G^\star_\rho}{RT}\right) \tag{3.4}$$

The expressions they gathered for $D_{(i)}$ are all based on a slag with $40(wt\%CaO) - 40(wt\%SiO_2) - 20(wt\%Al_2O_3)$:
From Niwa and Ocirc [13]:

$$D_{(Ca)} = 6.26 \cdot 10^{-6} exp\left(-\frac{287000}{RT}\right) \tag{3.5}$$

From Towers and Chipman [14] and Henderson et al. [15]:

$$D_{(Al)} = 5.4 \cdot 10^{-4} exp\left(-\frac{234000}{RT}\right) \tag{3.6}$$

$$D_{(Si)} = 4.7 \cdot 10^{-4} exp\left(-\frac{251000}{RT}\right) \tag{3.7}$$

From Oishi et al. [16]:

$$D_{(O)} = 18 \cdot 10^{-4} exp\left(-\frac{227000}{RT}\right) \tag{3.8}$$

Tang [5] has gathered a large amount of experimental data and writes that the diffusion coefficients in the slag are heavily reliant on the viscosity of the slag. While Waseda and Toguri [7] do not propose expressions for this they also agree that this is true. Tang [5] proposes the relations:

$$D_{(Si)} = \frac{9.14 \cdot 10^{-14} T}{\mu_s} \tag{3.9}$$

$$D_{(Al)} = \frac{1.03 \cdot 10^{-13} T}{\mu_s} \tag{3.10}$$

$$D_{(Ca)} = \frac{2.54 \cdot 10^{-13} T}{\mu_s} \tag{3.11}$$

$$D_{(O)} = \frac{8.69 \cdot 10^{-12} T}{\mu_s} \tag{3.12}$$

$$\tag{3.13}$$

It follows from equations 3.9- 3.12 that $D_{(O)} > D_{(Ca)} > D_{(Al)} > D_{(Si)}$. This diffusion order agrees with the data gathered by Waseda and Toguri [10], but their values do not agree if one uses the viscosity model from Kontratiev and Jak [11] in Tang's equations. Tang's [5] relations fit better with the data from Liang et al. [17], but they have a $D_{(O)}$ that varies with approximately one order of magnitude from Tang [5].

3.2 Reactions on the Bubbles and Droplets

As a bubble ascends through the ladle there will be reactions on the bubble surface. Tang [5] has done a large amount of work on the thermodynamics and kinetics of oxidative ladle refining of silicon and proposes the following reaction mechanisms:

1. $\{O_2\}$ diffuses to the melt/gas interface and adsorbed: $\{O_2\} \rightarrow 2\{O\}^\star$
2. $[Si]$ is transported to the melt/gas interface and adsorbed: $[Si] \rightarrow [Si]^\star$
3. Oxidation occurs in the interface
   (a) $[Si]^\star + \{O\}^\star \rightarrow \{SiO\}^\star$
   (b) $[Si]^\star + 2\{O\}^\star \rightarrow [SiO_2]^\star$
   (c) $\{SiO\}^\star + \{O\}^\star \rightarrow [SiO_2]^\star$
4. $\{SiO\}$ desorbs from the interface to the bulk gas: $\{SiO\}^\star \rightarrow \{SiO\}$
5. (SiO_2) nucleates in the interface: $[SiO_2]^\star \rightarrow (SiO_2)$
6. $[Ca]$ and $[Al]$ diffuse to the interface and adsorb at the melt/slag interface:$[Ca], [Al] \rightarrow [Ca]^\star, [Al]^\star$
7. Interface exchange reactions:
   (a) $4[Al]^\star + 3(SiO_2)^\star \rightarrow 2(Al_2O_3)^\star + 3[Si]^\star$
   (b) $2[Ca]^\star + (SiO_2)^\star \rightarrow 2(CaO)^\star + [Si]^\star$
8. $[Si]^\star$ desorbs from the interface to the bulk melt: $[Si]^\star \rightarrow [Si]$
9. $(Al_2O_3)^\star$ and $(CaO)^\star$ desorb from the melt/slag interface to the bulk slag:
   $(Al_2O_3)^\star, (CaO)^\star \rightarrow (Al_2O_3), (CaO)$

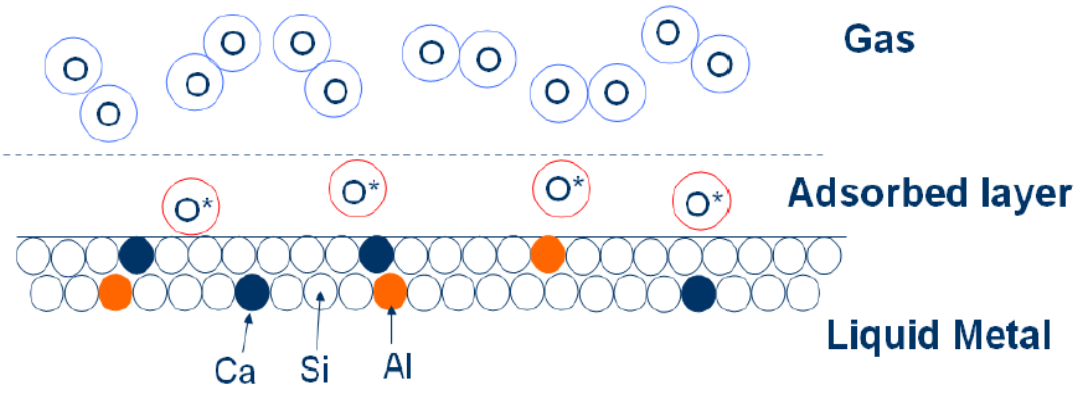

Figure 3.2.1: A schematic representation of the reaction mechanisms. Tang [5]

The reactions can be summed up by:

1. $[Si] + \{O_2\} = (SiO_2)$
2. $[Si] + \frac{1}{2}\{O_2\} = \{SiO\}$
3. $2[Ca] + (SiO_2) = 2(CaO) + [Si]$
4. $4[Al] + 3(SiO_2) = 3[Si] + 2(Al_2O_3)$
5. $3(CaO) + 2[Al] = 3[Ca] + (Al_2O_3)$

To determine the rate limiting step some assumptions need to be made about the system. Reaction 3.) and 4.) shows that the oxidation of $[Al]$ and $[Ca]$ are coupled with reaction 1.). This shows that the reactions are all under the same rate limiting step. Reaction rates tend to increase exponentially with temperature and are highly affected by the available reaction area. Oxidative ladle refining is typically done between 1723K and 1873K, which are considered high temperatures, and with dispersed bubbles giving the reaction area it is not likely that the rate of reaction is rate limiting. Adsorption is a surface phenomena and affected by the surface energy density. Tang states that "As the reaction rate increases, the mass transfer across the interface also goes up, thus lowering interfacial tension" [5] . This leads to the conclusion that adsorption should not be the rate limiting step.
The final place to look for the rate limiting step is in the diffusion of species from the bulk to the interface. Diffusion is affected by the concentration gradient and the ease of mobility for a species through a specific phase. The ease of mobility, or diffusivity D_i, is known somewhat for the species in the system. Diffusivity for a species in the gas phase is approximately six to seven orders of magnitude larger than the diffusivity for the same species in the melt and slag. This excludes diffusion in the gas as being rate limiting. The concentration of $[Si]$ is so much higher then $[Al]$ and $[Ca]$ giving it a large concentration gradient relative to the impurities. This makes it impossible for the diffusion of *Si* to be the rate limiting step. Since the concentration of *Al* and *Ca* will be high in the melt relative to the slag when refining starts it can be deduced that the rate limiting step must be the transport of *Al* and *Ca* in the slag.
As the refining runs its course the concentration of $[Al]$ and $[Ca]$ will become depleted. If their concentrations drop low enough Tang [5] proposes that the diffusion of *Al* and *Ca* in the metal becomes the rate limiting step, but for the majority of the refining process the concentration of $[Ca]$ and $[Al]$ will not be dilute enough for this to happen.

3.2.1 Importance of Ca

Reactions 3.) and 4.) can be rearranged to become:

5. $3(CaO)+2[Al]=3[Ca]+(Al_2O_3)$

Reaction 5.) shows that the concentrations of (Al_2O_3) and (CaO) in the slag will be regulated by the equilibrium of their respective concentrations in the melt. If the concentration of $[Ca]$ is low relative to $[Al]$ an $Al_2O_3-SiO_2$ slag will form. This aluminosilicate slag will be present as solid particles inside the slag phase greatly increasing the slags viscosity. An increase in viscosity has detrimental effects on mass transfer and will slow down the refining process drastically. Tang [5] notes that if the slags viscosity gets above 500 poise then reactions 3.), 4.) and 5.) stop, hindering any further refining. He also writes that the experience in the industry is that close to all of the oxygen reacts as long as reaction 3.) is running. 100% oxygen utilization indicates that the interface reactions are running at local equilibrium. The literature supports this by giving $P_{\{O_2\}}<10^{-15}$atm after reaction 1.) has taken place. Being able to assume equilibrium is a powerful assumption when modeling since it greatly simplifies the calculations and its importance cannot be stated enough. If the concentration of $[Ca]$ is low then the oxygen utilization decreases indicating that the system moves away from equilibrium and the refining becoming less efficient. This fits well with the formation of aluminosilicates described earlier.

3.2.2 Equilibrium Relation Between SiO_2 and SiO

As with reaction 3.) and 4.) reaction 1.) and 2.) can be rearranged:

6. $[Si]+(SiO_2)=2\{SiO\}$

Reaction 6.) is described in the phase diagram of Si-O, figure 3.2.2, where one can see that at a certain temperature T_{cr}, SiO_2 becomes unstable and $SiO_2\rightarrow SiO$. This is important since SiO_2 is the oxygen carrier for the equilibrium refining reactions. T_{cr} and the distribution can be found using thermodynamics and the stoichiometry of reaction 1.) and 2.).

$$n_{[Si]}[Si]+n_{\{O_2\}}\{O_2\}\rightarrow n_{\{SiO\}}\{SiO\}+n_{(SiO_2)}(SiO_2) \tag{3.14}$$

Leading to:

$$n_{[Si]}=n_{\{SiO\}}+n_{(SiO_2)},\qquad n_{\{O_2\}}=\frac{1}{2}n_{\{SiO\}}+n_{(SiO_2)} \tag{3.15}$$

So by knowing $n_{\{SiO\}}$ and $n_{(SiO_2)}$ you know the distribution of Si and O_2 in the different phases.
Using the equilibrium coefficients of reaction 1.) and 2.) Tang [5] has proposed a relation for $P_{\{SiO\}}$ using data from the FACT database:

$$P_{\{SiO\}}\approx\frac{n_{\{SiO\}}}{n_{\{SiO\}}+n_{\{N_2\}}+n_{\{O_2\}}}P_b=\left(\frac{exp(11.13+\frac{39464}{T})}{exp(-23.66+\frac{113623}{T})}\right)^{\frac{1}{2}}P_b \tag{3.16}$$

Equation 3.16 assumes that $\gamma_{[Si]},\gamma_{(SiO_2)}=1$ which is reasonable if one assumes that pure $[Si]$ forms pure (SiO_2) and $\{SiO\}$. $P_b=1atm$ as the total pressure inside the bubbles should equal the ambient pressure affecting them before injection.

The purge gas mixture before reaction is composed of O_2 and N_2 giving the balance:

$$2n_{tg,t_0}X_{\{O_2\}}[Si]+n_{tg,t_0}X_{\{O_2\}}\{O_2\}+n_{tg,t_0}(1-X_{\{O_2\}})\{N_2\}=2n_{tg,t_0}X_{\{O_2\}}\{SiO\}+n_{tg,t_0}(1-X_{\{O_2\}})\{N_2\} \tag{3.17}$$

Using equation 3.16 and neglecting $P_{\{O_2\}}$, since $P_{\{O_2\}} < 10^{-15}$ at equilibrium conditions, one gets:

$$n_{\{SiO\}} = n_{tg,t_0}(1 - X_{\{O_2\}})\frac{P_{\{SiO\}}}{P_b - P_{\{SiO\}}} \tag{3.18}$$

And equation 3.15 gives:

$$n_{(SiO_2)} = n_{tg,t_0}X_{\{O_2\}} - \frac{1}{2}n_{\{SiO\}} \tag{3.19}$$

Giving expressions for both $n_{\{SiO\}}$ and $n_{(SiO_2)}$.
To calculate T_{cr} equation 3.17 is used to give:

$$P_{\{SiO\}} = \frac{2X_{\{O_2\}}}{1 + X_{\{O_2\}}}P_b \tag{3.20}$$

together with equation 3.16 [5] gives the relation:

$$T_{cr} = 1874.7 + 88.533ln(X_{\{O_2\}}) \tag{3.21}$$

for the critical temperature T_{cr} in $^{\circ}C$. This creates a benchmark for which temperatures and oxygen fractions can be used to run the refining process.

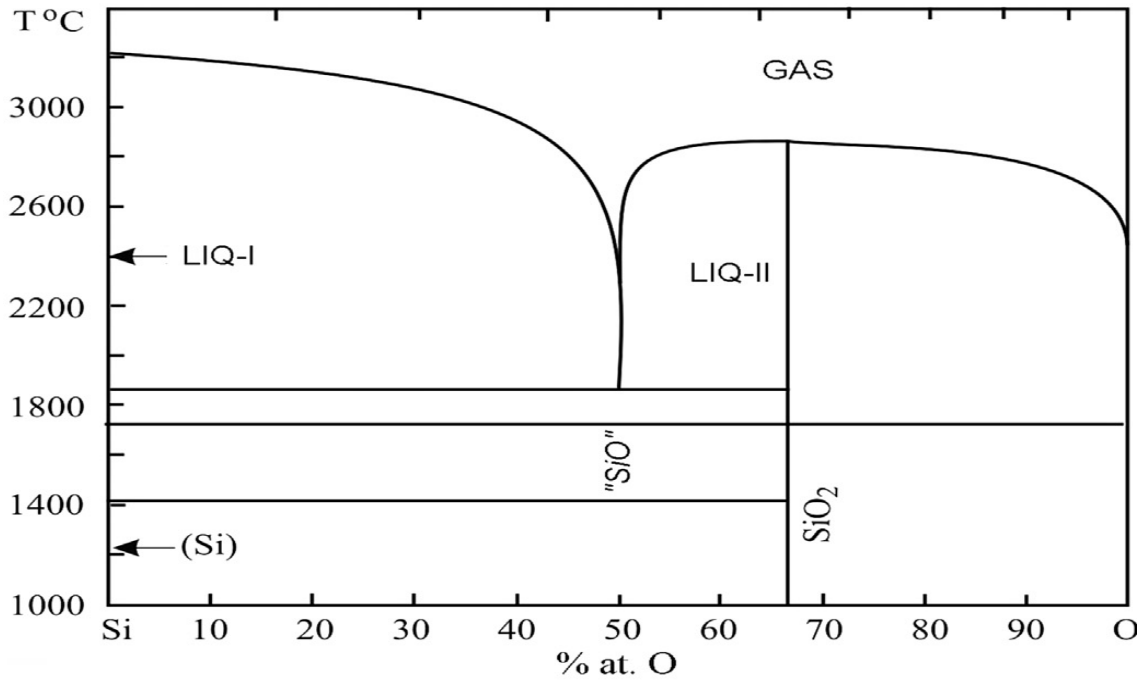

Figure 3.2.2: The phase diagram of Si-O, Tangstad [18]

3.2.3 Melt-Slag Balance

When doing an equilibrium balance between the melt and the slag one would normally use the Gibbs energy equation coupled with thermodynamic data on reactions 3.), 4.) and 5.) to give equations 3.22, 3.23 and 3.24.

$$\frac{a^2_{(CaO)}\ a_{[Si]}}{a^2_{[Ca]}\ a_{(SiO_2)}} = exp(-\frac{\Delta_r G^\circ_3}{RT}) = \frac{(X_{(CaO)}\ \gamma_{(CaO)})^2\ a_{[Si]}}{(X_{[Ca]}\ \gamma_{[Ca]})^2\ (X_{(SiO_2)}\ \gamma_{(SiO_2)})} \tag{3.22}$$

$$\frac{a^2_{(Al_2O_3)}\ a^3_{[Si]}}{a^4_{[Al]}\ a^3_{(SiO_2)}} = exp(-\frac{\Delta_r G^\circ_4}{RT}) = \frac{(X_{(Al_2O_3)}\ \gamma_{(Al_2O_3)})^2\ a^3_{Si}}{(X_{[Al]}\ \gamma_{[Al]})^4\ (X_{(SiO_2)}\ \gamma_{(SiO_2)})^3} \tag{3.23}$$

$$\frac{a_{(Al_2O_3)}\ a^3_{[Ca]}}{a^2_{[Al]}\ a^3_{(CaO)}} = exp(-\frac{\Delta_r G^\circ_5}{RT}) = \frac{(X_{(Al_2O_3)}\ \gamma_{(Al_2O_3)})\ (X_{[Ca]}\ \gamma_{[Ca]})^3}{(X_{[Al]}\ \gamma_{[Al]})^2\ (X_{(CaO)}\ \gamma_{(CaO)})^3} \tag{3.24}$$

The problem with this approach is that finding the activity coefficients, γ_i, for a component i is difficult. When working with $\{SiO\}$ and (SiO_2) it could be assumed that $\gamma_{[Si]}, \gamma_{(SiO_2)} = 1$, since the components created were pure, but this is not the case for the slag reactions.

Jakobsson [19] did an extensive literary review of the activities and iso-concentration curves concerning the $SiO_2 - CaO - Al_2O_3$ slag system at 1600°C. In this review he writes that the work by Rein and Chipman [20] is considered the most representative for the ternary $SiO_2 - CaO - Al_2O_3$ at 1600°C due to its close agreement with the work done by Morita et al. [21] at 1550°C. The iso-activity diagrams from Rein and Chipman can be seen in figure 3.2.3 and 3.2.4.

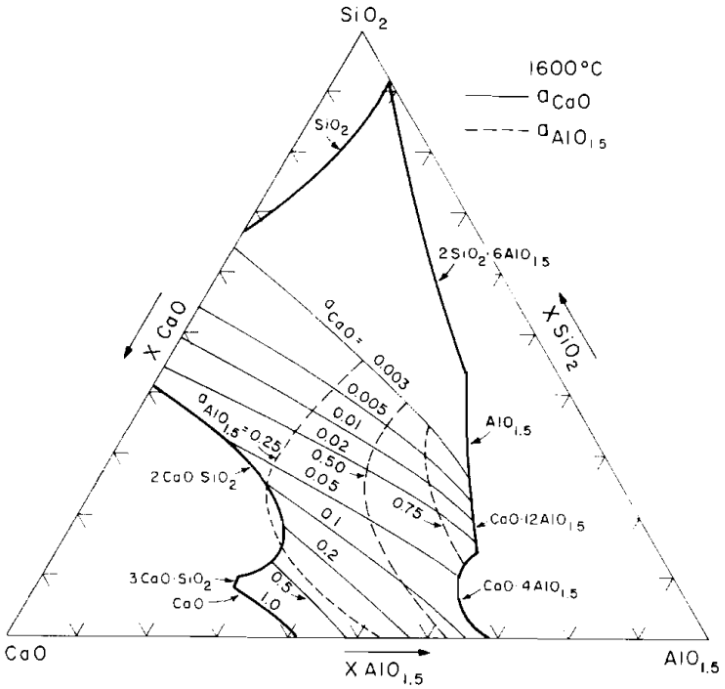

Figure 3.2.3: Iso-activity diagram for CaO and $AlO_{1.5}$ at 1600°C. From Rein and Chipman [20].

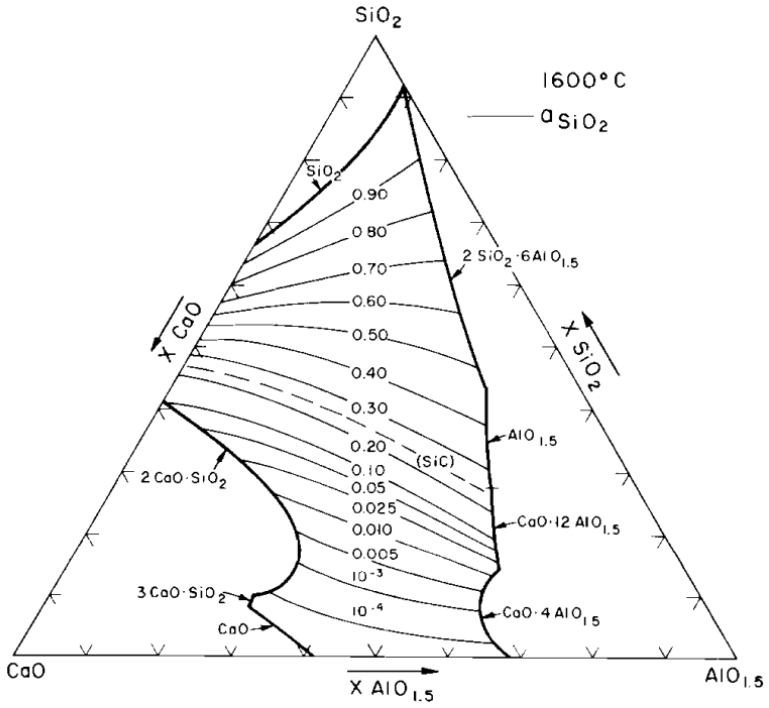

Figure 3.2.4: Iso-activity diagram for SiO_2 at 1600°C. From Rein and Chipman [20].

Using the results from Rein and Chipman [20] and FACTSAGE, Jakobsson [19] compared them with his own results and found that FACTSAGE gave the best agreement with his data. The self-interaction of aluminum found by Miki et al. [22] was used in the FACTSAGE calculation. From this he generated $\gamma^0_{[Al]} = 0.66$ which he comments does not agree with Miki et al. [22] who gives $\gamma^0_{[Al]} = 0.23$, if one extrapolates their relation to 1600°C. It is also bigger than $\gamma^0_{[Al]} = 0.45 \pm 0.09$ found experimentaly by Margaria et al. [23], who also calculated $\gamma^0_{[Al]} = 0.53$ based on the work from Weiss and Schwerdtfeger [24].

While Morita et al. [21] and Wang et al. [25] have done extensive investigations on the iso-concentration lines for $[Al]$ and $[Ca]$ in equilibrium with $SiO_2 - CaO - Al_2O_3$ at 1550°C Jakobsson [19] has compared his results at 1600°C to the work of Schei et al. [4] and Wang et al. [25] at 1550°C. Jakobsson notes that his data from 1600°C fits well with the previous data for the (SiO_2) rich region, but beyond that one starts to get deviations.

Tang [5] has developed a different method for calculating the distribution between the melt and slag. By using the equilibrium slag-metal distribution coefficient for the different elements he has created expressions for the concentrations by fitting thermodynamic data using the FACT database. His expression are as follows:

$$(wt\%Ca) = (9.6375[wt\%Al])^{-0.5591} + (20.2121[wt\%Ca])^{0.2595},\ (wt\%CaO) = 1.399(wt\%Ca) \quad (3.25)$$

$$(wt\%Al) = (38.497[wt\%Al])^{0.2665} - (26.2167[wt\%Ca])^{0.2139},\ (wt\%Al_2O_3) = 1.89(wt\%Al) \quad (3.26)$$

$$(wt\%Si) = 0.4674(100 - 1.89(wt\%Al) - 1.4(wt\%Ca)),\ (wt\%SiO_2) = 2.139(wt\%Si) \quad (3.27)$$

Tang [5] also notes that these expressions are not affected heavily by temperature and can be taken to be unaffected in the range $1773K < T < 1973K$. Tang's expressions have the benefit of being easy to compute but may give other problems because of its simplicity, like needing a small step size to give good results.

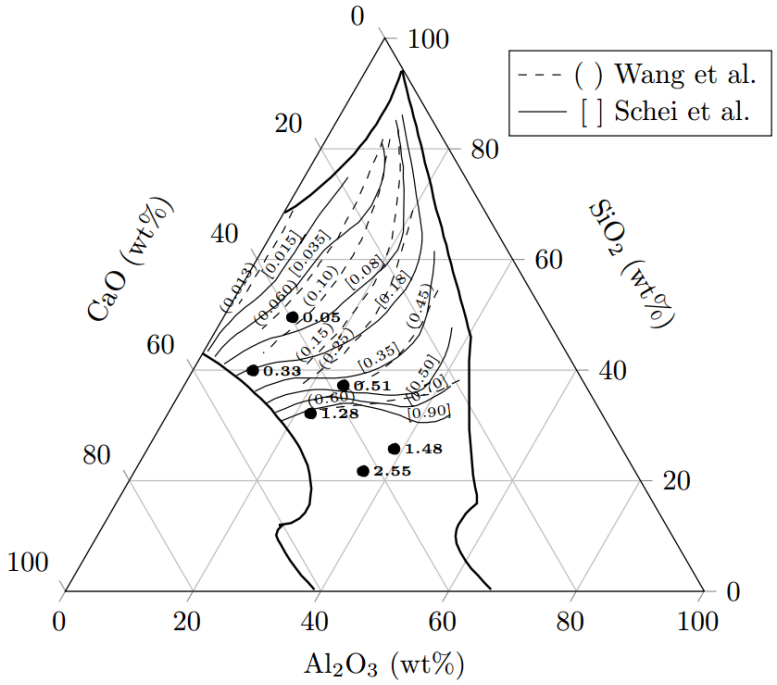

Figure 3.2.5: Iso-concentration lines for $[Al]$ from Schei et al. [4] and Wang et al. [25] at 1550°C. The black circles are from Jakobsson [19] at 1600°C.

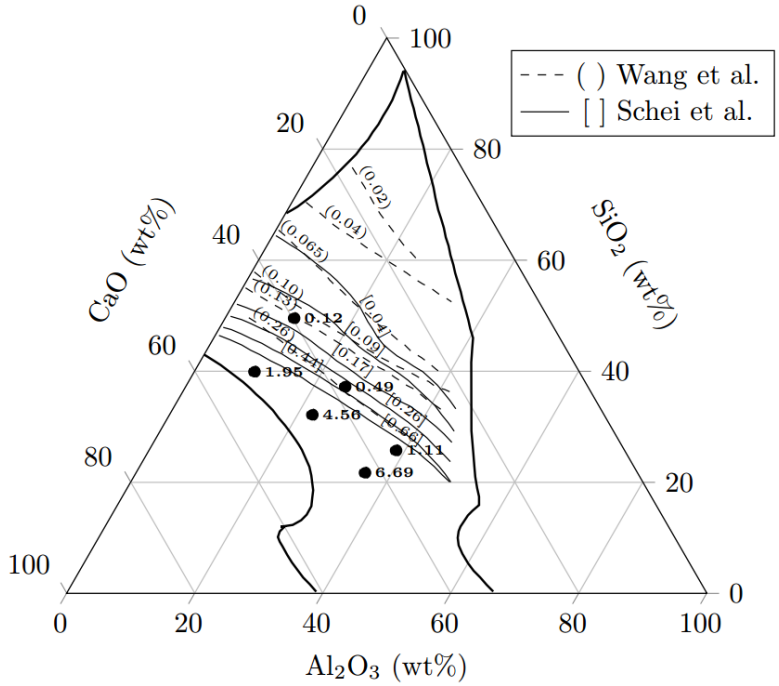

Figure 3.2.6: Iso-concentration lines for $[Ca]$ from Schei et al. [4] and Wang et al. [25] at 1550°C. The black circles are from Jakobsson [19] at 1600°C.

It should also be noted that Schei et al. [4] has compared the activity of $[Al]$ and $[Ca]$ in silicon and FeSi75-alloy. These relations can be seen in equation 3.28 and 3.29, and are generated using slag activities from Rein and Chipman [20] at 1550°C.

$$\gamma^{Si}_{[Al]}[wt\%Al]_{Si} = 1.34\gamma^{FeSi}_{[Al]}[wt\%Al]_{FeSi} \tag{3.28}$$

$$\gamma^{Si}_{[Ca]}[wt\%Ca]_{Si} = 1.33\gamma^{FeSi}_{[Ca]}[wt\%Ca]_{FeSi} \tag{3.29}$$

Equations 3.28 and 3.29 show that the activity of $[Al]$ and $[Ca]$ decrease with the presence of $[Fe]$.

3.3 Mass Transfer

To describe the mass transport in the ladle a conservation equation is needed. The conservation of mass is shown in equation 3.30 [12]. This equation is expressed using the Eulerian frame of reference where a control volume is fixed in spatial space and time.

$$\frac{\partial}{\partial t}\int_V \rho \; dV + \int_A (\rho \mathbf{v}) \cdot \mathbf{n} \; dA = 0 \tag{3.30}$$

Equation 3.30 describes the total change in mass for the control volume. By applying the divergence theorem and keeping the control volume constant it can be transformed into equation 3.31 if one assumes a constant volume according to Drew and Passman [26], after Reynolds decomposition and time averaging.
.

$$\sum_{p=1}^{N} (\frac{\partial}{\partial t}(\rho_k \alpha_k) + \nabla \cdot (\rho_k \alpha_k \mathbf{u}_k)) = 0 \tag{3.31}$$

Equation 3.31 describes the conservation of mass for the whole control volume.
Next one needs the conservation of mass for a single phase k which is expressed in equation 3.32. Where equation 3.31 is the sum of equation 3.32 over all the phases in the volume.

$$\frac{\partial}{\partial t}(\rho_k \alpha_k) + \nabla \cdot (\rho_k \alpha_k \mathbf{u}_k) = \sum_{p=1}^{N} (\dot{m}_{p,k} - \dot{m}_{k,p}) \tag{3.32}$$

Finally equation 3.33 for the conservation of an individual species i in a phase k is needed to complete the mass conservation equations.

$$\frac{\partial}{\partial t}(\rho_k \alpha_k \omega_i) + \nabla \cdot \dot{\mathbf{m}}_{i,k} = r_{i,k} \tag{3.33}$$

Equation 3.33 needs to be solved for every species in all of the phases. The results are then put into equation 3.32 as it is solved for every phase in the volume. At last equation 3.31 is solved using the results from equation 3.32. If relativistic effects are neglected equation 3.31 should always give zero as mass cannot be created or destroyed.

3.3.1 Reactions at the Interface

To be able to solve equation 3.33 one needs to know exactly how the reactions happen at the melt/gas and melt/slag interface. Tang [5] describes both processes as if they happen directly at the interface, as seen earlier, while Ashrafian [27] describes both processes as happening in the melt side of the adsorption interface. If the reaction front is not on the interface one must account for the effect a reaction has on

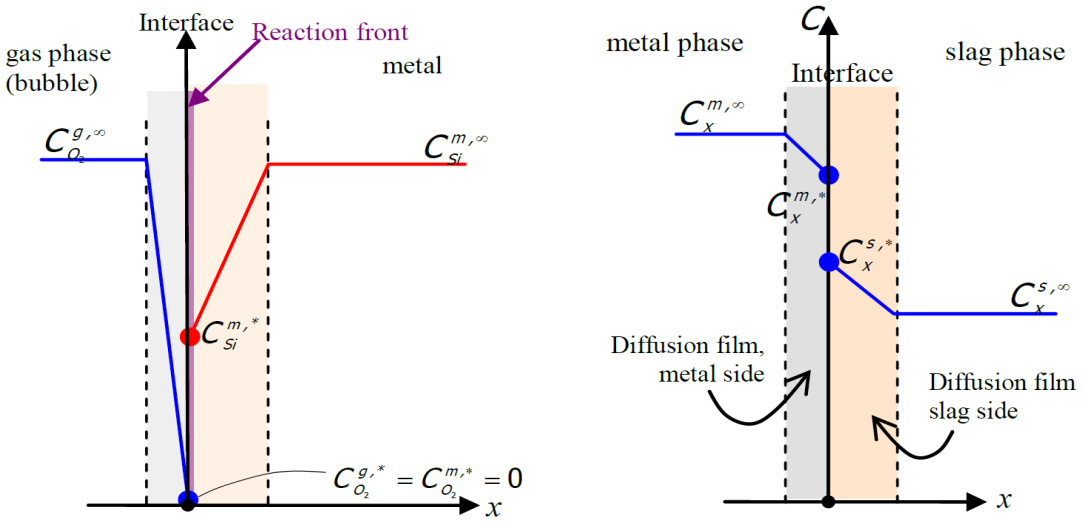

Figure 3.3.1: Melt/gas and melt/slag interfaces expressed by two-film theory. Ashrafian [27]

the diffusion of the species through the adsorption interface. One way to deal with this is to add the enhancement factor E which is defined as the fraction between mass transfer with and without reaction. The problem with E is that it is notoriously difficult to compute but Ashrafian [27] shows that can be simplified somewhat.

It must be said that even though Ashrafian [27] describes both the melt/gas and melt/slag reactions as happening at the metal side he only uses E when describing the melt/gas reactions. A reason for this might be because he states that the reaction happens just as the oxygen anions diffuse into the metal side. It can be viewed as if there is no mass transfer of oxygen in the metal phase, just a reaction when the oxygen anions enter it. Since E is the effect that a reaction has on the mass transfer it can be excluded in this case. This makes the equations for the melt/slag reactions equal for both Tang and Ashrafians descriptions. Tang [28] commented on this that it does not matter how you describe the melt/gas reaction since it is not rate limiting, and the effect an eventual E would have on the mass transfer as a whole is negligible. Since the literature on this subject is limited it is difficult to discern which of the descriptions is correct, but if E can be neglected without giving a high degree of error it should be for the purpose of simplifying the calculations. These seem to be the two dominating view on the subject, and both of the models give good results when compared to experimental data.

The reactions in the system are assumed to be instantaneous. This assumption says that the reactants cannot be present at the same time without reacting. The temperature in the ladle is so high it will drive the rapid reaction kinetics making an instantaneous reaction a reasonable assumption. Since the thickness of the interface layers are small compared to the bubble and droplet diameters the it can be approximated that the atoms see the surfaces as if they were flat allowing for two-film theory to be used for a flat surface. Using two-film theory, figure 3.3.1 and the stoichiometric coefficients for the reactions the system can be solved. Equation 3.34 gives the molar flux for the melt/slag reactions where the fluxes can be coupled to express $N_i|_{m\to s} = f(X_{[i]}, X_{(i)})$. An example of these types of expressions can be seen in equation 3.34.

$$N_i|_{m\to s} = c_m \alpha_m k_{[i]} (X_{[i]} - X_{[i]}^{\star}) = c_s \alpha_s k_{(i)} (X_{(i)}^{\star} - X_{(i)}) \tag{3.34}$$

3.3.2 The Mass Transfer Coefficient

The mass transfer coefficient k_i has the units $\frac{m}{s}$ and can be thought of as the velocity of mass transfer for a species in a specific phase film or volume. When doing experiments one usually know the concentration of a species before the experiment starts, ω_i^{in}, when it ends ω_i^{end} and at specific sampling points $[\omega_i^{sp_1}, \cdots, \omega_i^{sp_n}]$. While fitting ones data it is convenient to collect everything that can affect the mass transfer into one velocity coefficient and express the rate as a function of concentration and geometry variables with a coefficient that includes almost everything else. This has some benefits like simplifying expressions and allowing one to do calculations on systems where one might not know every parameter which affects the mass transfer or their values. It does however cause problems when k_i changes values unexpectedly or behaves in complex ways. Due to the myriad of properties and relations it could contain there is no simple way of dissecting it into its constituent terms, without extensive knowledge of the system it was used in and the assumptions the calculations were based on. Based on [29] [30] [1] [12] one can list some common properties which k_i might be a function of:

$$k_i(D_i, U_k, \mu_k, \rho_k, L, \sigma_{p,k}) \tag{3.35}$$

In transport theory and modeling it is also common to express k_i as a function of dimensionless numbers. A common expression used comes from the Blasius solution of a flat plate [29], and is shown in equation 3.36.

$$\frac{\bar{k_i}L}{D_i} = Sh = 0.664 \left(\frac{UL}{\nu_i}\right)^{\frac{1}{2}} \left(\frac{\nu_i}{D_i}\right)^{\frac{1}{3}} \tag{3.36}$$

Dimensionless numbers and their use will be discussed further later in this thesis.
A problem with equation 3.34 is that it is difficult to measure a k_i for each specific phase film. To circumvent this problem a total mass transfer coefficient $k_{i,t}$ $[\frac{m}{s}]$ can be found, combining the two films. Engh [1] takes equation 3.34 and rewrites it as equation 3.37.

$$N_i|_{m\to s} = \frac{k_{[i]}\bar{\rho}_m}{M_i}(\omega_{[i]} - \omega^\star_{[i]}) = \frac{k_{(i)}\bar{\rho}_s}{M_i}(\omega^\star_{(i)} - \omega_{(i)}) \ \ [\frac{kmol}{m^2\ s}] \tag{3.37}$$

By rewriting equation 3.37 one gets equation 3.38.

$$\omega_{[i]} - \omega^\star_{[i]} = \frac{N_i|_{m\to s}M_i}{k_{[i]}\bar{\rho}_m}, \ \ \omega^\star_{(i)} - \omega_{(i)} = \frac{N_i|_{m\to s}M_i}{k_{(i)}\bar{\rho}_s} \tag{3.38}$$

Engh [1] further assumes that the concentrations of the species i is in equilibrium at the reaction interface due to the high temperature giving rapid reaction rates. This allows one to relate the interface concentrations by the surface equilibrium distribution coefficient K_i as seen in equation 3.39 leading to the partition coefficient seen in equation 3.40.

$$K_i = \frac{\omega^\star_{(i)}\gamma_{(i)}}{\omega^\star_{[i]}f_{[i]}} \tag{3.39}$$

$$\frac{K_i f_{[i]}}{\gamma_{(i)}} = \frac{\omega^\star_{(i)}}{\omega^\star_{[i]}} \tag{3.40}$$

Using equations 3.40 and 3.38 one can get equation 3.41 representing the driving forces for mass transfer in both phases.

$$\omega_{[i]} - \frac{\omega_{(i)}\gamma_{(i)}}{K_i f_{[i]}} = N_i|_{m\to s} M_i \left(\frac{1}{k_{[i]}\bar{\rho}_m} + \frac{\gamma_{(i)}}{k_{(i)}\bar{\rho}_s K_i f_{[i]}} \right) \tag{3.41}$$

In equation 3.41 $(\frac{1}{k_{[i]}\bar{\rho}_m} + \frac{\gamma_{(i)}}{k_{(i)}\bar{\rho}_s K_i f_{[i]}})$ can be the thought as the total resistance against mass transfer between the two phases giving $k_{i,t}$.

$$\frac{1}{k_{i,t}\bar{\rho}_m} = \left(\frac{1}{k_{[i]}\bar{\rho}_m} + \frac{\gamma_{(i)}}{k_{(i)}\bar{\rho}_s K_i f_{[i]}} \right) \tag{3.42}$$

From this the molar flux $N_i|_{m\to s}$ can be expressed in terms of $k_{i,t}$.

$$N_i|_{m\to s} = \frac{k_{i,t}\bar{\rho}_m}{M_i} \left(\omega_{[i]} - \frac{\omega_{(i)}\gamma_{(i)}}{K_i f_{[i]}} \right) \tag{3.43}$$

From equation 3.43 it can be seen that dividing $\omega_{(i)}$ with the partition coefficient $\frac{K_i f_{[i]}}{\gamma_{(i)}}$ gives the hypothetical concentration of the bulk slag in equilibrium with the melt.
Engh [1] notes that equation 3.43 is not unique to a slag-melt system, but can also be used for the melt-bubble interface.
This can be written more generally for multiple volumes with different resistances against mass transfer as seen in Deckwer [30] as long as the mass transfer process is linear and any reactions present are of 1st order.

$$\frac{1}{Ress_{tot}} = \sum_{q=1}^{n} \frac{1}{Ress_q} \tag{3.44}$$

3.3.3 Ladle Refining Using $k_{i,t}$

Engh [1] presents a refining equation with a system where he assumes that both the slag and the melt are well mixed, have a constant total mass and that the contact area between all the phases is constant. He notes that these assumptions might simplify the system too much, and are difficult to attain in the real life case. It is shown here because it is still used in the literature [3], and gives good insight into the theory behind ladle refining. Equation 3.45 shows the mass balance for the system.

$$-m_m \frac{d\omega_{[i]}}{dt} = k_{i,t}\bar{\rho}_m A_s (\omega_{[i]} - \omega_{[i]}^{eq}) \tag{3.45}$$

Using the partition coefficient one gets:

$$\omega_{[i]}^{eq} K_i f_{[i]} = \gamma_{(i)}\omega_{(i)} \tag{3.46}$$

If the slag is assumed to initially not have contained the species i equation 3.47 holds.

$$m_m(\omega_{[i]}^{in} - \omega_{[i]}) = m_s\omega_{(i)} \tag{3.47}$$

Combining equations 3.45, 3.46 and 3.47 one gets the driving force for mass transfer.

$$\omega_{[i]} - \omega_{[i]}^{eq} = \omega_{[i]} \left(1 + \frac{\gamma_{(i)} m_m}{K_i f_{[i]} m_s} \right) - \frac{\gamma_{(i)} m_m}{K_i f_{[i]} m_s} \omega_{[i]}^{in} \tag{3.48}$$

This leads to:

$$min(\omega_{[i]}) = \lim_{\omega_{[i]} \to \omega_{[i]}^{eq}} (\omega_{[i]} - \omega_{[i]}^{eq}) \;\; \rightarrow \;\; \omega_{[i]} = \omega_{[i]}^{\infty} = \frac{m_m \omega_{[i]}^{in}}{m_m + \frac{K_i f_{[i]} m_s}{\gamma_{(i)}}} \tag{3.49}$$

Combining equation 3.48 and 3.49 gives equation 3.50.

$$\omega_{[i]} - \omega_{[i]}^{eq} = \left(1 + \frac{\gamma_{(i)} m_m}{K_i f_{[i]} m_s} \right) (\omega_{[i]} - \omega_{[i]}^{\infty}) \tag{3.50}$$

Introducing equation 3.50 into 3.45 gives the refining integral.

$$\int_{\omega_{[i]}^{in}}^{\omega_{[i]}} \frac{d\omega_{[i]}}{\omega_{[i]} - \omega_{[i]}^{\infty}} = - \int_0^t \frac{k_{i,t} \bar{\rho}_m A_s}{m_m} \left(1 + \frac{\gamma_{(i)} m_m}{K_i f_{[i]} m_s} \right) dt \tag{3.51}$$

When integrated equation 3.51 becomes:

$$\frac{\omega_{[i]} - \omega_{[i]}^{\infty}}{\omega_{[i]}^{in} - \omega_{[i]}^{\infty}} = exp \left(- \frac{k_{i,t} \bar{\rho}_m A_s}{m_m} \left[1 + \frac{\gamma_{(i)} m_m}{K_i f_{[i]} m_s} \right] t \right) \tag{3.52}$$

3.3.4 Slag to Metal Mass Transfer

Engh [1] expresses his model for a metal with some initial concentration of impurities that are transported into a slag. Since the experiments done in this thesis look at the transfer from slag into a clean metal the model needs to be modified somewhat. This is no large feat as the conservation of mass allows one to easily transform mass flow from metal $\rightarrow$ slag to slag $\rightarrow$ metal.
Beginning with the metal and slag balances:

$$-m_s \frac{d\omega_{(i)}}{dt} = k_{i,t} \bar{\rho}_s A_s (\omega_{(i)} - \omega_{(i)}^{eq}) \tag{3.53}$$

$$m_m \frac{d\omega_{[i]}}{dt} = k_{i,t} \bar{\rho}_m A_s (\omega_{[i]}^{eq} - \omega_{[i]}) \tag{3.54}$$

Adjusting equation 3.47 for this system where $\omega_{[i]}^{in} = 0$ gives:

$$m_s (\omega_{(i)}^{in} - \omega_{(i)}) = m_m \omega_{[i]} \tag{3.55}$$

$$\omega_{(i)} = \omega_{(i)}^{in} - \frac{m_m}{m_s} \omega_{[i]} \tag{3.56}$$

If equation 3.55 holds true then equation 3.57 must also be true, due to conservation, giving:

$$-m_s \frac{d\omega_{(i)}}{dt} = m_m \frac{d\omega_{[i]}}{dt} \tag{3.57}$$

$$\bar{\rho}_s(\omega_{(i)} - \omega_{(i)}^{eq}) = \bar{\rho}_m(\omega_{[i]}^{eq} - \omega_{[i]}) \tag{3.58}$$

Using this with $\omega_{(i)}^{eq} = \frac{K_i f_{[i]} \omega_{[i]}}{\gamma(i)}$ and the previous equations it can be seen that:

$$\omega_{[i]}^{eq} - \omega_{[i]} = \frac{\bar{\rho}_s}{\bar{\rho}_m} \left[(\omega_{(i)}^{in} - \frac{m_m}{m_s}\omega_{[i]}) - \frac{K_i f_{[i]} \omega_{[i]}}{\gamma_{(i)}} \right] \tag{3.59}$$

$$= \frac{\bar{\rho}_s}{\bar{\rho}_m} \left[\omega_{(i)}^{in} - \left(\frac{m_m}{m_s} + \frac{K_i f_{[i]}}{\gamma_{(i)}} \right) \omega_{[i]} \right] \tag{3.60}$$

$$\tag{3.61}$$

As one wants to express $\frac{d\omega_{[i]}}{dt}$ by $\omega_{[i]}^{\infty} - \omega_{[i]}$ equation 3.49 can be turned on its head to get equation 3.62.

$$max(\omega_{[i]}) = \lim_{\omega_{[i]} \to \omega_{[i]}^{eq}} (\omega_{[i]}^{eq} - \omega_{[i]}) \quad \rightarrow \quad \omega_{(i)}^{in} = \left(\frac{K_i f_{[i]}}{\gamma_{(i)}} + \frac{m_m}{m_s} \right) \omega_{[i]}^{\infty} \tag{3.62}$$

This gives

$$\omega_{[i]}^{eq} - \omega_{[i]} = \frac{\bar{\rho}_s}{\bar{\rho}_m} \left(\frac{K_i f_{[i]}}{\gamma_{(i)}} + \frac{m_m}{m_s} \right) (\omega_{[i]}^{\infty} - \omega_{[i]}) \tag{3.63}$$

Which leaves one with the relation:

$$m_m \frac{d\omega_{[i]}}{dt} = k_{i,t} \bar{\rho}_s A_s \left(\frac{K_i f_{[i]}}{\gamma_{(i)}} + \frac{m_m}{m_s} \right) (\omega_{[i]}^{\infty} - \omega_{[i]}) \tag{3.64}$$

Giving the integral:

$$\int_0^{\omega_{[i]}} \frac{d\omega_{[i]}}{\omega_{[i]}^{\infty} - \omega_{[i]}} = \int_0^t \frac{k_{i,t} \bar{\rho}_s A_s}{m_m} \left(\frac{K_i f_{[i]}}{\gamma_{(i)}} + \frac{m_m}{m_s} \right) dt \tag{3.65}$$

Finally giving the solution:

$$\omega_{[i]}(t) = \omega_{[i]}^{\infty} \left[1 - exp \left(-\frac{k_{i,t} \bar{\rho}_s A_s}{m_m} \left(\frac{K_i f_{[i]}}{\gamma_{(i)}} + \frac{m_m}{m_s} \right) t \right) \right] \tag{3.66}$$

3.4 Dimensional Analysis and Dimensionless Numbers

Using dimensional analysis one can describe the characteristics of a system by reducing the physical dimensions of its variables into dimensionless form. This is done by creating dimensionless numbers, or groups, derived using the systems characteristic properties and physical correlations between its unit dimensions. The applications of dimensionless numbers are many, were some of their common uses are: simplifying equations and diagrams, describing/finding dominant parameters, scaling a system while still retaining its physical similarities.
An important theorem in dimensional analysis is "The Buckingham π theorem" [31]. It states that a complete physical equation can be written as:

$$f(Q_1, Q_2, \cdots Q_n) = 0 \tag{3.67}$$

With n physical variables $Q_1, \cdots, Q_n$, and can be expressed using a minimal number of i dimensionless groups $\Pi_1, \cdots, \Pi_i$ as:

$$\psi(\Pi_1, \cdots \Pi_i) = 0 \tag{3.68}$$

with

$$\Pi_i = \prod_{p=1}^{n} Q_p^{a_p} \tag{3.69}$$

where the exponents $a_1, \cdots a_n$ must satisfy the equation:

$$[Q_1^{a_1} \cdots Q_n^{a_n}] = [1] \tag{3.70}$$

If k is the number of arbitrary fundamental units needed as a basis to describe the system $[Q_1], \cdots, [Q_n]$ then:

$$i = n - k \tag{3.71}$$

Using this on a simple system where one has mass transfer of one component A, from a fluid stream to a surface Lobo and Kolbeinsen [29] show that the system can be described by six independent dimensionless groups instead of the ten variables needed otherwise. They do this by listing the variables needed with their units:

k_A	$\omega_A - \omega_{As}$	x	y	U	D_A	ν	ρ	L	$\omega_{A,\infty} - \omega_{As}$
$\frac{m}{s}$	$\frac{kg\ A}{kg}$	m	m	$\frac{m}{s}$	$\frac{m^2}{s}$	$\frac{m^2}{s}$	$\frac{kg}{m^3}$	m	$\frac{kg\ A}{kg}$

There are 10 variables with 4 unique units giving 6 independent dimensionless groups. Using the variables from Lobo and Kolbeinsen one can create dimensionless groups by using physical relations and the Buckingham π theorem like in equation 3.72.

$$k_A = f(U, D_A, \nu, \rho, L) = C_1 U^{a_1} D_A^{a_2} \nu^{a_3} \rho^{a_4} L^{a_5} \tag{3.72}$$

While one can construct any 6 independent dimensionless groups the ones chosen by Lobo and Kolbeinsen [29] were:

1. The Schmidts Number: $Sc = \frac{\nu}{D}$
2. The Reynolds Number: $Re = \frac{UL}{\nu}$
3. The Sherwood Number: $Sh = \frac{k_A L}{D}$
4. Dimensionless concentration: $\omega_A = \frac{\omega_A - \omega_{As}}{\omega_{A,\infty} - \omega_{As}}$
5. Dimensionless position in x- and y-dir: $x^\star = \frac{x}{L},\ y^\star = \frac{y}{L}$

Choosing useful dimensionless groups is important, but from the list one can see that Lobo and Kolbeinsen [29] relate the concentration and positions to their respective characteristic properties. Sc relates the viscous and mass diffusivity, Re describes the outer against the inner forces of a flow, and Sh relates the total mass transfer against the diffusive mass transfer. Knowing these dimensionless groups allows one to check if two systems are similar by comparing their values against each other. Similar systems should perform equal in their similarity space. This knowledge allows one to scale a system in different dimensions while retaining its properties as long as similarity is upheld.

A simple example of this is if you have two people standing on each side of a ball pushing against it. From this one gets the force balance in $x-dir$ as seen in equation 3.73.

$$F_{tot} = F_1 - F_2 = m_1 a_1 - m_2 a_2 \tag{3.73}$$

Let us assume one is only interested in three cases:

1. The ball holds its position $\rightarrow \;\; F_1 = F_2 \;\; \rightarrow \;\; \frac{F_1}{F_2} = 1$
2. The ball moves towards the right $\rightarrow \;\; F_1 > F_2 \;\; \rightarrow \;\; \frac{F_1}{F_2} > 1$
3. The ball moves towards the left $\rightarrow \;\; F_1 < F_2 \;\; \rightarrow \;\; \frac{F_1}{F_2} < 1$

From this one can see that the three cases can be expressed as the dimensionless quantity $\frac{F_1}{F_2}$. The benefit of expressing the system this way is that the quantity $\frac{F_1}{F_2}$ allows one scale the system and still expect the same result. This can be seen if one always want the ball to go toward the right. In this case one can increase or decrease F_1 or F_2 as long as $\frac{F_1}{F_2} > 1$ holds.
While this is a simple system it does show one of the pitfalls using this method. If one increased F_1 and F_2 too much then the ball would rupture and get crushed due to the exterior pressure. While making F_1 and F_2 too big might be disastrous, making them too small might also pose certain problems. A changing environment might also pose problems. The quantity $\frac{F_1}{F_2}$ will probably not be the important factor if one stood in a hurricane. This illustrates the fact that different physical properties might dominate at different dimension scales, often called dimensional regimes, or in different systems, and that one has to account for these effects when doing system scaling. While there are limitations on the use of dimensional analysis it is still a useful tool when describing systems.

3.5 Bubbles

3.5.1 Bubble Size

The size of a bubble in a stagnant liquid can be determined using gibbs free energy. To illustrate this one can look at air bubbles created by a straw in water. By creating a gas flow through the straw a pressure is exerted by the gas on the liquid/gas interface. The pressure does work on the interface stretching it. As the pressure grows the surface is stretched more and more forming the bubble. The work done over the surface to increase its area increases the surfaces energy density signifying a change in the systems free energy. If the net gas flow becomes zero the bubble radius should be stable giving no change in free energy leading to $\frac{dG}{dr} = 0$. Now if the bubble radius was to decrease by an infinitesimal amount dr then this would also lower the bubbles surface energy density. To counteract this the pressure inside the bubble must increase. Pashley and Karaman [32] write that this change in dr can be expressed as:

$$dG = -\sigma(4\pi r^2 - 4\pi(r-dr)^2) + (P_b - P_l)4\pi r^2 dr \tag{3.74}$$

$$-8\pi r dr\sigma + \Delta P 4\pi r^2 dr \tag{3.75}$$

When applying the equilibrium condition $\frac{dG}{dr} = 0$ to equation 3.75 gives:

$$-8\pi r\sigma + \Delta P 4\pi r^2 = 0 \tag{3.76}$$

Leading to the Laplace equation 3.77.

$$\Delta P = \frac{2\sigma}{r} \tag{3.77}$$

Equation 3.77 can be expanded for any curved interface using the two principal radii of curvature as seen in equation 3.78 [32].

$$\Delta P = \sigma(\frac{1}{R_1} + \frac{1}{R_2}) \tag{3.78}$$

3.5.2 Bubble Diameters

Bubbles in a flow are not necessarily spherical. Grace [33], later expanded in Grace et al. [34], gathered data from multiple sources under a wide range of operating conditions to create a geometric framework for the shapes of bubbles rising in infinite fluids. Even though the bubbles are not spherical it is still common in the literature to use bubble and particle diameters, so before tackling the bubble shapes this will be explained.

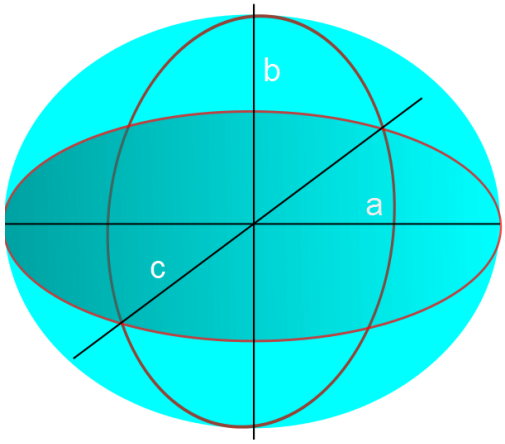

Figure 3.5.1: An ellipsoid with semi principal axis lengths of a, b and c

In the literature it is usual to express bubbles by their sphere equivalent diameters [33] to correct for their deviation from an ideal sphere [29]. The bubble geometry tends to exibit a high degree of sphericity [29] so relating an object that may have complex geometries and topographies to one with a smooth surface and diameter is preferable. To get a representative equivalent diameter for a bubble swarm or a subset/range of one averages or means are often used. Deckwer [30] writes that if one uses a photographic method at least 500 bubbles must be measured to give a reliable average, which is in agreement with the ASTM standard for measuring particle sizes [35].

Since these equivalent diameters relates an objects properties and behavior to another object it is important to use the one that gives the best representation of the original system. The equivalent sphere should exhibit a high degree of physical similarity with the original object to constitute the same criteria for the desired characteristics. If one wants to read more about this Sauter [36] covers it quite well.

While there are multiple ways of generating different sphere equivalent diameters this author has found that the most commonly used are the volume equivalent sphere diameter and the sauter diameter. The volume equivalent sphere diameter, seen in equation 3.79, is for instance used by Grace [33].

$$d_e = (\frac{6V_b}{\pi})^{\frac{1}{3}} \tag{3.79}$$

d_e is here the diameter of a sphere that has the same volume as the bubble. It has the benefit of being independent of bubble shape and instead relates directly to the bubbles volume. The problem or benefit with this relation is that it does not take into account the surface area. Measuring the surface area of non-spherical objects can be quite difficult. Depending on the objects degree of sphericity and how important the area is for ones calculations one might need to choose another equivalent diameter.

If one looks at an ellipsoid, as seen in figure 3.5.1, it has a volume expressed by equation 3.80. The ellipsoids surface area is shown in equation 3.81, where $F(\sqrt{\delta}|\frac{\varepsilon}{\delta})$ and $E(\sqrt{\delta}|\frac{\varepsilon}{\delta})$ are the incomplete elliptic integrals of the first and second kind.

$$V = \frac{4\pi}{3}abc \tag{3.80}$$

$$A_s = 2\pi c^2 + \frac{2\pi ab}{\sqrt{\delta}}[(1-\delta)F(\sqrt{\delta}|\frac{\varepsilon}{\delta}) + \delta E(\sqrt{\delta}|\frac{\varepsilon}{\delta})] \tag{3.81}$$

$$\delta = 1 - \frac{c^2}{a^2}, \quad \varepsilon = 1 - \frac{c^2}{b^2} \tag{3.82}$$

While equation 3.81 looks difficult it can be solved, but it is an example of how it can be difficult to calculate the surface are of "simple" geometric shapes.
To include the effects of the surface area Sauter [36] proposed the sphere equivalent diameter, later named after him. The sauter diameter, as seen in equation 3.83, is the sphere equivalent diameter of a sphere that has the same volume to surface area ratio as the bubbles.

$$d_{SD} = \frac{6V_b}{A_s} = \frac{d_e^3}{d_s^2} \tag{3.83}$$

It combines the volume and surface area equivalent sphere diameters, seen in equation 3.79 and 3.84 respectively.

$$d_s = (\frac{A_s}{\pi})^{\frac{1}{2}} \tag{3.84}$$

The benefit of using the sauter diameter is that it takes into account the surface area and volume which is beneficial when looking at reactions and mass transfer. The downside is that it is difficult to generate, but this is eased somewhat by standard approximations and practices for these types of measurements [35].
Sauter [36] meant for his diameter to be used as a mean bubble diameter. For the general case the ASTM standard [35] for calculating a mean particle diameter is:

$$d_{pq} = \left[\frac{\sum_i n_i d_i^p}{\sum_i n_i d_i^q}\right]^{\frac{1}{p-q}}, \quad p \neq q \tag{3.85}$$

$$d_{pq} = \left[\frac{\sum_i n_i d_i^p ln(d_i)}{\sum_i n_i d_i^q}\right], \quad p = q \tag{3.86}$$

From equation 3.85 one can see that the sauter mean diameter is equal to d_{32} and the volume equivalent mean sphere diameter becomes d_{30}.

3.5.3 Bubble Shapes in Flow

According to Grace [33] the relevant physical quantities of a bubble rising at terminal velocity U in an infinite Newtonian fluid are:

$$F(g, \rho_c, \mu_c, \sigma, \rho_d, \mu_d, d_e, U) = 0 \tag{3.87}$$

By using the Buckingham π theorem one can transform equation 3.87 to 3.88.

$$F(Re, Eo, Mo, \kappa, \gamma) = 0 \tag{3.88}$$

where:

- Reynolds number: $Re = \frac{\rho_c d_e U}{\mu_c}$
- Eötvös number: $Eo = \frac{g d_e^2 (\rho_c - \rho_d)}{\sigma}$
- Morton number: $Mo = \frac{g \mu_c^4 (\rho_c - \rho_d)}{\rho_c^2 \sigma^3}$
- Viscosity ratio: $\kappa = \frac{\mu_d}{\mu_c}$
- Density ratio: $\gamma = \frac{\rho_d}{\rho c}$

κ and γ tend to be small for gas bubbles rising in liquids, and Haberman and Morton [37] found that the viscosity and density of the dispersed fluid phase can be neglected in determining the bubbles properties.

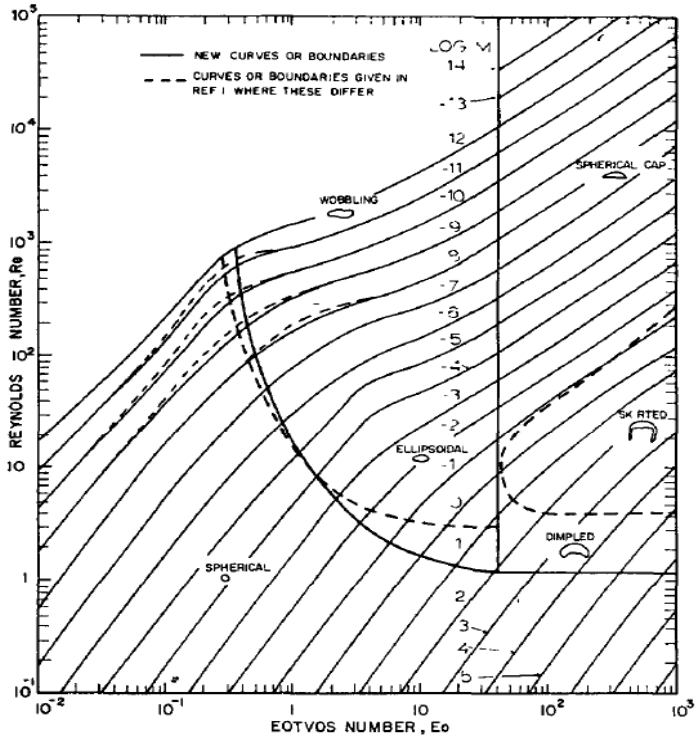

Figure 3.5.2: Grace diagram showing the bubble shape regimes with respect to Re, Eo and Mo. Grace et al. [34].

By neglecting κ and γ it is sufficient to only consider Re, Eo and Mo in equation 3.88. Using experimental data from multiple sources over large ranges of parameters Grace [33] created a diagram showing the bubble shape regime at specific values of Re, Eo and Mo. Figure 3.5.2 shows the grace diagram where Re is plotted a function of Eo and Mo. This diagram does not apply when $\rho_d >> \rho_c$ or $\mu_d >> \mu_c$ [34]. Grace [33] describes three primary bubble shape regimes, as can be seen in figure 3.5.2. These are spherical, ellipsoid and spherical-cap. From figure 3.5.2 one can see that high surface energy density and the predominance of viscous over inertial forces promote the minimization of surface area giving spherical bubbles. When the viscous forces dominate enough, giving a very low Re, it does not seem to matter how low the surface energy density is, since the bubbles will always be spherical regardless of Eo or Mo. At somewhat large values for Re end intermediate values of Eo the bubbles will be ellipsoidal. If Mo becomes too small tho one tends to see shape irregularities giving wobbling shapes [33]. Grace [33] notes that the boundary between spherical and ellipsoidal bubbles is difficult to discern since it is not well defined. This comes from a scarcity of available data and how far one is willing to stretch the definition of a sphere before it becomes an ellipsoid is arbitrary [33]. The concentration of surface active contaminants has also an effect on the bubble deformation [38, As read in [33]], which Grace et al. [34] attribute to the higher velocities in pure fluids. Grace [33] writes that the boundary in figure 3.5.2 is thought to represent a reasonable estimate of when the ratio of minor to major semi-axis is about 0.9. When both Eo and Re are high the bubbles enter the spherical-cap regime. According to Grace [33] the spherical-cap regime has well-defined boundaries between the other regimes. Grace et al. [34] writes that the spherical-cap regime can be divided into sub regimes. These depend on the shape of the bubbles rear, which can be flat dimpled or skirted.

3.5.4 Bubble Sizes in Turbulent Flow

When the flow has an $Re > 2300$ it becomes turbulent [29]. When a bubble moves in a turbulent flow its size is determined by the balance between surface tension forces and turbulent fluctuation forces [39]. Hinze [39] writes that if the Weber number, $We = \frac{\rho_c U^2 d}{\sigma}$, for a bubble is larger then some critical We, We_{crit}, it will break up into smaller bubbles. As long as $We \gg We_{crit}$ Hinze proposes:

$$We_{crit} = C\left[1 + \varphi(Oh)\right] \tag{3.89}$$

where C is a constant, $\lim_{Oh \to 0} \varphi(Oh) = 0$ and Oh is the Ohnesorge number:

$$Oh = \frac{\mu_d}{\sqrt{\rho_d \sigma \, d_b}} \tag{3.90}$$

Hinze [39] writes that if the breakup is assumed to happen due to the kinetic energy of turbulent fluctuations We_{crit} can be written as:

$$We_{crit} = \frac{\rho_c \bar{U}^2 d_{max}}{\sigma} \tag{3.91}$$

If one assumes isotropic homogeneous turbulence the turbulent dissipation rate, ε, will determine the turbulence pattern. Using the Kolmogoroff energy distribution law

$$\bar{U}^2 = C_{Kolm} \left(\varepsilon d\right)^{\frac{2}{3}} \tag{3.92}$$

Hinze [39] uses equation 3.89 with the condition $Oh \ll 1$ giving:

$$d_{max} = C \left(\frac{\sigma}{\rho_c}\right)^{\frac{3}{5}} \varepsilon^{-\frac{2}{5}} \tag{3.93}$$

Calderbank [40] later expands on this creating equation 3.94, as written by Olsen et al. [41], for the equilibrium bubble size in turbulent flow.

$$\bar{d}_{SD} = C_1 \alpha_d^n \left[\frac{\sigma^{0.6}}{\varepsilon^{0.4} \rho^{0.6}}\right] \left(\frac{\mu_d}{\mu_c}\right)^m + C_2 \tag{3.94}$$

Olsen et al. [41] adopted $n = 0.5$ and $m = 0.25$ as it fit with data from different authors. C_1 and C_2 are tuning parameters, where $C_1 = 4.0$ and $C_2 = 1.0 \cdot 10^{-3}$ was used for bubbles. From equation 3.94 one can see that C_2 can be though of as an initial bubble size. Using equation 3.94 one can get a bubble size which can be used as an equilibrium condition in other models where the bubble sizes change dynamically in a control volume. This can come from a more advanced bubble dispersion model, like the one proposed by Laux and Johansen [42].

3.5.5 Bubbles Through a Porous Plug

The purge gas enters the *Si* refining ladle through a porous plug located at the bottom of the ladle. A porous plug is made of a refractory material and can be viewed as a series of small tubes with gas flowing through them. When the gas comes into contact with the melt a gas pocket is formed. The formation and geometry of the gas pocket is due to the surface energy density $\sigma_{k,p}$ between the different phases. As more gas arrives the pressure in the gas pocket increases until it reaches a critical size and lets go of the plug creating a bubble. The problem with molten silicon is that it does not wet the refractory material giving $\sigma_{m,plug} > \sigma_{m,b},\ \sigma_{b,plug}$. This leads to a low contact angle θ, as seen from equation 3.95.

$$\sigma_{m,plug} = \sigma_{b,plug} + \sigma_{m,b} cos(\theta) \tag{3.95}$$

With a high degree of wetting, θ will be large giving the bubble a diameter close to the pore diameter. Under non wetting conditions the bubbles become much larger due to increased spreading of the gas phase over the plug. Increased spreading of the gas pockets makes it possible for coalescence. If this happens the smaller pockets will merge into bigger gas pockets. Under certain conditions they may even coalesce into a gas pocket which which covers the entire plug. These pockets will be unstable releasing bubbles of different sizes as they grow. When they become large enough the gas pockets will detach creating large bubbles that float to the top, as seen in 3.5.3. A large degree of coalescence is detrimental to the refining process and must be avoided at all costs, due to the massive decrease in melt to gas surface area.

The criterion for coalescence is known to vary with different plug designs, gas flow rates, gas composition and bulk melt composition. Anagbo and Brimacomb [43] have done experiments in water and found that, for their system, flow rates above 16 $[\frac{cm^3}{s\ cm^2}]$ cause some degree of coalescence, and above 40 $[\frac{cm^3}{s\ cm^2}]$ the gas pocket is big enough to cover the whole plug.

Even though certain difficulties are associated with porous plugs they still provide benefits over nozzles or tuyeres. Nozzles require very high gas flow rates to prevent back flow while porous plugs allow for lower gas flow rates. When one wants to facilitate reactions, like in ladle refining, too high of a gas flow rate is detrimental due to a low residence time of the bubbles. Porous plugs also have the benefit of generating smaller bubbles compared to nozzles, increasing the liquid to gas surface area and thus the refining rate.

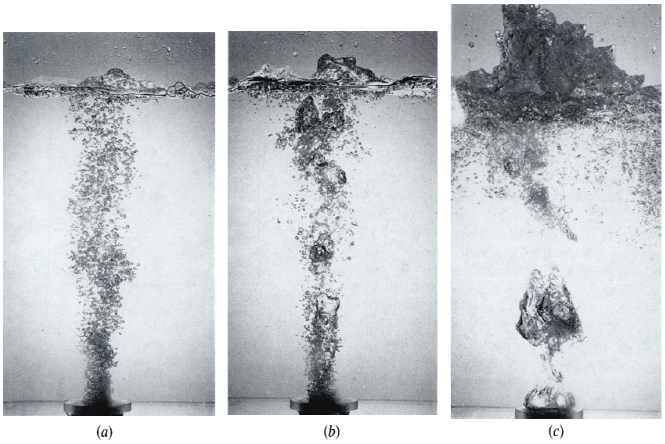

Figure 3.5.3: Modes of gas dispersion in porous plug injection: (a) discrete bubbles, (b) incipient coalescence, and (c) coalescence. Anagbo and Brimacomb [43]

3.5.6 Bubble Column Reactors

The oxidative ladle refining process is in principle a chemical bubble column reactor. Chemical bubble column reactors are widely used due to their excellent heat and mass transfer characteristics and low operating costs [44]. While different bubble column reactors may vary they are in principle a cylinder with a gas distributor, usually placed at the bottom [12], as seen in figure 3.5.4.

The gas phase is dispersed as bubbles while injected through the gas distributor into the liquid phase. As the bubbles rise through the reactor they entrain the liquid carrying it upwards. The liquid velocity at the center of the bubble column is comperable to the bubbles rise velocity [30]. While the entrained liquid gets displaced upwards it induces a counter flow of liquid along the walls to satisfy the overall conservation. The liquid moving downward will also carry with it some of the small bubbles for a certain distance [30]. This characteristic up and down flow creates a circular flow pattern representative to the system. The difference in phase velocities will also contribute to the radial exchange flow. As a bubble rises it must push the fluid elements in front of it to the side, and in its wake those behind it are drawn inn. Together the radial exchange flow from the circular flow and different phase velocities give rise to a high degree of inter radial mixing, causing there to be practically no radial liquid concentration gradients. Despite a high rate of radial intermixing the mean liquid axial velocity profiles have been found to be relatively stable with a general shape [45] shown in figure 3.5.5.

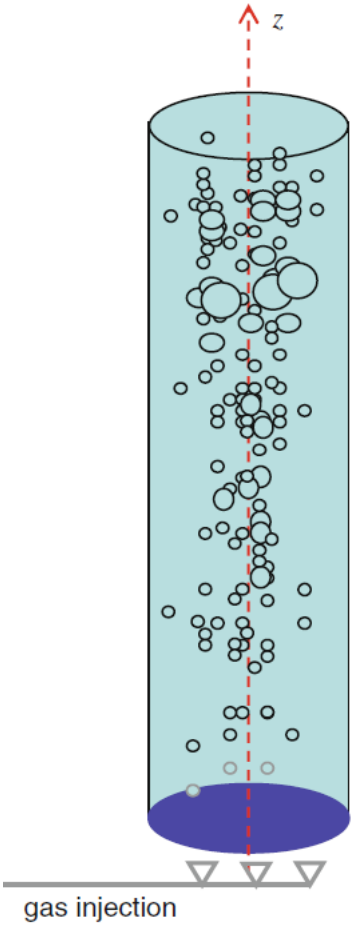

Figure 3.5.4: A figure showing the simplest form of a bubble column reactor. From Jakobsen [12]

Despite an initial uniform gas distribution a radial velocity and gas hold up profile will form. This comes from the fact that the bubble sizes in the column are not uniform, but rather belong to a size population, where in particular the larger bubbles and the entrained liquid together tend to rise at the center of the column [30]. Coalescence is also a phenomenon that must be considered, allowing for a wider range of bubble sizes depending on multiple process parameters.

A bubble column reactor will display significantly different behaviors depending on the flow conditions, giving rise to three distinct flow regimes [30], shown in figure 3.5.6. When the gas velocity is low the bubble size distribution is roughly uniform with an almost constant rise velocity for the bubbles and a close to constant gas distribution. This flow regime is called homogeneous or bubbly flow. As the gas rate increases the homogeneous bubble distribution will become unstable. The smaller bubbles will start to coalesce forming larger bubbles. These secondary bubbles will have a higher rise velocity then their smaller counterparts. This flow regime with a large range of bubble sizes is called the heterogeneous, turbulent or churn-turbulent region. If the reactor diameter is small($\approx< 20\ cm$) [30] while under heterogeneous flow conditions the walls can stabilize large elongated bubbles known as slugs. These slugs will collect the smaller bubbles continuously as they rise expanding until they obtain a cross section close to the reactor diameter.

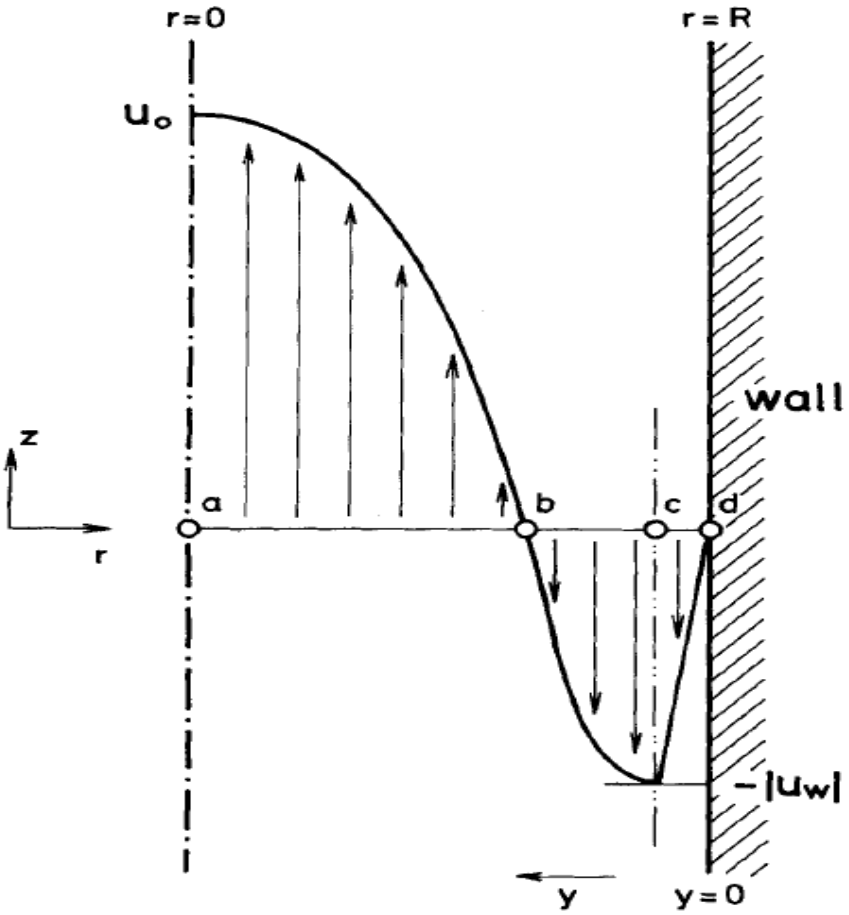

Figure 3.5.5: General shape of the flow pattern for the liquid in a bubble column. From Ueyama et al. [45].

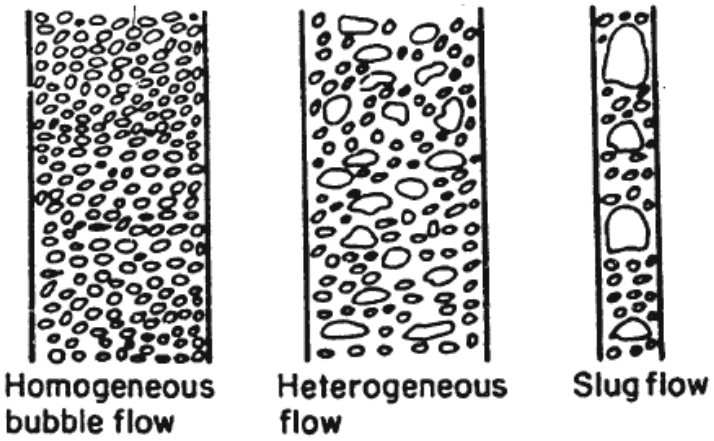

Figure 3.5.6: Different flow regimes in a bubble column reactor. From Deckwer [30].

While the flow regime is heavily dependent on the gas velocity there are other important factors. The dimentions of the reactor, expecially the diameter, can have a large impact as seen from slug flow. Deckwer et al. [46] shows how the effect of wall retardation on a bubble flow can be represented. This is shown in figure 3.5.7 where Kantarci et al. [44] has cleaned up the figure from Deckwer et al. It must be noted that figure 3.5.7 is not made dimensionless, so its values should not be used without checking for similarity, but rather as a visualization of how the terminal velocity and reactor diameter affect the flow regime.

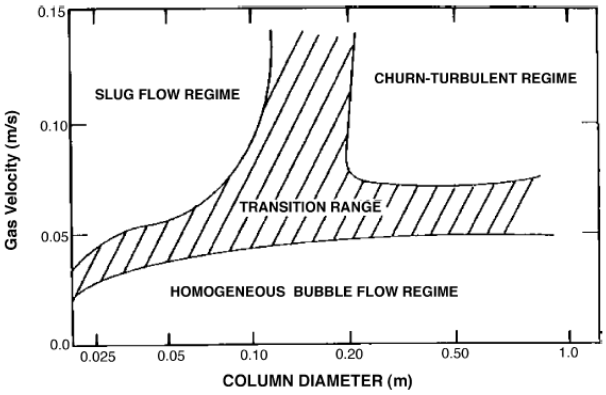

Figure 3.5.7: Velocity and reactor diameter for a flow with a set bubble diameter.From Kantarci et al. [44] based on figure from Deckwer et al. [46]

Clift et al. [47] uses data from various sources to express the influence of wall retardadion on a bubble flow. This is done by comparing the terminal bubble velocity in the reactor to the terminal bubble velocity in an infinte container, $\frac{U_T}{U_{T\infty}}$ as the diameter ratio $\lambda = \frac{d_e}{D}$ changes. For $Eo < 40$, $Re > 200$ and $\lambda \leq 0.6$, using data from Salami et al. [48, As read in [47]], Uno and Kintner [49], and Strom and Kintner [50], Clift et al. [47] proposes:

$$\frac{U_T}{U_{T\infty}} = (1-\lambda^2)^{\frac{3}{2}} \tag{3.96}$$

From these data he proposes that one can neglect wall effects when the error $<$ 2%. This occurs when:

$$Re \geq 100, \quad \lambda \leq 0.12 \tag{3.97}$$

When $Eo \geq 40$ Clift et al. [47] writes that wall effects can be ignored as long as $\lambda \leq 0.125$ for spherical-caps when Mo is low, based on data from Collins [51] [52, As read in [47]]. For $\lambda \geq 0.125$ Wallis [53] proposes to use equation 3.98 which Clift et al. [47] confirms fits well with the data from Collins.

$$\frac{U_T}{U_{T\infty}} = 1.13e^{-\lambda}, \quad 0.125 \leq \lambda \leq 0.6 \tag{3.98}$$

Grace [33] writes about wall retardation on rising bubbles based on their shape regime. He gathers data from other authors and proposes based on this the limits for λ where one can neglect wall effects.

- $\frac{d_e}{D} \leq 0.2$ for spherical caps. Collins [52, As read in [33]].
- $\frac{d_e}{D} \leq 0.113$ for ellipsoidal bubbles. Harmathy [54].
- $\frac{d_e}{D} \leq 0.074$ for spherical bubbles. Haberman and Sayre [55].

Grace [33] writes that if one follows these limits the maximum wall retardation is expected to be of the order of 3% for spherical caps [52, As read in [33]], 4% for ellipsoidal bubbles [54], and 15% for spherical bubbles [55].

From this it can be seen that the bubbles are affected by multiple parameters through Eo, Mo, Re and λ. Luckily for metallurgists it seems that molten metals tend to exhibit the same properties as conventional liquids [47]. From Tang [5] one can see that molten silicon is a low viscosity liquid, like water, with a density in the same order of magnitude of water as well. Based on this one can create systems where one should expect similarities in phase and/or flow behavior.

3.6 Analytical Techniques

It is deemed as important, by this author, to give the reader an overview of theory behind the analytical techniques used for sample analysis in the experimental portion later in this thesis. It is meant to paint the reader a picture of how the techniques work, and under which conditions they take place. This transparency allows the reader to go into the experiment portion with an informed mind to better judge its contents.

3.6.1 ICP-MS

ICP-MS is an analytical technique where one combines a high temperature inductively coupled plasma source(ICP) with a mass spectrometer(MS) to determine quantities of trace elements in solids or liquids. The ICP ionizes the elements in the sample and after the ions are separated they are detected by the MS. Figure 3.6.1 gives a basic overview of the apparatus and the process steps. Samples analyzed by ICP-MS are usually prsent in liquid form, or as a solid dissolved into one. This liquid is then aspirated into a nebulizer converting it and Ar gas into an aerosol. If one cannot dissolve a solid sample one might be able to heat it up in an Ar atmosphare using a laser to form an aerosol directly [56]. The aerosol is then transferred into the ICP torch chamber. Inside this chamber there are load coils that generate an oscillating electric and magnetic field. Ar is injected and subjected to a spark stripping away some of its electrons forming Ar-ions. As these ions are caught in the oscillating field they collide with other Ar atoms forming a plasma with temperatures in the range of 6000-10000K [56]. The aerosol sample is then injected into the plasma where it too gets ionized. It is important to note that the ions formed by the ICP plasma are typically positive ions, M^+/M^{2+}, making elements that form negative ions very difficult to detect [56].
From the ICP torch chamber the sample is filtered and cooled. The flow is driven by a lower pressure in the filters which is decreased by each filter step. Wolf [56] writes that the torch chamber is approximately under atmospheric pressure while the MS, which comes after the filters, has a pressure $\sim< 1.3 * 10^{-8}$ *bar*. Some of these filters consist of metal disks with small holes i the center(1mm) [56]. Due to the narrow diameter of these holes Wolf [56] writes that it is not recommended to have more then 0.2% of total dissolved solids in the sample. This is to prevent blockage of the filters which decreases sensitivity and detection capability.
The ions, which are positively charged, are then focused by positively charged electrostatic lenses so the ion beam may enter the MS. A commonly used MS technique is the quadrupole mass spectrometer. Here four rods are arranged as in figure 3.6.1. By applying alternating AC and DC voltages to opposite paired rods and switching them rapidly under a radio frequency field only a specific mass to charge ratio is allowed through. Different voltages allow different mass to charge ratios through giving the amount of an element at each step. While this might seem slow according to Wolf [56] the filter can separate up to $2400\frac{amu}{s}$ and has a typical resolution ranging between $0.7 - 1.0$ *amu*. Other types of MS can also be used like magnetic mass spectrometers to give better resolution but at the cost of other properties.

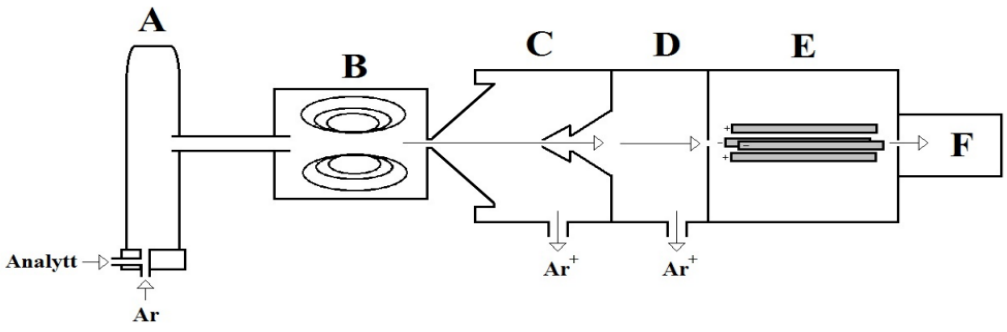

Figure 3.6.1: A) Nebulizer, B) ICP Torch, C-D) Filters, E) Quadrupole Mass Filter, F) Detector. From Galteland and Bjørnstad [57].

Chapter 4

Bubble Column Reactor Proposal

Earlier in this thesis the literature on scaling a system with respect to bubble size was presented. From this one can construct a cold model expecting the same behavior tendencies as the industrial system. The experiment presented here aims to measure initial bubble sizes in the central bubble column and how they change as they rise. Other behaviors will not be considered here.
Elkem has been generous enough to supply industrial porous plugs and disclosed some of their operation parameters to the author for experimental use. They do not however want the specification and information to go public at this point. To adhere to their wishes non of the experimental specifications will be provided, which could allow one to calculate these specific system properties. While the specifics might not always be this authors to share the experimental concept and considerations should still give a good overview.
A schematic representation of the reactor can be seen in figure 4.0.1. The reactor is, in its simplest form, a transparent glass fiber box with the ability to fasten a porous plug at the bottom, venting the output gas through the top. Due to the weight of the plug and liquid combined a sturdy steel frame is advised to carry the apparatus. The cage containing the plug should be welded to the frame since it is quite heavy, and if not secured well could slip out of the reactor spilling its contents, and thus being a large safety hazard. The bubble sizes can be measured using a high speed camera as the reactor wall material is transparent. At least 500 bubbles need to be measured to get a good average, as is advised by the ASTM standard for particle size measurements [35]. If one sees bubbles with high degree of asymmetry a pair of cameras should be used, at two different sides, to capture the topography and volume better, since normal commercial cameras do not register depth information. A pair of cameras can also be used together with commercial image recognition software to count bubbles, measure diameters and volumes, etc...
The reactor geometry considered by Olsen et al. [41], when modeling, had a lower ladle diameter of 1.04m, where the plug diameter was 0.08m. Their inlet sauter bubble diameter was 0.01m. Due to not being able to share the actual experiment geometries this will be used as a model system. This system has a $\frac{d_e}{D} < 9.6 \cdot 10^{-3}$, and is expected from the literature to not contain any wall retardation effects.
From the literature one can deduce that if no wall retardation is desired $\frac{d_e}{D} \leq 0.074$ is enough to cover all bubble shapes, as long as Mo is low. Assuming $\rho_d \gg \rho_c$ gives $Mo = \frac{g\mu_c^4}{\rho_c \sigma^3}$. Tang [5] writes that $\mu_m(T = 1873K)|_{p=1atm} \approx 6 \cdot 10^{-4}$ $[Pa\ s]$, which agrees with experimental results from Assael et al. [58]. Bjørnstad [2] collected multiple expressions for ρ_m from various authors and showed that $\rho_m(T = 1873K)|_{p=1atm} \approx 2500$ $[\frac{kg}{m^3}]$ is a good estimate. $\sigma_{m,g}$ is more difficult, but both Tang [5] and Schei et al. [4] give values between $0.5 - 1$ $[\frac{N}{m}]$. Using these values one gets $Mo \approx 10^{-15}$ which is considered low. This is expected for metal melts by Clift et al. [47] and Lobo and Kolbeinsen [29]. Using the parameters discussed until now, with 0.01m as the sauter bubble diameter, one can estimate that $Eo \approx 4$. Based

on equations 3.84 and 3.79, and confirmed by the ASTM standard [35], one can see that $d_s \leq d_e$. With equation 3.83 this becomes:

$$d_{SD} = d_e \left(\frac{d_e}{d_s}\right)^2, \qquad \frac{d_e}{d_s} \geq 1 \;\; \Rightarrow \;\; d_{SD} \geq d_e \tag{4.1}$$

This leads to a reactor diameter of at least $1.4 \cdot 10^{-1} m$, but due to the danger of slug flow it should be increased $> 2 \cdot 10^{-1} m$ [30]. To err on the side of safety the reactor diameter should be larger then the minimum value by a safety margin acceptable to the experimenter. Depending on the plug size and flow parameters it might not be a bad idea to build in the same scale as, used by Olsen et al. [41]. Due to a large *Re*, giving turbulent conditions, one must expect some degree of coalescence and should plan ones dimensions accordingly. More precise values for bubble sizes might be estimated from the pore size corrected for gas flow parameters and coalescence.
To get the desired bubble sizes the liquids properties are crucial. By matching Mo, Eo and *Re* through the gas velocity and the liquids parameters similarity should be attained. The gas properties are not important when the bubbles are rising in the flow, but if one also desires to measure the inlet bubble size the surface energy density of the gas and plug must match the real system. This is not considered here. Finding suitable liquids to replace $Si_l|_{T=1873K}$ is a challenge. Here some of its property ratios are listed with respect to the approximate values for pure water at 298K, at 1atm.

$$\frac{\rho_{Si_l}|_{T=1873K}}{\rho_{H_2O}|_{T=298K}} \approx 2.5 \tag{4.2}$$

$$\frac{\mu_{Si_l}|_{T=1873K}}{\mu_{H_2O}|_{T=298K}} \approx 0.6 \tag{4.3}$$

Approximate values are taken from Lobo and Kolbeinsen [29]. This author has not found any liquids possessing close to both of the values as listed in the equations above. It is easy to find one, but not the other, so matching the dimensionless numbers is crucial when deciding on how to vary the operational parameters and choosing fluids. A note of warning, some fluids might be poisonous, corrosive, pose other health hazards, or cause material damage. In this case the experiment should be modified to fit the system. This author is not responsible for any situations that may occur when doing this experiment. As a final note, something to remember is to consider changes in gas flow rate, and other flow parameters, if measured at high temperatures as they tend to change when brought down to ambient conditions. This is also true the other way around. While it is not condidered here it can be looked up in Olsen et al. [41], Engh [1], or Jakobsen [12].

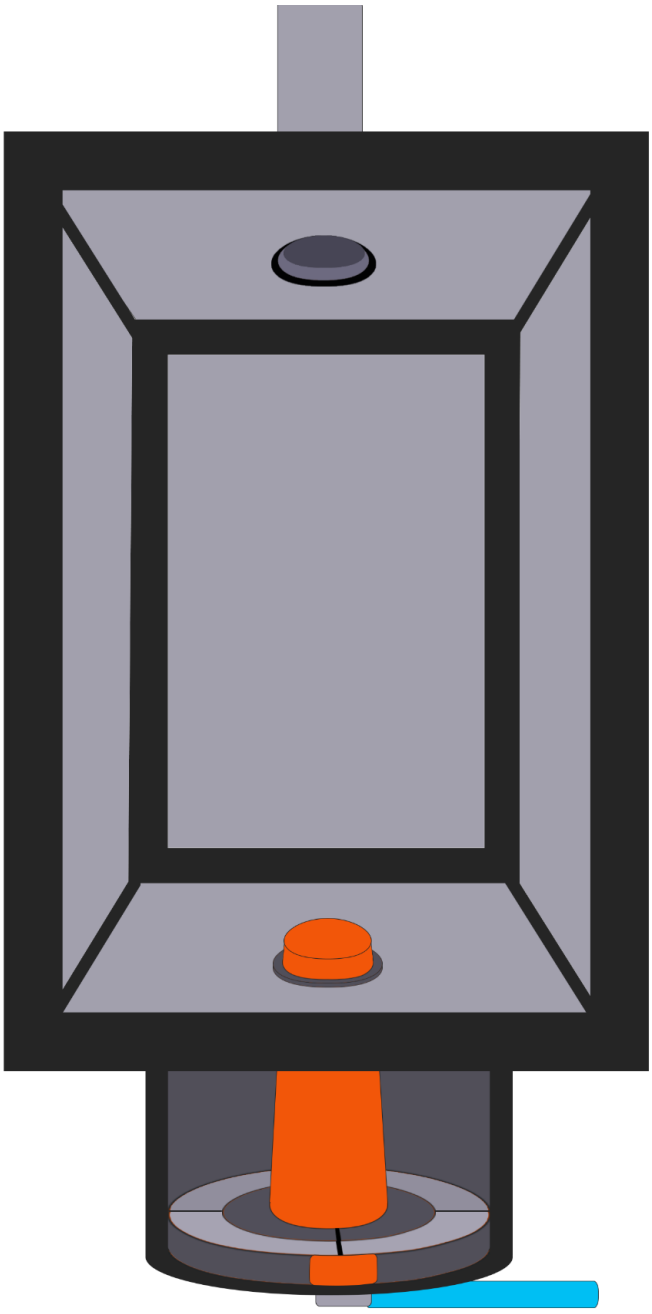

Figure 4.0.1: The reactor proposed by this work.

Chapter 5

Experiment

This chapter presents a description of the performed experiments. It starts with a description of the samples and their preparation continuing with the apparatus and experimental procedure. At the end some details and deviations are given.

5.1 Samples and Preparation

The silicon used in this experiment had a purity of at least 8N [19]. Initial master slags were made by Jakobsson at NTNU from commercial oxides with a purity of $\geq 99.5\%$ [19]. To get a homogeneous slag the oxides were mixed in different proportions, melted, quenched and crushed, with the last three steps repeated atleast two times [19]. The compositions of the master slags used in this experiment can be seen in table 5.1. Jakobsson notes that all the master slags contaied approximately $0.1 wt\%\ Fe_2O_3$, with

Table 5.1: Composition of master slags after normalization measured by XRF. From Jakobsson [19]

Slag	SiO_2 $[wt\%]$	CaO $[wt\%]$	Al_2O_3 $[wt\%]$	MgO $[wt\%]$
1	38.0	20.9	40.9	0.1
2	68.6	20.9	10.3	0.0
3	39.5	50.4	9.8	0.0

the total initial concentration of all other measured oxides $\geq\ 0.1 wt\%$ [19]. By mixing the master slags in table 5.1 with different proportions the desired slag compositions were obtained. These can be seen in table 5.2. To ensure homogeneity the new slag mixtures were heated to 1873K, kept there one hour, before quenched and crushed.

Table 5.2: Intended slag concentrations.

Slag ID	SiO_2 $[wt\%]$	CaO $[wt\%]$	Al_2O_3 $[wt\%]$
CSA255520	55	25	20
CSA254035	40	25	35
CSA404020	40	40	20

The three slag compositions in table 5.2 were chosen due to their representative concentration with respect to the slags generated during refining of different *Si* alloys. Figure 5.1.1 shows their location in the ternary phase diagram, where two and two concentrations lie along the iso-concentration lines for each of the respected species.

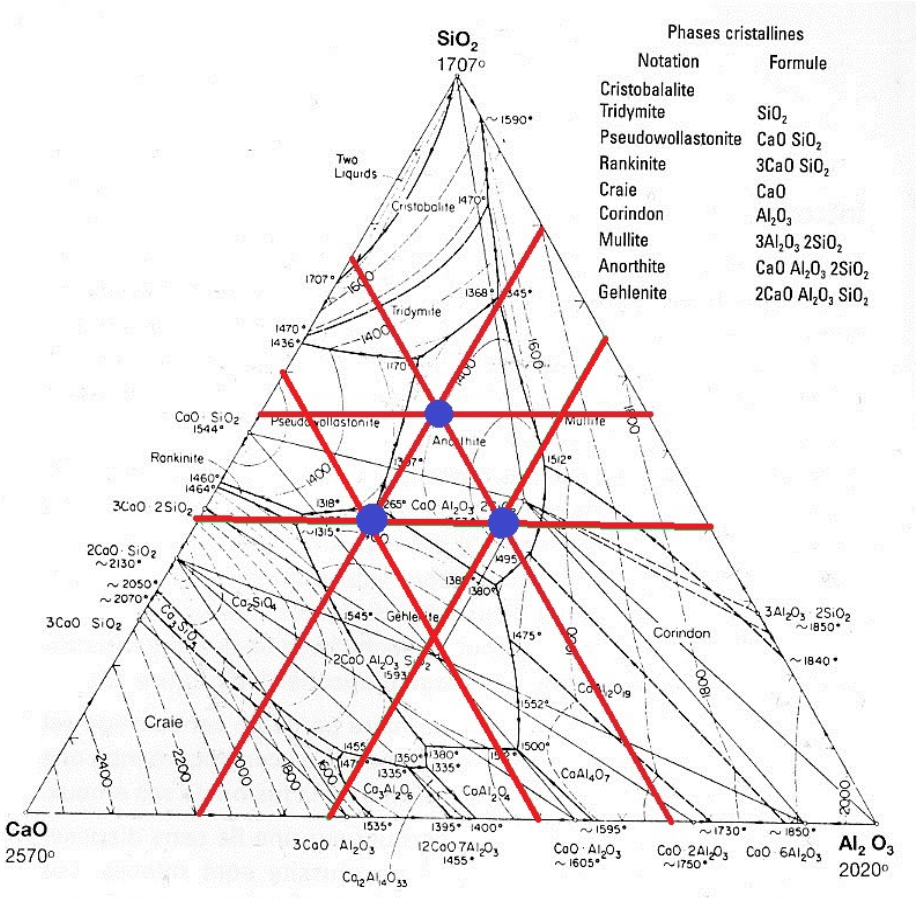

Figure 5.1.1: The slag compositions chosen. Phase diagram modified from Schei et al. [4]

5.2 The Furnace

The apparatus used during the experiment was the TF2 graphite tube furnace at NTNU, which is of an inhouse design. Figure 5.2.1 shows a picture of the furnace while figure 5.2.3 contains a more detailed description. By passing a current through the graphite resistance tube heat is generated allowing for operation temperatures up to 1973K. Graphite is well suited due to its high thermal shock resistance allowing for rapid thermal cycling. The furnace was kept under an argon atmosphere at 1.15-1.3 bar to ensure that neither the sample or the graphite was in contact with an oxidizing atmosphere in the hot zone. Using the gas inn and outlet valves the pressure is controlled manually by ensuring the gas flow rate is high enough to have constant gas cycling, while maintaining the desired pressure range. B-type thermocouples were used to control the temperature due to to their reliability at 1873K. From figure 5.2.3 it can be seen that two thermocouples are used. The one inserted from the top was used to regulate the temperature, while the second was used as an insurance. Much work was done to ensure a wide hot zone to get good measurements, and the temperature profile can be seen in figure 5.2.2.

This furnace was used due to its special crucible insertion and withdrawal system. First the crucible is put into a graphite crucible holder mounted on a rod. Fastened beneath the crucible holder is a cylindrical slab which seals the lower chamber as the holder itself enters. To ensure the seal is tight and the slab kept in place, a second seal is mounted to the first and fastened to the furnace itself. After the lower chamber is tightly sealed it is cut of from the outer atmosphere and evacuated. When the chamber is sufficiently evacuated its connection to the vacuum pump is closed off, and the chamber is subjected to the main chambers atmosphere by opening the equalizer valve, followed by opening the chamber separation mechanism. The crucible holder can now be raised into the main chambers hot zone by opening a lock bolt in the sealing slab. This must be done swiftly to ensure that as little gas escapes. When withdrawing the crucible the rod is quickly retracted as to place the crucible holder directly above chamber separation mechanism. The crucible is kept here for more then 5min allowing the rod to cool sufficiently as to not be hazardous to the operator. Quenching the sample is crucial to retain the high temperature distribution, and is seen to by a part of the cooling system placed close by. From this point one only has to lower the crucible holder further down, seal the main chamber and open the lower chamber to the outer atmosphere. By using this insertion and withdrawal contraption one can keep disturbances to the furnace atmosphere to a minimum, allowing for all the samples in one series to be subjected to as equal conditions as possible.

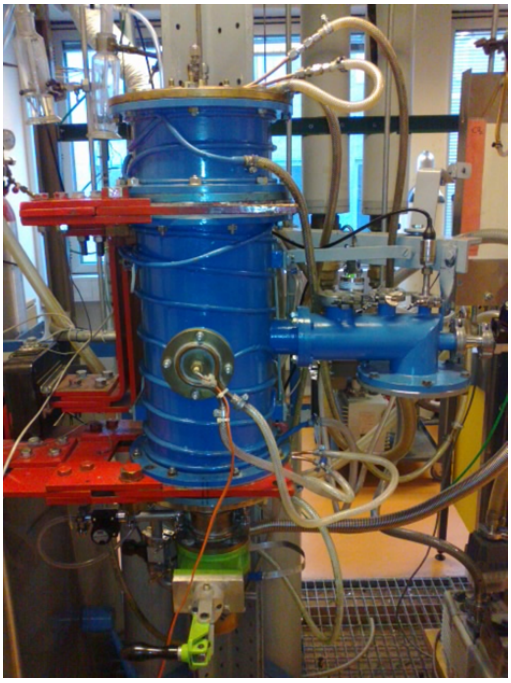

Figure 5.2.1: TF2 tube furnace

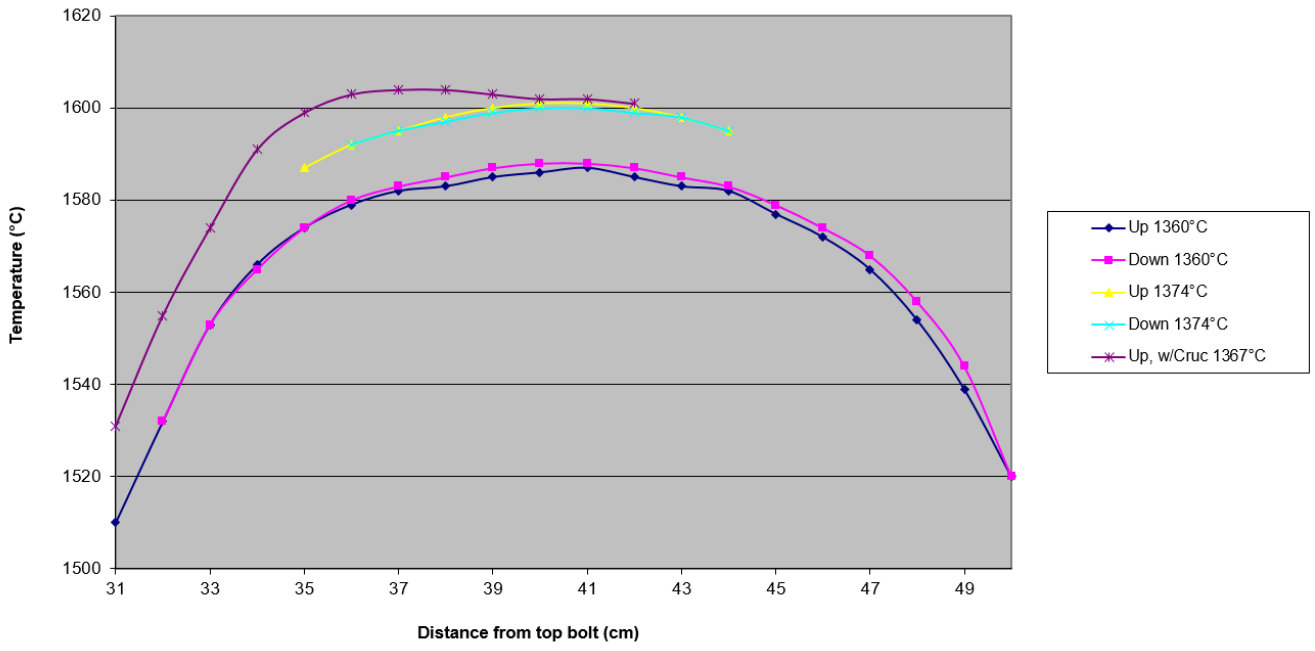

Figure 5.2.2: Temperature profile with and without a crucible. The temperature of the side thermocouple is also listed.

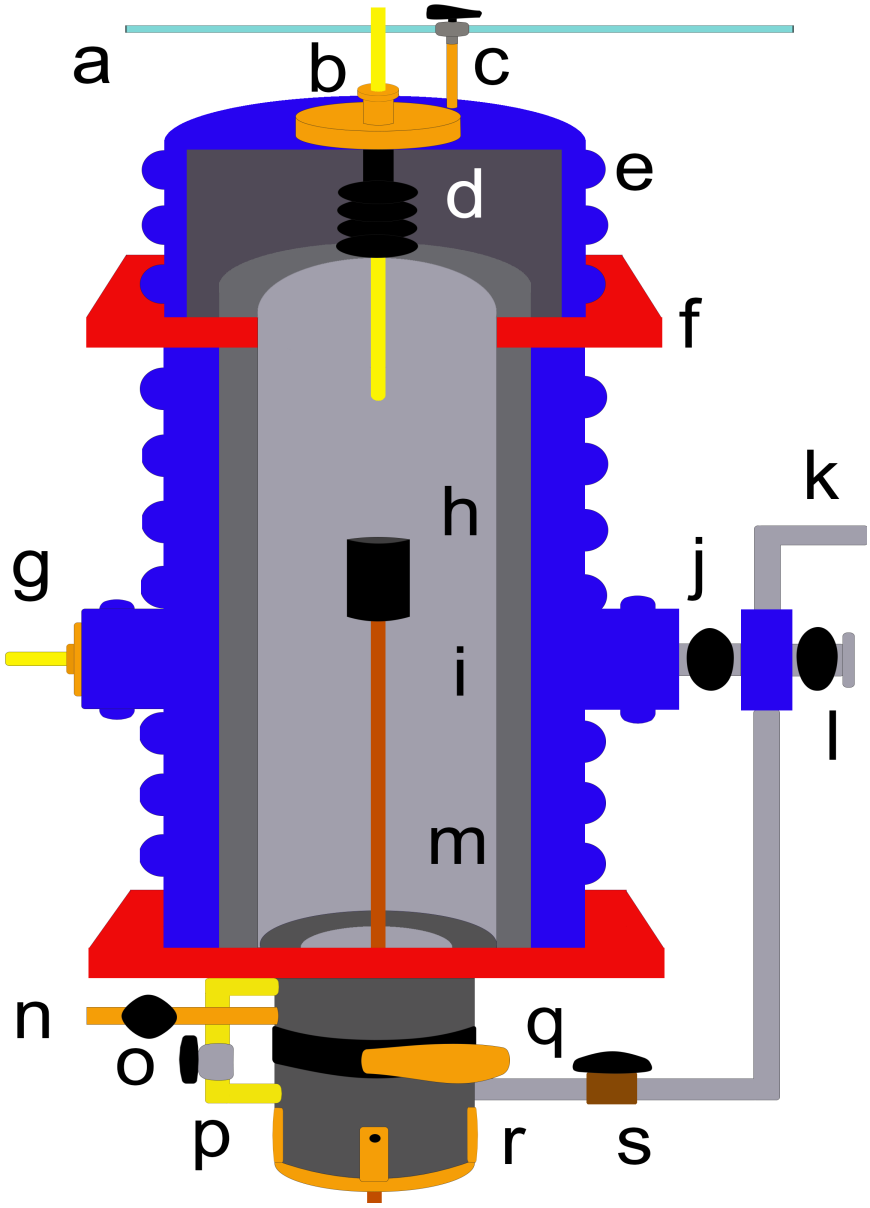

Figure 5.2.3: Illustration of the furnace

(a) Gas tubing from flask
(b) Primary thermocouple
(c) Gas inlet with valve
(d) Heat shield
(e) Water cooling tubes
(f) Transformer contacts
(g) Secondary thermocouple
(h) Crucible holder
(i) Resistance heating element
(j) Valve conecting main chamber to vacuum pump
(k) Vacuum pump pipe
(l) Valve connecting the tubing to the outside
(m) Crucible holder rod
(n) Gas outlet
(o) Gas outlet control valve
(p) Valve connecting the main and lower chamber
(q) Sealing mechanism
(r) Lower chamber crucible seal
(s) Valve connecting lower chamber to vacuum and the outside

5.3 Experimental Procedure

12g of silicon pellets were put into 15 IG-110 graphite crucibles with dimensions Ø30mm/22x45mm and an inner height of 40mm. A premelt of the silicon pellet was performed to minimize the inconsistencies in contact area between metal and slag. With figure 5.2.2 as a reference the inner bottom of the crucible was put at 42cm while the thermocouple tip was placed at 38cm. This gave a smoother surface morphology with a contact area approximately equal to the crucible opening. The furnace was evacuated to ≤ 0.3mbar and refilled with 5.0 argon. Heating to 1600°C was started after the internal furnace pressure reached 1.2bar, at a rate of $40\frac{K}{min}$. During the experiment the internal pressure was kept between 1.15-1.30bar. Each crucible was held in the hotzone for 7min before quenching. The holding time at the chamber separation mechanism was 5min for the first series, but was later increased to 7min due to the rods heat. 11g of slag was then added to each crucible, with compositions listed in table 5.2. Three different slags were used with five samples in each slag series, totaling 15 samples. Each series was subjected to the same procedure described above with exceptions in holding time. Five time steps were chosen and can be seen in table 5.3. The first four time steps measure the mass transfer kinetics, while the 180min sample was expected to reach equilibrium concentration as proposed by Jakobsson [19]. To keep the experimental conditions as constant as possible each slag series was run on the same day and kept in a desiccator after cooling to avoid contamination.

Table 5.3: Time steps used.

Time $[min]$	5	10	20	30	180

5.4 Sample Preparation for Analysis

Before analysis the graphite crucible was removed and the slag and metal separated. The graphite crucibles were lathe turned by a technician at the Faculty of Natural Sciences and Technology's graphite workshop at NTNU leaving a thin graphite layer. This final layer was in turn removed by a hand held rotary tool with diamond bits. Figure 5.4.1 shows one such sample after the crucible was removed. The metal and slag were then separated by hand using the power tool and pliers so the pure phases could be put into separate containers. All of these activities were performed inside a fume cupboard due to the amount of graphite dust generated, and the health hazard associated with inhaling this dust. Great care was taken to ensure that no metal was present in the slag samples and no slag in the metal samples. As to not contaminate the final product pieces were discarded rather than kept, if separation could not be attained in a reasonable time frame with the tools available. Over $95wt\%$ of the metal and atleast $60wt\%$ of the slag was kept after separation.

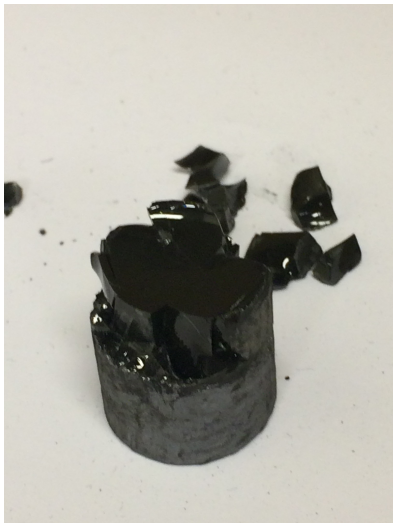

Figure 5.4.1: Slag and metal after the crucible was removed.

The metal was easily separated from the slag due to its strength, however the geometry of the metal surface after solidification resulted in some material loss.

Due to silicons volumetric expansion when solidifying a concave protrusion shaped like a paraboloid protruded from the metal surface into the slag. The protruding surface could be quite uneven with smaller protrusions extending from the main body. These small protrusions could be quite fragile thus separating from the main body when the slag was removed, and is expected to be the primary contribution to the metal loss. Any visible slag pieces clinging to the metal were ground away to give a clean metal surface. The slag was quite brittle crumbling into a mixture of varying particle sizes accompanied by a rough sand. There were a high prevalence of small metal inclusions in the slag, which were ground away if possible. Since the concentration of elements in the metal were quite different from the slag it was deemed necessary to err on the side of caution rather than to risk contamination. This led to some of the slag particles being discarded if the metal could not be removed. Together with the sand these are expected to constitute the primary loss of slag.

After separation the metal samples were crushed to a fine powder using a tungsten carbide disk mill. The crushing chamber was cleaned with high purity cleaning quartz and acetone before the metal samples were introduced, and with pressurized air between each sample. As for the slag samples they were crushed with a polytetrafluoroethylene ball mill. Before each series the ball and cup were cleaned by crushing high purity cleaning quartz, pressurized air and ethanol. Between each sample the ball and cup were cleaned with pressurized air. If there was still any visible powder in the cup it was removed with physical means and washed with ethanol. This was performed twice on each slag sample to get a powder fine enough for XRF. The slag n powder form can be seen in figure 5.4.2.

Figure 5.4.2: Slag in powder form after one round of crushing.

5.5 Analysis

Both metal and slag were analyzed by ICP-MS to find the concentration of $[Ca]$ and $[Al]$ and to check for contaminants in the slag. This was done by the HR-ICP-MS lab at the Department of Chemistry at NTNU, with the instrument type Element 2 from Thermo Electronics. Two sub-samples, between 25-45mg, were taken from each sample and dissolved in a 1.5mL ultra pure 68% HNO_3 + 0.5mL 40% HF mixture. After dissolution the samples are diluted, with deionized water, to a final volume between 216-220mL, giving 0.1M HNO_3 and 0.23% v/v HF. Three samples of NIST metallurgical silicon standard reference, three standard slag references and three blank samples were analyzed together with the sub samples to calibrate the machine.

5.6 Considerations

There were some complications concerning the 180min sample for CSA404020. After operating for one hour small flakes of the thermocouples Al_2O_3 insulation fell into the sample. When this happened the thermocouple stopped responding and the furnace was rapidly cooled. After inspecting the sample, removing the available surface contaminants and weighing it, it was decided that the sample could still be used since the amount of contaminants added in the system were less then $0.05g$, and was considered

too low to make an impact. The slag was then reheated four days later for 180min. Since this was the equilibrium sample, and the only important factor should be to keep it at the given temperature until equilibrium is reached it was decided that this would not affect the final result. When the slag and metal was separated one could still see the particles at the top of the slag. The slag around this area was discarded along with the particles.

When dissolving silicon metal in HNO_3 + HF for ICP-MS the mixture will generate some heat. This is due to reactions taking place between Si, Ca and F. NIST proposes using the property data from Chase [59] for CaF_2 and Lyman and Noda [60] for SiF_4. From these data one can see that SiF_4 is more volatile then CaF_2. Jakobsson [19] had an equal problem with Si and B reacting with F and he found that the Si loss was not significant as to compromise the analysis.

Chapter 6

Results

The experimental results from ICP-MS can be seen in table 6.1. There were no other contaminants found

Table 6.1: Experimental results for $[Al]$ and $[Ca]$ by ICP-MS. The ppm values are averaged over the two sub-samples and the standard deviations for the samples are included.

Sample	$[ppm\ Al]_{avg}$	$STD_{[Al]}$	$[ppm\ Ca]_{avg}$	$STD_{[Ca]}$
CSA404020-Si5	915.27	53.12	1523.79	133.72
CSA404020-Si10	3053.05	152.29	5270.03	158.44
CSA404020-Si20	2898.99	215.11	5412.82	399.11
CSA404020-Si30	5269.32	117.82	9669.25	375.29
CSA404020-Si180	8400.26	1877.78	17339.76	4282.17
CSA255520-Si5	3044.34	314.40	4670.04	410.70
CSA255520-Si10	1431.92	90.82	2112.08	119.97
CSA255520-Si20	1868.20	160.73	2703.56	275.84
CSA255520-Si30	2151.57	193.65	3059.73	277.15
CSA255520-Si180	3212.46	122.34	3970.30	90.85
CSA254035-Si5	5465.27	341.85	4308.90	184.04
CSA254035-Si10	4213.50	188.93	1756.62	75.07
CSA254035-Si20	7558.93	86.32	4572.67	122.96
CSA254035-Si30	5438.90	987.79	2199.34	372
CSA254035-Si180	9814.48	929.67	4660.35	151.28

in any of the slag samples beyond what was already shown in figure 5.1. The measured values for each sub-sample by ICP-MS are average values from the detector and are delivered with their own relative standard deviation(RSD). Due to this inherent uncertainty the STD values in table 6.1 are calculated by taking the root of the sum of the variance between sub-samples and the average between the sub-samples own variance. This is expressed in equation 6.1, where the sub-expressions are from the ASTM standard for basic statistics [61].

$$STD = \left[\frac{n\left(\sum_{i=1}^{n} x_i^2\right) - \left(\sum_{i=1}^{n} x_i\right)^2}{n(n-1)} + \frac{\sum_{j=1}^{n} \left(\frac{x_j RSD_j}{100}\right)^2}{n} \right]^{\frac{1}{2}} \tag{6.1}$$

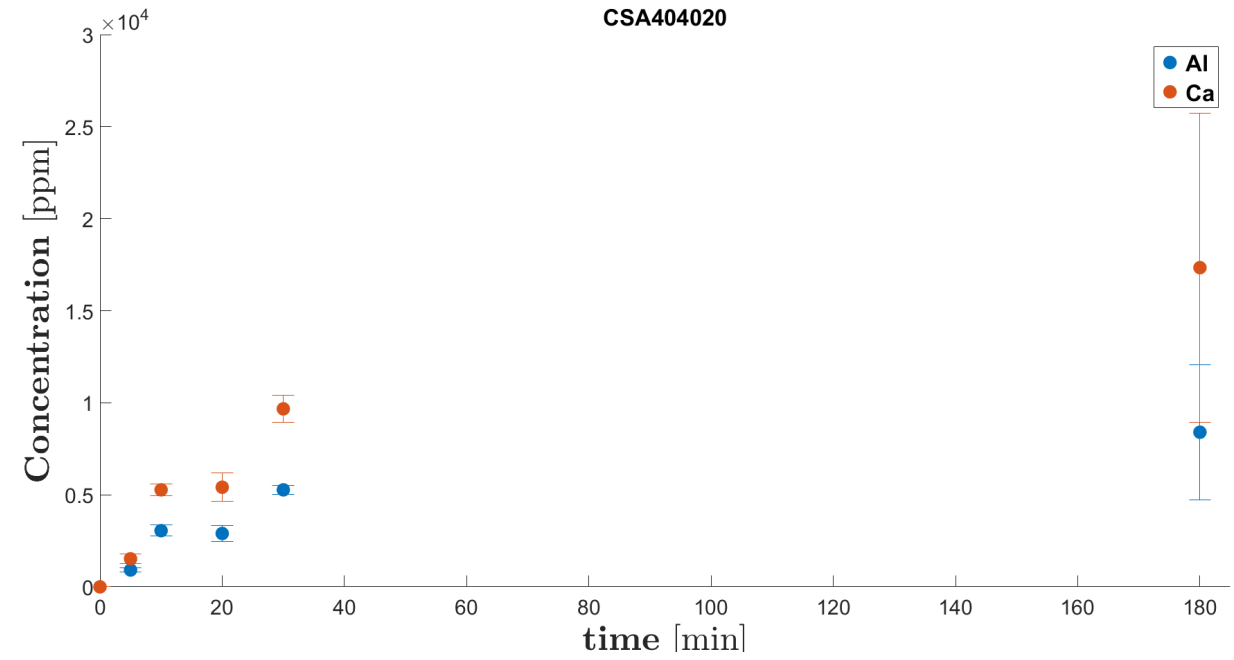

Figure 6.0.1: CSA404020 sample with errorbars set at 95% confidence level.

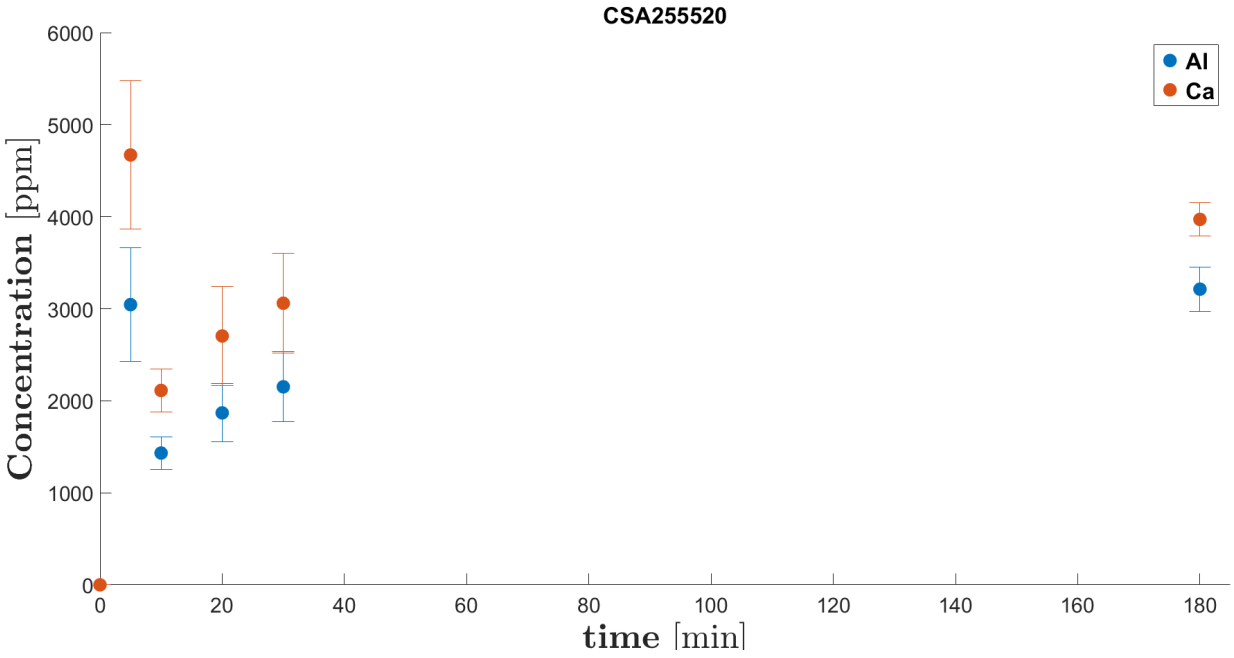

Figure 6.0.2: CSA255520 sample with errorbars set at 95% confidence level.

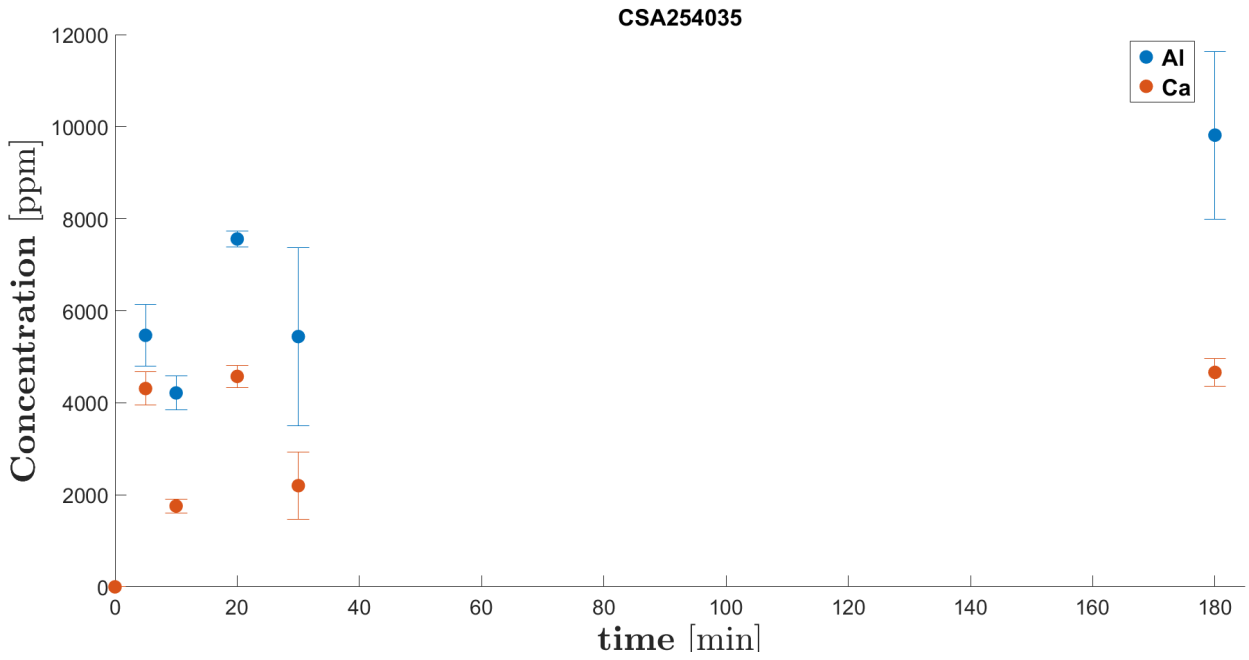

Figure 6.0.3: CSA254035 sample with errorbars set at 95% confidence level.

6.1 Calculating $k_{i,t}$

Due to the large deviation seen in the experimental data from the models using $k_{i,t}$ this author was not able to generate a a useful value. This will be discussed in later.

Chapter 7

Industrial Samples

The samples were taken at Elkem Salten, as part of the KPN FUME project, in 2012 and 2014, for a 96% *Si* and 99% *Si* alloy respectively. These samples are not extracted, or prepared, by this author and are printed with permission from Elkem. Figures 7.0.1- 7.0.4 show the normalized concentrations of both setts with respect of $[Al]$ and $[Ca]$. Only the normalized concentrations are shown as per Elkem's wishes. The normalization was done with respect to the initial concentration for each element in each ladle. Samples were taken from the tapping jet into the ladle and when the ladle was 50%, 75% and 100% full. Different ladles were added different amounts of fluxing, or cooling materials, at different times, but this author is not eligible to share this information. This together with some assumed variations in expected slag concentrations are expected to be the cause of deviations between the individual ladles for an alloy. Since this author only has ICP-MS data from this project, the compositions of the slags could not be determined. This is due to a limitation of ICP-MS, as it is only reliable at finding the concentrations of trace elements. The 2012 samples also contain an analysis of the product after it was tapped from the ladle. These samples were analyzed by ICP-MS, and as far as this author has been informed, underwent the same sample preparation process for ICP-MS as the experiments done in this thesis. While this set contains data where the

Some work has already been done using these sample setts. Kero et al. [3] has reviewed the refining kinetics of multiple elements from the 96% *Si* alloy(2012), covering a broad range of other elements if the reader is interested.

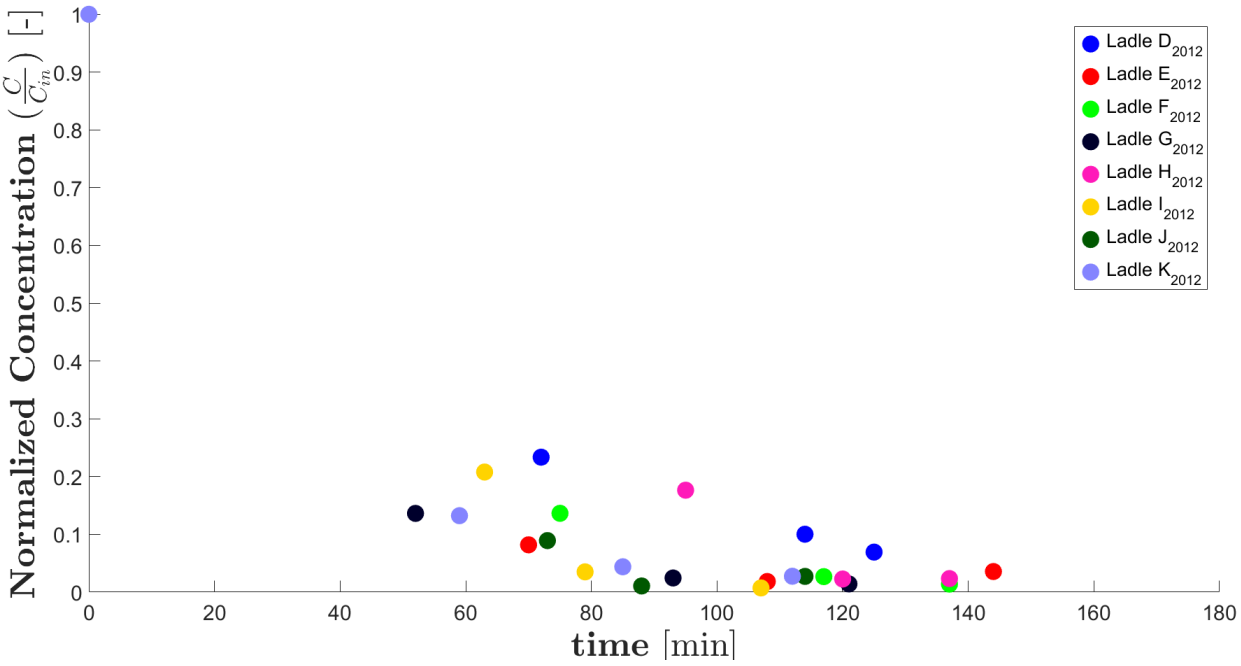

Figure 7.0.1: Normalized [*Ca*] of 96% *Si* from Elkem Salten. Printed with permission from Elkem.

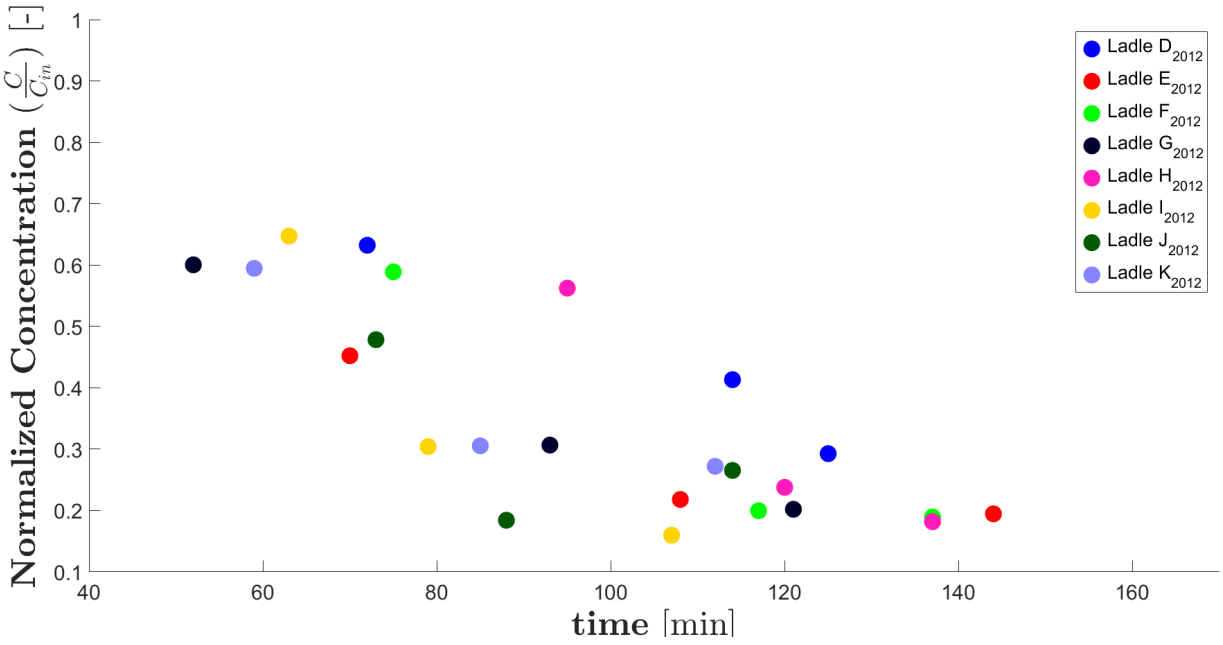

Figure 7.0.2: Normalized [*Al*] of 96% *Si* from Elkem Salten. Printed with permission from Elkem.

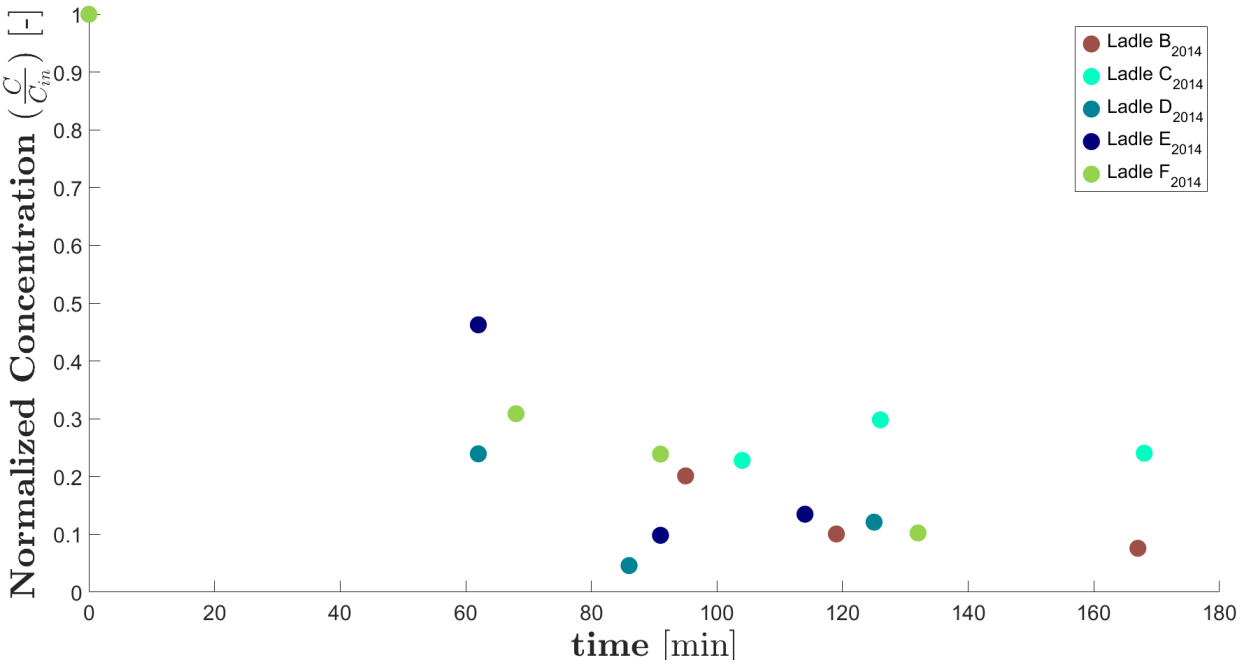

Figure 7.0.3: Normalized [*Ca*] of 99% *Si* from Elkem Salten. Printed with permission from Elkem.

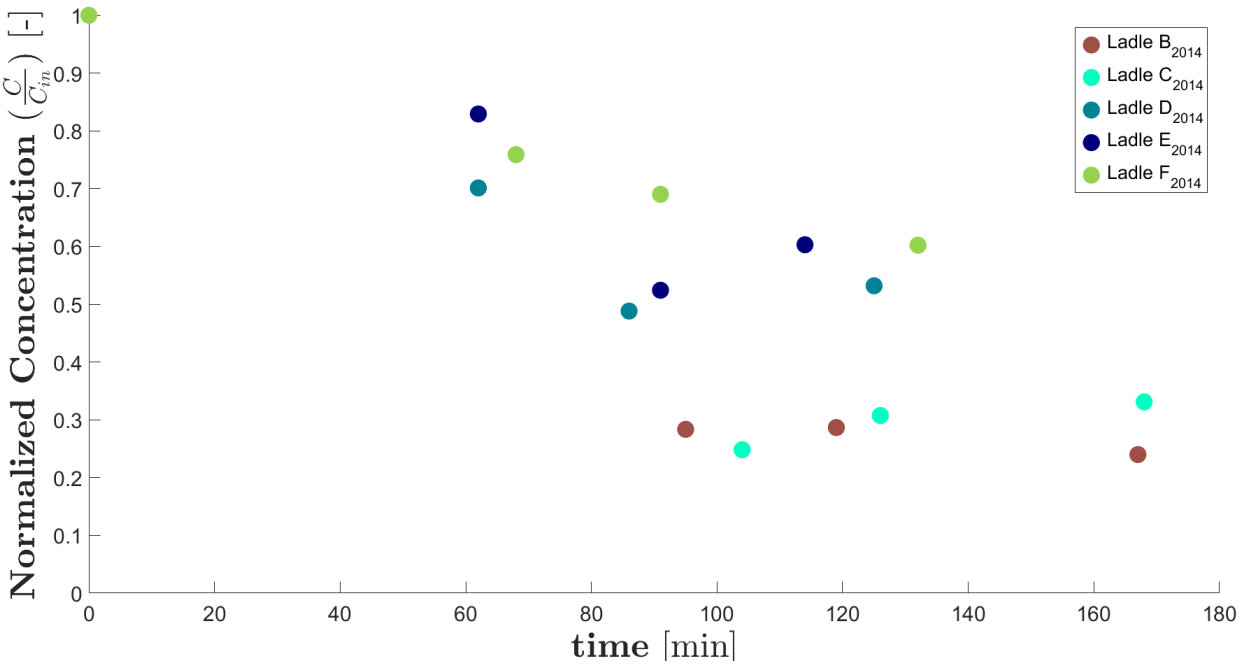

Figure 7.0.4: Normalized [*Al*] of 99% *Si* from Elkem Salten. Printed with permission from Elkem.

Chapter 8

Discussion

8.1 Mass Transfer Experiment

8.1.1 Samples

When the experimental results from table 6.1 are compared to the iso-concentration values for molten silicon in equilibrium with $SiO_2 - CaO - Al_2O_3$ slags, tables 8.1 and 8.2, one can see that they differ drastically. The experimental values are consistently exceptionally large compared to the literature. When compared to other authors doing similar, like Jakobsson [19], they do not fit either. Since the deviation is consistent and no value compares even remotely to the literature they are considered to be wrong. To catch the culprit an examination of the process steps is in order.
From figures 6.0.1, 6.0.2 and 6.0.3 it can be seen that while there are some sub-sample pairs which exhibit high degree of variance, the sample setts as a whole there looks to be a high degree of homogeneity between the two sub-samples. This excludes a consistent non-representative sampling of the final product as the culprit for this deviation. The deviation could come from not retrieving enough of the phase in question when separating metal and slag. This might be a reasonable train of thought if the problem lie in the slag, but not for the metal. As already mentioned there was little trouble extracting the metal due to its tendency to stay as one piece, giving little metal loss. Another step that might affect the samples could be contamination by the slag when crushing. This does not hold water since the metal and slag were crushed by two different machines.
Operational factors concerning the procedure or the materials used are next in line. The procedure and materials have been tried and tested previously by Jakobsson [19], giving reliable results. While a different furnace was used, by Jakobsson, it is not seen as likely for the culprit to lie there.
Next it would be logical to question the analysis method. ICP-MS is a common method to employ when looking for trace elements in metals and slags. If this was the case then onw should see such deviations in other works as well. As fortune has it there were some Fe65Si samples sent along, in addition to the experimental samples presented here, as part of the same analysis order. These were analyzed the same day making it reasonable to assume that the operational conditions were close to equal. The owner of these samples was contacted and revealed that the data he had received followed the expected behavior for the analyzed elements. While these were not $[Ca]$ and $[Al]$ this could shine some light on the problem. Fe65Si uses a different standard metal sample when calibrating, so it might be the case that the silicon metal standard sample had been contaminated. If this is the case then all the sample data should deviate by a consistent amount and could still be of some use, as they will show the same trends even if the values are off. This is assumed moving forward as it is considered to be the most likely occurrence, due to the consistent deviation, and how the experimental data shows some of the same behaviors seen in the

industrial data.

Table 8.1: $[ppm\ Al]$ values from various authors in equilibrium with $SiO_2 - CaO - Al_2O_3$. Values from Schei et al. [4] and Wang et al. [25].

Sample	CSA404020	CSA255520	CSA254035
$[ppm\ Al]^{1550^\circ C}_{Schei}$	2650	800	4250
$[ppm\ Al]^{1550^\circ C}_{Wang}$	2500	1500	5250

Table 8.2: $[ppm\ Ca]$ values from various authors in equilibrium with $SiO_2 - CaO - Al_2O_3$. Values from Schei et al. [4] and Wang et al. [25].

Sample	CSA404020	CSA255520	CSA254035
$[ppm\ Ca]^{1550^\circ C}_{Schei}$	5500	$\geq$400	400
$[ppm\ Ca]^{1550^\circ C}_{Wang}$	2600	525	1000

8.1.2 Mass Transfer Rates

When comparing the industrial data, figure 7.0.1-7.0.4, and experimental data, figures 6.0.1-6.0.3, one can find certain trends. A consistent trend in both the experimental and industrial data is that the mass transfer rate is larger in the samples with lower initial concentration gradients of $[Al]$ and $[Ca]$. If $(\omega_{[i]} - \omega^{eq}_{[i]})|_{m\to s}$ is the primary driving force then $\frac{d\omega^{99\%}_{[i]}}{dt} > \frac{d\omega^{96\%}_{[i]}}{dt}$ should be the case. This tendency is also seen in the experimental data were CSA255520, which has the lowest equilibrium $[ppm\ Al]$ and $[ppm\ Ca]$, has the highest $\frac{\omega_{[i]}|_{t=5min}}{\omega_{[i]}|_{t=180min}}$ ratio.
Table 8.3 shows the viscosity of different slags, calculated using Kontratiev and Jak's [11] model. In the experimental data one can see a trend where the sample with the most viscous slag, CSA255520, exhibiting the highest initial mass transfer rate. Consequently the sample with the least viscous slag, CSA404020, exhibits the lowest initial mass transfer rate.

Seen in isolation the behavior of $[Ca]$ in both industrial alloys seem to be in accordance with Engh's [1] model. This is in the degree that they seem to follow a relationship, $f(t) = Ae^{-Bt}$, where A and B are constants. This is not true for $[Ca]$ in the experimental data, where $[Ca]$ closely follows the same tends as $[Al]$ in every slag. $[Al]$, in the 96% alloy, exhibits the closest degree of expected behavior in accordance with Engh's model, together with the experimental sett CSA404020, relative to the other $[Al]$ setts. On the other hand, $[Al]$ in the 99% alloy and experimental data seem to exhibit a more complex behavior. These deviations from Engh's [1] model show some interesting aspects and symmetries, and are discussed separately in the oscillations section.

This author has not found anything in the literature which can explain the consistent trends found for the mass transfer rate with respect to the slag viscosity, and initial concentration gradients. The trivial solution to these deviations would be that the samples got switched somehow in the process. While it might be tempting it is not viewed as likely by this author, as the samples were meticulously labeled the whole way. Special care was also taken, for fear that it might happen, to only work with one sample set at any given time. While this would give some explanation to the deviation in experimental values it would not explain the deviations observed in the industrial data.

Table 8.3: Viscosity of the slags used in the experiments. Calculated using the model from Kondratiev and Jak [11]

Sample	CSA404020	CSA255520	CSA254035
μ_s $[Pa\ s]$	0.4135	4.0363	1.5086

While looking for possible explanations to the mass transfer rate deviation, the characteristics an effect, or combination of effects, must exhibit was considered. It must be kinetic in nature as it does not hinder the mass transfer permanently. If this was the not the case then the equilibrium concentrations between silicon and slag would reflect this. It must be strong enough to dominate, or modify, the concentration gradient and the viscous forces. One of the things considered here was that the activities of $[Al]$, $[Ca]$, (SiO_2), (CaO) or (Al_2O_3) might change drastically with minute concentration variations. It is true that from the work done by Rein and Chipman [20], and the overview presented by Jakobsson [19], that the activities of these species does change drastically, with respect to different concentrations within the $SiO_2 - CaO - Al_2O_3$ system. The only caveat is that when looking at figures 3.2.3 and 3.2.4, the changes in these activities are still small at minute concentration variations. It also does not follow the industrial data where the higher concentration of $[Fe]$ in the 96% alloy should, according to Schei et al. [4] give lower activity coefficients for both $[Ca]$ and $[Al]$. There might be some other factor which increases this that has not been found by this author, as changing activities can be a powerful driving force explaining why the initial mass transfer rate is higher in the 96%, rather than 99% alloy.

When looking at the diffusion coefficient both Tang [5] and Liang et al. [17] agree, and have experimental data confirming, that the diffusion coefficient is reverse proportional with the viscosity. The theory presented on the subject from Schei et al. [4], Engh [1] and Waseda and Toguri [7] support this.
Turkdogan [10] may have an answer as he writes that if the cat or anion in a slag has a greater mobility then the local electrostatic potential will also retard the flux. Since the diffusivity of the oxygen-anion is larger then all the other species in the slag, as seen from Tang [5] and Waseda and Toguri [7], then this might have some effect on the concentration profiles. If a low viscosity allows for a rapid mass transfer, but this again causes local electrostatic potential gradients then this might supply the effect needed. Not enough data could be found by this author on the subject to confirm, or deny, this though.
A difference between the slags might be due to that the Al-ion changes its coordination as $\frac{(mol\%CaO)}{(mol\%Al_2O_3)}$ is beneath or above 1, as expressed by Waseda and Toguri [7] based on research from Kozakevitch [8, As read in [7]]. This can modify how the Al-ion is placed in the slag structure, which might also affect how the Ca-ion behaves. When this is tested against the slag concentrations it does not seem to hold water as CSA254035 is the only sample where $\frac{(mol\%CaO)}{(mol\%Al_2O_3)} < 1$.
There might be some unknown effect causing these deviations, but there is not presently enough data to run any complex statistical fitting for more complex expressions.

8.1.3 Oscillations

When the experimental and industrial data are compared there seems to be some sample setts that exhibit an interesting and consistent oscillating behavior. Before this is explored further it must be stressed that while this might be interesting there is presently not enough evidence to draw any conclusions. These oscillations may just be the bi-product of experimental uncertainty, or random noise which just happens to fit. The rest of the discussion on these oscillations will continue as if they present a physical effect, but this cannot presently be confirmed.

The reason this is brought up is due to its interesting implications concerning the predicament with the experimental data which will not fit any current models. This oscillation behavior i best seen for $[Al]$ in figures 8.1.1- 8.1.3 where lines have been drawn between the sample points for all the $[Al]$ samples. While this is also seen in the experimental $[Ca]$ samples it is not easily found in the industrial data so $[Ca]$ will not be shown this way.
Lets assume three reactions in a system with transport from a slag to pure metal:

1. $3[Si] + 2(Al_2O_3) = 4[Al] + 3(SiO_2)$
2. $2(CaO) + [Si] = 2[Ca] + (SiO_2)$
3. $3[Ca] + (Al_2O_3) = 3(CaO) + 2[Al]$

When the process starts reaction 1). and 2). start instantly, rapidly transporting Al and Ca atoms into the melt. Since the initial concentration gradient is large the initial flux will be high. When the Ca and Al atoms enter the metal they will rapidly diffuse through the volume due to internal concentration gradients and high temperature. Reaction 3). cannot start before an imbalance between $[Ca]$ and $[Al]$ happens. Since the concentration gradient concerning reaction 3). is low initially, with few of the $[Al]$ and $[Ca]$ atoms staying at the slag/metal interface, it will start to lag behind. If one imagines that when a flow of atoms from phase A to phase B fist has started, then it requires some time to turn the other way. In this case, if reaction 3). finds that there is too high a concentration of Al in the metal, then it takes it some time to reverse that flow to achieve balance. But when this flow is first brought around it takes some time to stop again. This would allow for a system where the concentrations of $[Al]$ and $[Ca]$ are constantly being adjusted. If one also assumes that the smaller the concentration gradient, then the easier it is for 3). to adjust the concentrations, then one can expect the concentration curves to exhibit some behaviors similar to forced dampened harmonic motion. One could also say that the general path the net flux would follow was something akin to Engh's [1] model. If one superimposes this behaviour on Engh's [1] model then one should expect something which looks like figure 8.1.3. As a final note it could also be theorized that the more viscous the slag was the more difficult it would be to turn the flow around.

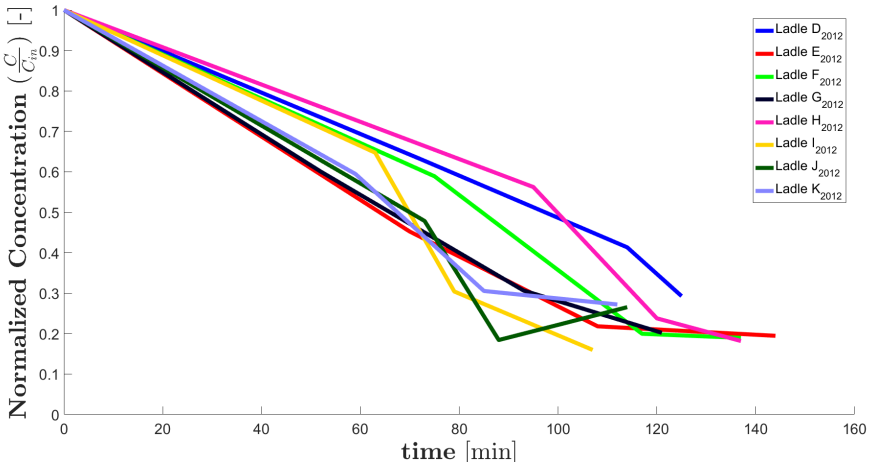

Figure 8.1.1: Industrial data for $[Al]$, in the 96% *Si* alloy. Normalized with respect to the initial concentration of $[Al]$ for each ladle in the set.

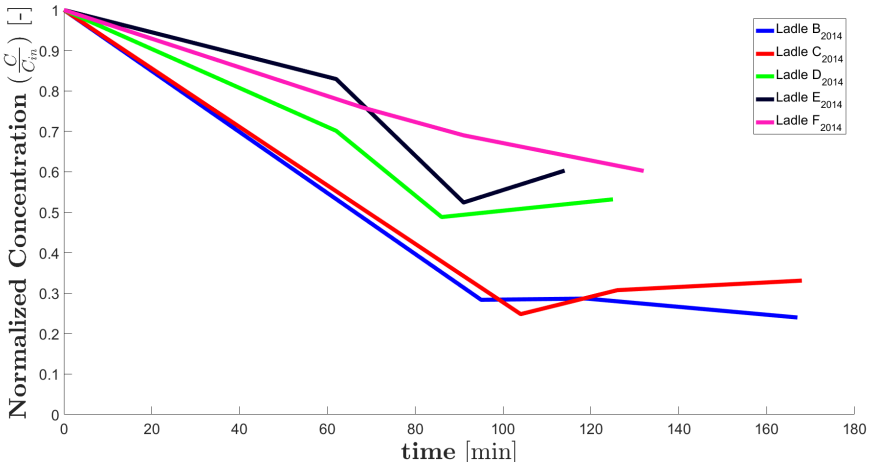

Figure 8.1.2: Industrial data for $[Al]$, in the 99% *Si* alloy. Normalized with respect to the initial concentration of $[Al]$ for each ladle in the set.

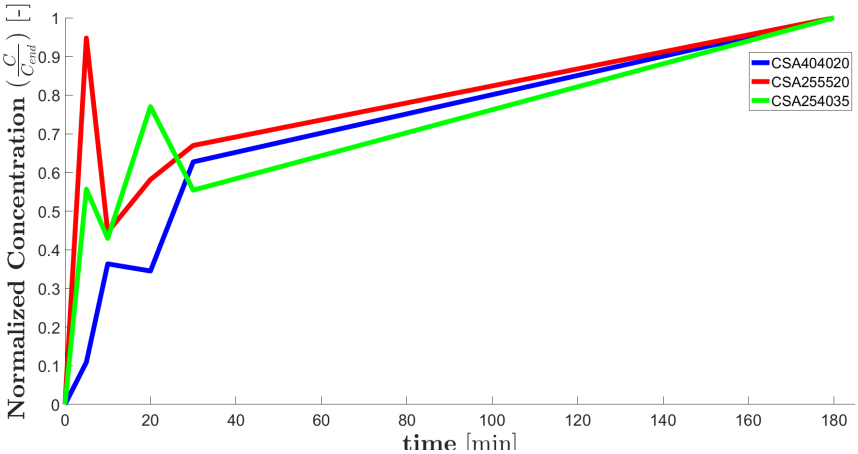

Figure 8.1.3: Experimental data for $[Al]$ for all tree slags. Normalized with respect to the 180min sample $[Al]$ for each slag.

While the discussion until now has focused on the physical aspects of such an effect there is a bit more too it. This was fist conceived by trying to find solutions to an in-homogeneous second order ordinary differential equation using Engh's model as the homogeneous solution, $\omega_{[i]}^{hom} = (1 - exp(-\varphi t))$, where $\varphi = \frac{k_{i,t}\bar{\rho}_s A_s}{m_m}\left(\frac{K_i f_{[i]}}{\gamma_{(i)}} + \frac{m_m}{m_s}\right)$, to better fit the experimental data. The math behind this sort of analysis, and how these solutions were found and the symmetries they posses will not be explained here. What can be noted is that if one uses the solution:

$$\omega_{[i]}(t) = \omega_{[i]}^{max}(1 - exp(-\varphi t)) + Aexp(-\zeta\phi_0 t)\, sin\left(\sqrt{1-\zeta^2}\phi_0 t + \varepsilon\right) \tag{8.1}$$

For the in-homogeneous second order ordinary differential equation, which has a forcing term akin to that found in forced damped harmonic motion then one gets the the graphs shown in figures 8.1.4 and 8.1.5. These solutions were generated by hand since not enough data was available to use a statistical fitting algorithm for equations on this form. Due to the time consuming nature of this work this author was not able to generate one for CSA254035. Figures 8.1.4 and 8.1.5 were generated as a proof of concept, and were not fitted perfectly due to time constraints. Their equations are shown here, normalized with respect to the 180min sample for each sample:

$$\omega_{[Al]}^{CSA404020}(t) = (1 - exp(-0.034t)) + 0.22sin(0.24t)\, exp(-0.04t); \tag{8.2}$$

$$\omega_{[Al]}^{CSA255520}(t) = (1 - exp(-0.04t)) + 3.54sin(0.195t)\, exp(-0.3t); \tag{8.3}$$

While these solutions are interesting prospects it is difficult to provide any more information without resorting into complex mathematics beyond the scope of this thesis, when it is not known if this is a real effect.

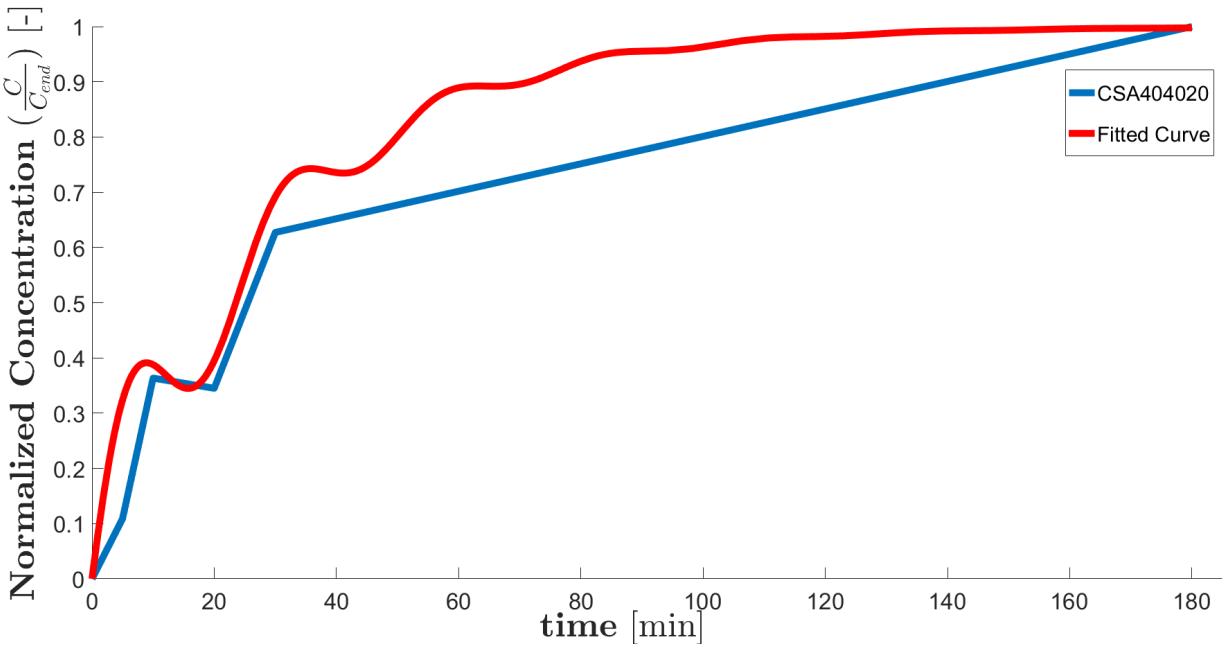

Figure 8.1.4: Experimental data for $[Al]$ in CSA404020, including a model where Engh's [1] model has been added forced damped harmonics. Normalized with respect to the 180min sample $[Al]$.

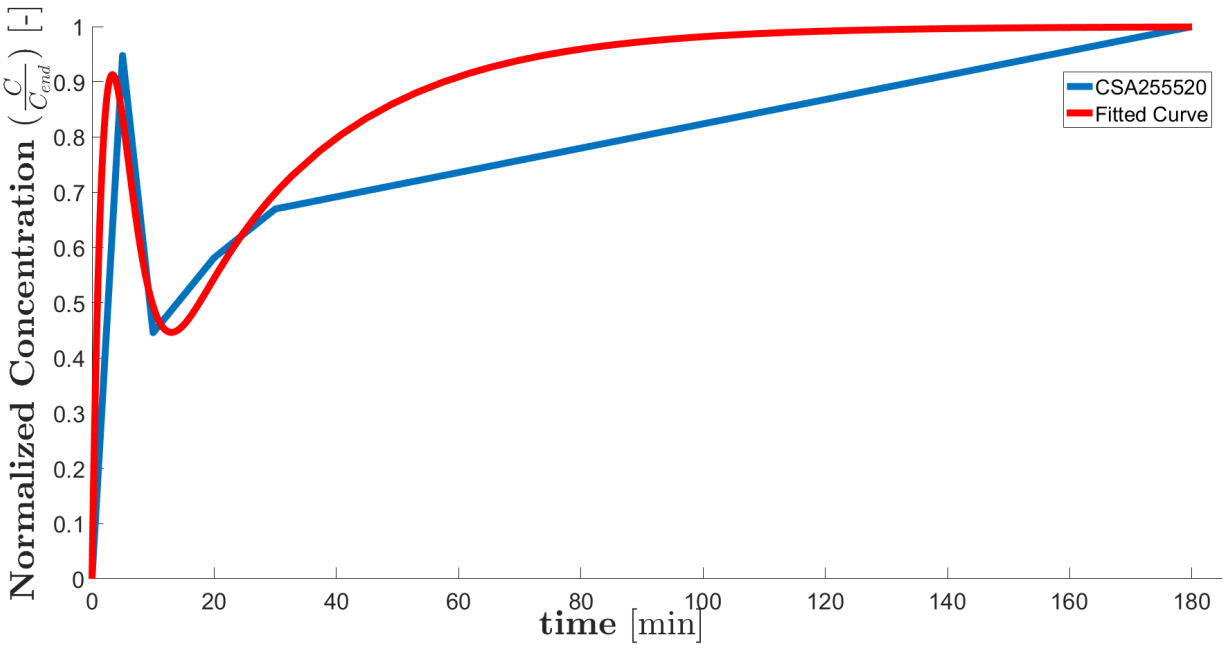

Figure 8.1.5: Experimental data for $[Al]$ in CSA255520, including a model where Engh's [1] model has been added forced damped harmonics. Normalized with respect to the 180min sample $[Al]$.

Chapter 9

Conclusions and Future Work

9.1 Conclusions

An experiment for measuring the sizes of gas bubbles in industrial ladles has been proposed. By creating a cold model with the same dimensionless parameters as the industrial ladle similarity should be attained. Due to the large discrepancy between the experimental concentrations of $[Ca]$ and $[Al]$ with the equilibrium concentrations from literature it is assumed that the experimental values are wrong. It is however thought that this is due to a contaminated standard sample so the deviation in all samples should be consistent. The industrial data for $[Ca]$ followed Engh's [1] model quite well if viewed individually. $[Ca]$ in the experimental data did not behave as its industrial counterparts, but instead exhibited the same behavior as $[Al]$ in the same system. $[Al]$ in the industrial 96% alloy was the $[Al]$ which behaved closes to what was expected from Engh's model. Both the industrial 99% alloy and the experimental data exhibited some of the same characteristics, with a few of the 96% alloy ladles following suite. When viewed as a whole a consistent trend was seen in both the experimental and industrial data. The rate of mass transfer increased when the concentration gradient decreased. This goes against the current theory and models on the subject. In the experimental data it was also observed that the rate of mass transfer was highest in the sample with the highest viscosity, and lowest in the one with lowest viscosity. This does not either fit any of the currently known theory on the subject. On the basis of this no mass transfer coefficient could be calculated for the experimental data, since the curves did not fit into any model where it can be calculated. In the discussion some interesting possibilities were discussed to explain this phenomenon, but much more work needs to be done before one can say that this is a real effect. All in all it must be concluded that the amount of data on this topic is not sufficient to explain what is observed and that more work must be conducted before any mechanism can be formulated reliably.

9.2 Future Work

This author will continue the work with PHD at NTNU. The cold reactor experiment will be conducted with the help of Elkem, and further plans are already in motion for an extensive analysis of the mass transfer.

Bibliography

[1] T.Abel Engh. *Principles of Metal Refining*. Oxford University Press, 2 edition, 1992.

[2] Erlend Lunnan Bjørnstad. *TMT4500-Materials Technology, Specialization Project, Review of the Parameters Needed for CFD Modelling of the Central Bubble Column in Oxidative Ladle Refining of Silicon*. Thesis, NTNU, 2015.

[3] Ida Kero, Mari K. Næss, Vegar Andersen, and Gabriella M. Tranell. Refining kinetics of selected elements in the industrial silicon process. *Metallurgical and Materials Transactions B*, 46(3):1186, 2015.

[4] Anders Schei, Johan Kristian Tauset, and Halvard Tveit. *Production of High Silicon Alloys*. TAPIR FORLAG, Trondheim, 1 edition, 1998.

[5] Kai Tang. Thermodynamic analysis of oxidative ladle refining of silicon melt including models for thermophysical properties of the silicon melt and sio2-al2o3-cao slag. Technical report, SINTEF Materials and Chemistry, 2007.

[6] Ahindra Ghosh. *Secondary Steelmaking*. Principles and Applications. CRC Press LLC, 2000 N.W. Corporate Blvd., Boca Raton, Florida 33431., 1st ed. edition, 2000.

[7] Yoshio Waseda and James M Toguri. *The Structure and Properties of Oxide Melts*. World Scientific Publishing Co. Pte. Ltd., 1 edition, 1998.

[8] P Kozakevitch. Viscosite et elements structuraux des aluminosilicates fondus: laitiers cao-al2o3-sio2 entre 1600 et 2100 c. *REVUE DE METALLURGIE-CAHIERS D INFORMATIONS TECHNIQUES*, 57:149–160, 1960.

[9] Gabriella Tranell. Si summerschool, slag refining, 2014.

[10] E. T. Turkdogan. *Physiopchemical Properties of Slags and Glasses*. The Metals Socity, London, 1983.

[11] Alex Kondratiev and Evgueni Jak. A quasi-chemical viscosity model for fully liquid slags in the al2o3-cao-feo-sio2 system. *Metallurgical and Materials Transactions B*, 36(5):623–638, 2005.

[12] Hugo A. Jakobsen. *Chemical Reactor Modeling : Multiphase Reactive Flows*. Chemical Reactor Modeling. Springer International Publishing, Cham, 2nd ed. edition, 2014.

[13] Kichiz Niwa and Ocirc. A study on the diffusion of calcium ion in molten lime-silica-alumina slags by using a radioactive tracer technique. *Journal of the Japan Institute of Metals*, 21(4):304–308, 1957.

[14] Helen Towers and John Chipman. Diffusion of calcium and silicon in a lime-alumina-silica slag. *transactions of the Metallurgical Society of AIME*, 209, 1957.

[15] John Henderson, Ling Yang, and G. Dege. Self-diffusion of aluminum in cao-sio2-al2o3 melts. *Transactions of the Metallurgical Society of AIME*, 221, 1961.

[16] Y Oishi, R Terai, and H Ueda. *Oxygen diffusion in liquid silicates and relation to their viscosity*, pages 297–310. Springer, 1975.

[17] Yan Liang, Frank M. Richter, Andrew M. Davis, and E. Bruce Watson. Diffusion in silicate melts: I. self diffusion in cao-al2o3-sio2 at 1500c and 1 gpa. *Geochimica et Cosmochimica Acta*, 60(22):4353–4367, 1996.

[18] Merete Tangstad. *Chapter 6 - Ferrosilicon and Silicon Technology*, pages 179–220. Butterworth-Heinemann, Oxford, 2013.

[19] Jakobsson. *Distribution of boron between silicon and CaO-SiO_2, MgO-SiO_2, CaO-MgO-SiO_2 and CaO-Al_2O_3-SiO_2 slags at 1600°C*. Thesis, NTNU, 2013.

[20] Richard H Rein and John Chipman. Activities in liquid solution sio2-cao-mgo-al2o3 at 1600 degrees c. *Transactions of the Metallurgical Society of AIME*, 233(2):415–, 1965.

[21] Kazuki Morita, Kousuke Kume, and Nobuo Sano. A newly developed method for determining sio2 activity of the silicate slags equilibrated with molten silicon alloys. *ISIJ International*, 40(6):554–560, 2000.

[22] Takahiro Miki, Kazuki Morita, and Nobuo Sano. Thermodynamic properties of aluminum, magnesium, and calcium in molten silicon. *Metallurgical and Materials Transactions B*, 29(5):1043–1049, 1998.

[23] T Margaria, M Rebiere, F Traversaz, and C Dumay. Silicon refining: experimental studies and industrial means to control silicon quality. *Silicon for the Chemical Industry IH, Sandefjord, Norway*, pages 21–31, 1996.

[24] Torsten Weiss and Klaus Schwerdtfeger. Chemical equilibria between silicon and slag melts. *Metallurgical and Materials Transactions B*, 25(4):497–504, 1994.

[25] Xin-guo Wang, Wei-zhong Ding, Kai Tang, Guo-chang Jiang, and K-d Xu. Experimental thermodynamic research on equilibrium between silicon alloy and sio2-cao-al2o3 melt. *TRANSACTIONS-NONFERROUS METALS SOCIETY OF CHINA-ENGLISH EDITION-*, 11(4):535–539, 2001.

[26] Donald A. Drew and Stephen L. Passman. *Theory of Multicomponent Fluids*. Springer New York, 1999.

[27] Alireza Ashrafian, Stein Tore Johansen, Sean Gaal, and Birger Andresen. A reactor model for ladle refining of silicon metal, 2008.

[28] Kai Tang. Interview by erlend lunnan bjørnstad at 10:00-11:00 06.11.2015, 2015.

[29] Stephen Lobo and Leiv Kolbeinsen. *Compendium for Fluid Flow and Heat Transfer, Advanced Course TMT4208 NTNU. Based on norwegian compendium by Bakken, Jon Arne published 1992 for the course Metallurgical Engineering II at NTH.* IMT NTNU, Trondheim, Norway, 2010.

[30] Wolf-Dieter Deckwer and Robert W. Field. *Bubble column reactors*. Reaktionstechnik in Blasens´aulen. Wiley, Chichester, 1992.

[31] E. Buckingham. On physically similar systems; illustrations of the use of dimensional equations. *Physical Review*, 4(4):345–376, 1914.

[32] Richard M. Pashley and Marilyn E. Karaman. *Applied colloid and surface chemistry*. Wiley, Chichester, 2004.

[33] JR Grace. Shapes and velocities of bubbles rising in infinite liquids. *Trans. Inst. Chem. Eng.*, 51(2):116–120, 1973.

[34] J.R. Grace, T. Wairegi, and T.H. Nguyen. Shapes and velocities of single drops and bubbles moving freely through immiscible liquids. *Trans. Inst.Chem. Eng*, 54:167–173, 1976.

[35] ASTM International. Standard practice for calculation of mean sizes/diameters and standard deviations of particle size distributions, astm e2578-07(2012), 2012.

[36] J. Sauter. Determining size of drops in fuel mixture of internal combustion engines (”grôssenbestimmung der brennstofftropfen im gemischnebel von verbrennungskraftmaschinen”). *Techncal Memorandums National Advisory Committee for Aeronautics No.390 translated from the original journal Zeitschrift des Vereines deutscher Ingenieure by Miner, Dwight M.*, pages 1040–1042, 1926.

[37] William L. Haberman, R. K. Morton, and David W. Taylor Model Basin. *An experimental investigation of the drag and shape of air bubbles rising in various liquids / by W. L. Haberman and R. K. Morton*. [David W. Taylor Model Basin], Washington, D.C., 1953.

[38] T Tadaki and S Maeda. On the shape and velocity of single air bubbles rising in various liquids. *Kagaku Kogaku*, 25:254–264, 1961.

[39] J. O. Hinze. Fundamentals of the hydrodynamic mechanism of splitting in dispersion processes. *AIChE Journal*, 1(3):289–295, 1955.

[40] PH Calderbank. Physical rate processes in industrial fermentation. part i: The interfacial area in gas-liquid contacting with mechanical agitation. *Trans. Inst. Chem. Eng*, 36(5):433–440, 1958.

[41] Jan Erik Olsen, Dadan Darmana, Alireza Ashrafian, and Kai Tang. Cfd modelling of a reactive gas stirred three phase silicon reactor, 2008.

[42] Harald Laux and Stein Tore Johansen. A cfd analysis of the air entrainment rate due to a plunging steel jet combining mathematical models for dispersed and separated multiphase flows. *Fluid Flow Phenomena in Metal Processing*, 1999.

[43] P. E. Anagbo and J. K. Brimacombe. Plume characteristics and liquid circulation in gas injection through a porous plug. *Metallurgical Transactions B*, 21(4):637–648, 1990.

[44] Nigar Kantarci, Fahir Borak, and Kutlu O. Ulgen. Bubble column reactors. *Process Biochemistry*, 40(7):2263–2283, 2005.

[45] Korekazu Ueyama and Terukatsu Miyauchi. Properties of recirculating turbulent two phase flow in gas bubble columns. *AIChE Journal*, 25(2):258–266, 1979.

[46] Wolf-Dieter Deckwer, Youssef Louisi, Ahmed Zaidi, and Milos Ralek. Hydrodynamic properties of the fischer-tropsch slurry process. *Industrial and Engineering Chemistry Process Design and Development*, 19(4):699–708, 1980.

[47] R. Clift, John R. Grace, and M. E. Weber. *Bubbles, drops, and particles*. Academic Press, New York, 1978.

[48] E Salami, A Vignes, and P Le Goff. Hydrodynamique des dispersions. ii. effet de paroi. mouvement d'une goutte ou d'une bulle dans un fluide immobile contenu dans un tube vertical de petit diametre. *Genie Chimique*, 94:67–77, 1965.

[49] Seiji Uno and R. C. Kintner. Effect of wall proximity on the rate of rise of single air bubbles in a quiescent liquid. *AIChE Journal*, 2(3):420–425, 1956.

[50] J. R. Strom and R. C. Kintner. Wall effect for the fall of single drops. *AIChE Journal*, 4(2):153–156, 1958.

[51] R. Collins. The effect of a containing cylindrical boundary on the velocity of a large gas bubble in a liquid. *J. Fluid. Mech.*, 28(1):97–112, 1967.

[52] R. Collins. Experiments on large gas bubbles in liquids. Report AERE-R–5402, Atomic Energy Research Establishment, Harwell (England), 1967.

[53] Graham B. Wallis. *One-dimensional two-phase flow*. McGraw-Hill, New York, 1969.

[54] Tibor Z. Harmathy. Velocity of large drops and bubbles in media of infinite or restricted extent. *AIChE Journal*, 6(2):281–288, 1960.

[55] William L. Haberman and R.M Sayre. Motion of rigid and fluid spheres in stationary and moving liquids inside cylindrical tubes. Report 1143, Department of the Navy David Teylor Model Basin: Hydromechanics Laboratory Reserch and Development, 1958.

[56] Ruth E. Wolf. What is icp-ms? ... and more importantly, what can it do?, *http://crustal.usgs.gov/laboratories/icpms/intro.html*, 13.08.13 2005.

[57] Frithof Bjørnstad and Olav Galteland. Sammendrag av kj2050 - analytisk kjemi, 2013.

[58] Marc J. Assael, Ivi J. Armyra, Juergen Brillo, Sergei V. Stankus, Jiangtao Wu, and William A. Wakeham. Reference data for the density and viscosity of liquid cadmium, cobalt, gallium, indium, mercury, silicon, thallium, and zinc. *Journal of Physical and Chemical Reference Data*, 41(3), 2012.

[59] NIST-JANAF Thermochemical Tables. ed. by mw chase, jr. *J. Phys. Chem. Ref. Data*, 1998.

[60] John L Lyman and Tetsuji Noda. Thermochemical properties of si2f6 and sif4 in gas and condensed phases. *Journal of Physical and Chemical Reference Data*, 30(1):165–186, 2001.

[61] ASTM International. Standard practice for calculating and using basic statistics, astm e2586-14, 2014.